Electrochemical Studies of Nanoscale Objects: Proteins and Inorganic Nanoparticles

by

LEI WANG

BS, Wuhan University, 2003

MS, University of Pittsburgh, 2006

Submitted to the Graduate Faculty of

School of Arts and Science in partial fulfillment

of the requirements for the degree of

Doctor of Philosophy

University of Pittsburgh

2010

UNIVERSITY OF PITTSBURGH

School of Arts and Science

This dissertation was presented

by

Lei Wang

It was defended on

April, 2010

and approved by

Steve Weber, Professor, Department of Chemistry

Adrian Michael, Professor, Department of Chemistry

Jung-Kun Lee, Assistant Professor, Dept. of Mechanical Engineering and Materials Science

Dissertation Advisor: David H. Waldeck, Professor, Department of Chemistry

Electrochemical Studies of Nanoscale Objects: Proteins and Inorganic Nanoparticles

Lei Wang, PhD

University of Pittsburgh, 2010

Conformational transitions of proteins play a crucial role in many biochemical and biophysical reactions. Understanding the conformational changes of a protein upon adsorption to a substrate is very important in biotechnology, e.g. the development of modern protein chip technology, biocompatibility of implants, and many other ones. This research program used cytochrome *c*, an electron carrier in the respiratory chain, as a model to probe how surface adsorption affects the folding of a protein. My work investigates the interaction of protein horse heart cytochrome c when it is electrostatically adsorbed or covalently attached onto a 1 nm thick monolayer film, which covers an Au surface. After changing the pH value of the solutions or adding the denaturants into the solutions, the conformation of cytochrome c changes and causes a change of the peak current of cyclic voltammgram. In addition, the denatured cytochrome c's peroxidase activity has been studied and compared at different pH.

Assemblies of CdSe and CdTe nanoparticles (NPs) on a dithiol coated Au electrode were created and their electronic energetics were quantified. This research describes the energy level alignment of the filled and unfilled electronic states of nanoparticles with respect to the Au Fermi level. Using cyclic voltammetry it was possible to measure the energy of the filled states of the NPs with respect to the Au substrate, and by using photoemission spectroscopy it was possible to independently measure both the filled state energies and those of the unfilled states with respect to the vacuum level. Comparison of these two different measures shows good

agreement with the IUPAC accepted value of the absolute electrode potential. In contrast to the common model of energy level alignment, the experimental findings show that the filled states become 'pinned' to the Fermi level of the Au electrode, even for moderately small NP sizes. Photophysical and photoinduced electron transfer processes that follow the excitation of the NP assemblies are probed by photoelectrochemical measurements. For bilayer assemblies of two different NPs on a Au substrate, the photocurrent response of the bilayer assemblies depends on the ordering of differently sized nanoparticles with respect to the surface.

TABLE OF CONTENTS

LIST OF TABLES

LIST OF FIGURES

LIST OF SCHEMES

Dedicated to my parents.

ACKNOWLEDGEMENTS

First of all, I would like to thank Prof. David H. Waldeck for his very helpful guidance and generous support. His precise research attitude, great work ethic, broad knowledge not limited to chemistry, but all other sciences, especially physics and mathematics, inspire me to explore and get close to the truth behind the phenomenon.

I have been working together with Dr. Eugene Wagner to teach P-Chem lab. His prominent teaching skills are highly welcomed by the students. The experience I gain in the P-Chem lab will benefit my research and teaching career along my life.

I also want to thank my collaborator Dr. Liana V. Basova, Dr. Igor V. Kurnikov, Prof. Valerian E. Kagan, and Prof. Ron Naaman, through whom I can view my research from another perspective. I learned a lot of things from them. Furthermore, I want to thank my committee members Prof. Adrian Michael, Prof. Steve Weber, and Prof. Jung-Kun Lee for their time and advice to complete this work.

I would like to thank Dr. Hongjun Yue, who taught me the basic experiment steps when I just joined Prof. Waldeck's group. His patience helped me get used to the new research quickly. I would like to thank Dr. Amit Paul, who joined the chemistry department and Prof. Waldeck's group in the same year as me. His optimistic attitude to life and research always cheer me up. His help and advice on my proposal and thesis preparation are highly appreciated. Daniel Lamont is

a very knowledgeable and versatile labmate and friend, who trained me the use of AFM and helps me correct my English all the time. I also want to thank Mingyan Wu and Yang Wang for synthesizing the nanoparticles. I could not have finished my research without their help.

It has been a wonderful and lucky experience to work with my intelligent labmates: Dr. Min Liu, Dr. Palwinder Kaur, Dr. Subhasis Chakrabarti, Dr. Emil Wierzbinski, Dr. Prasun Mukherjee, Kathryn Davis, Matt Kofke, Xin Ying, Robin Sloan, and Brian Bloom. I am proud to work with them as a team to explore the mystery of science.

I want to express my appreciation to the support team of our department: electronic shop, machine shop, glass shop, main office and stockroom staffs. Their expertise and generous help are indispensible for me to finish my research.

Finally, I want to express my deepest love to my parents for their constant and selfless support and help along my life. My parents never had a chance to get to college in their era. But they gave all they have to educate me into college, up to graduate school. Especially, I would like to thank my father, whose dream is his son will be a Ph.D. and scientist in future. He worked so hard that I ever wondered he never slept in my childhood. He tried to save every penny himself and passed his fortune to support his son to get the best education in the world. Unfortunately, my father passed away in a car accident in the year of 2006. This thesis is dedicated to his dream. May he find peace in heaven. I want to give my special blessings to my mother, who devoted all her life to his son. She was just diagnosed with cancer and had a surgery. My mother is not a strong person, but she kept the tragic news from me to keep me from worry. I have been taken care of all the time, and now it is my turn to take care of my mother. We will defeat the cancer. Before I left China in 2003, all my family were there. I lost both of my grandparents, who brought me up, during these years. I very much regretted I could not be

near during their last breath. The Ph.D. study abroad is not only a process to gain knowledge, but also a process to grow up. At last, I want to thank all my family and friends, who help to look after my parents, share my happiness and sadness along my life.

1.0 INTRODUCTION

Electron transfer has been one of the hottest research topics in the past decades. Conceptually, it is referred as the process by which an electron moves from one atom or molecule to another atom or molecule. Electron transfer phenomena are widely reflected in the broad spectrum of diverse systems, including numerous processes in biology: oxygen binding, photosynthesis, respiration, and detoxification routes; ion, complexes, organic and inorganic supermolecules in polar or nonpolar solvents; metal, semiconductor, and superconductor electrodes in solution; surfaces and interfaces involving thin films, adsorbants and surface states; and processes of energy acquisition and storage, such as fuel cell and solar cell.

The modern era of electron transfer studies began after World War II.[1] It has been experiencing explosive development in chemistry, physics, and biology since the classical theory introduced by Rudoph A. Marcus.[2-4] My research involves the electron transfer of both protein and semiconductor nanoparticles (NPs) immobilized at the metal electrodes through alkanethiol linkers.[5] In the heterogeneous electron transfer, an electron moves between a chemical species and a solid-state electrode. Cyclic voltammetry has been used to study the electron transfer of chemical species immobilized at the metal surface, and redox potential of chemical species can be determined from the voltammograms. 1) Cytochrome *c*, an electron carrier in the respiratory chain, was used as a probe to explore how the protein conformation changes when it is immobilized onto the surface. And the redox potential of the cytochrome *c* plays a crucial role in

its biological function of electron transfer in respiratory chain. The formal redox potential for ferri/ferrocytochrome c couple is 0.265 V versus NHE (pH 7)[6] while it shuttle electrons between complex III and complex IV in the respiratory chain. Immobilization of cytochrome c into the surface results in the redox potential change depending on temperature,[7] pressure,[8] electrolyte composition and ionic strength.[9] Thus, the protein on an electrode surface may behave differently from its native state, which can provide meaningful instruction for the biosensor and biochip applications. 2) Semiconductor nanoparticles are envisioned as materials for light harvesting and photovoltaic applications.[10] One may envision that a device based on NPs will contain NPs of various band gaps, so as to cover the entire solar spectrum, and that one could engineer the device so that the NPs self-assemble into a robust superstructure. To design such structures efficiently, one would like to know the position of the electronic states, both occupied and unoccupied, so that efficient charge separation can be made possible. The redox potential measurement from the voltammetry can provide the energetics for semiconductor NPs immobilized on the surface, so as to optimize the architecture of the nanoparticle assembly.

In the introduction section of this thesis, I will first talk about the self-assembly of monolayers in section 1.1, which summaries the electrode preparation and chemical species immobilization. Classical Marcus theory will be introduced in section 1.2, as its application in heterogeneous electron transfer of redox species immobilized at the metal electrode. Section 1.3 and 1.4 review the current studies of interfacial electron transfer of cytochrome c and the electrochemistry of semiconductor nanoparticles, respectively.

1.1 SELF-ASSEMBLED MONOLAYER

1.1.1 History of SAMs

Self-assembled monolayers (SAMs) are composed of ordered molecular assemblies formed on a solid surface. The field of SAMs really began much earlier than is now appreciated. In 1946 Zisman first demonstrated the preparation of a monomolecular layer by adsorption of a surfactant onto a clean metal surface.[11] At that time, the potential of self-assembly was not recognized, and this publication initiated only a limited level of interest. Over the last two decades, this field has experienced huge growth in synthetic development and depth of characterization.[12] The exponential growth in SAM research is an example of the changes that chemistry as a discipline has experienced.

The early literature on SAMs focused largely on the assemblies formed by the adsorption of organosulfur compounds from solution or the vapor phase onto metal substrates of gold and silver.[13] These studies used three types of organosulfur compounds: alkanethiols ($HS(CH_2)_nX$), dialkyl disulfides ($X(CH_2)_mS\text{-}S(CH_2)_nX$), and dialkylsulfides ($X(CH_2)_mS(CH_2)_nX$), where n and m are the number of methylene units and X represents the end group of the alkyl chain ($-CH_3$, -OH, -COOH). The experiments established many of the basic structural characteristics of these systems (surface structure, chain organization, orientation), practical protocols for preparing SAMs (concentrations, length of time for immersion, solvents, temperature), and some details of the thermodynamics and kinetics governing the process of assembly.

A major portion of the research on SAMs since the early 1990s has continued to expand the types of substrates and molecules used to form them. The past decade has seen a significant expansion in studies that explore the assembly of SAMs on nanostructures.[14] The availability of

new types of nanostructures with well-defined shapes and sizes, either on substrate or in solution, has stimulated the wide application of SAMs for stabilizing these new structures and manipulating their interfacial/surface properties.

1.1.2 Preparation of SAMs

The most common protocol for preparing SAMs on gold, silver and other materials is to immerse a freshly prepared or clean substrate into a dilute (~1-10 mM) ethanol solution of thiols for ~12-18 h at room temperature. This procedure is widely used and originated from early studies of SAMs.[15] Two distinct adsorption kinetics can be observed: a very fast step, which takes a few seconds to minutes, by the end of which the contact angles are close to their limiting values and the thickness is about 80-90% of its maximum, and a slow step, which lasts several hours to maximize the density of molecules and minimize the defects in the SAM.[12] However, there are a number of experimental factors that can affect the structure of the resulting SAM and the rate of formation: solvent, temperature, concentration of adsorbate, immersion time, purity of the adsorbate, concentration of oxygen in solution, cleanliness of the substrate, and chain length.

SAMs formed by adsorption of alkanethiol onto a gold substrate has been most studied and understood, for at least following reasons: (1) Gold is a reasonably inert metal. It was suggested that gold does not have a stable surface oxide.[16] Therefore, its surface can be cleaned simply by removing the physically and chemically adsorbed contaminants. These properties make it possible to handle and manipulate gold samples under atmospheric conditions instead of under UHV. (2) Gold is easy to obtain, both as a thin film and as a colloid. It is straightforward to prepare thin films of gold by physical vapor deposition, sputtering, or eletrodeposition. And single crystals are available commercially. (3) Gold binds thiols with a high affinity,[17] and it

does not undergo any unusual reactions with them. This specific interaction allows thiol molecules to form a well packed SAM. (4) Thin films of gold are common substrates used for a number of existing spectroscopies and analytical techniques, including quartz crystal microbalance (QCM), surface plasmon resonance (SPR) spectroscopy and ellipsometry. This characteristic is particularly useful for applications of SAMs as interfaces for studies in biology.

Other materials offer similar properties, but the SAMs formed on these materials have been less studied than those on gold. Silver is the most studied substrate for SAMs of alkanethiols next to gold, but it oxidizes readily in air and is toxic to cells. However, it does give high quality SAMs with a simpler structure than gold.

1.1.3 SAMs for Electrochemistry

One of the simplest and most broadly used methods developed for modifying SAMs is the formation of amide linkages via an interchain anhydride intermediate.[18,19] In this method, a SAM terminated with carboxylic acids is activated by *N*-hydroxysuccinimidyl (NHS) esters and the subsequent reaction with an amine. The reaction is straightforward and yields amide bonds. Using this method, ligands and proteins have been immobilized on mixed SAMs. For mixed SAMs with a low fraction of acid functional groups (~ 10% surface coverage), RAIR spectroscopy indicated that the conversion of free acids to NHS esters was nearly quantitative and that the reaction of amines with the activated ester generated amides in better than 80% yield.[20]

Another set of methods for modifying the composition of SAMs use either the intrinsic properties of the surface (hydrophobicity, electrostatics) or selective interactions with the preformed chemical functional groups on the surface to promote adsorption of materials from

solution. These methods use noncovalent interactions rather than covalent reactions to stabilize the adsorbed materials.

A practical method for altering the composition of the exposed surface of a SAM is the adsorption of materials from solution. Surfactants, polymers, polyelectrolytes, proteins, organic dyes, and colloidal particles are examples of the types of materials that can adsorb onto SAMs. The attractive interactions between the adsorbant and surface are primarily van der Waals forces, electrostatic forces, or combinations of the two. Hydrophobic SAMs, such as ones formed from *n*-alkanethiols, readily adsorb amphiphilic molecules, some polymers, and most proteins.[21]

The ordered SAM on electrode makes it possible to generate barrier layers that prevent free diffusion of electroactive species to the surface of the electrode. Meanwhile, the electroactive species are immobilized on the electrode itself, which has proven useful in the characterization of electron transfer process. Compared to LB films or nonspecific physisorbed films, SAMs are more convenient and more effective choices for modifying electrodes in electrochemistry. They form spontaneously, and are relatively stable in solutions of electrolytes with a wide potential window.

There are two experimental configurations used commonly in electrochemistry for studying electron-transfer processes with chemically modified electrodes.[13] One strategy uses a thick (1−2 nm), hydrophobic SAM to block a redox species from diffusing to the surface of the electrode itself. A second approach uses a mixed SAM where one molecular component terminates with an electroactive group (for example, ferrocene). The immobilization of the redox species on the SAM minimizes effects of diffusion in the measured current responses. By changing the thickness of the SAM, coupling between the redox species and the electrode can be

effectively controlled. Thus, the electron transfer rate dependence on the thickness of SAM can be monitored.

Besides the distance dependence study, some electrochemical applications with these SAM-modified electrodes include (1) microarray electrodes,[22] (2) coupled electron−proton-transfer reactions,[23] (3) electrocatalysis,[24] (4) the effect of counterion motion on the rates of electron transfer,[25] (5) the corrosion control and adhesion control,[26] (6) the effect of orientation and conformation of electroactive proteins (cytochrome *c*, glucose oxidase) on the rates of electron transfer across SAMs. [27]

1.2 ELECTRON TRANSFER THEORY[1-4,28-32]

1.2.1 Motivation

The study of heterogeneous electron transfer kinetics has experienced a revitalization in recent years. This increased interest in both the experimental and theoretical aspects of electrode kinetics results from several factors. On the experimental front, recent technical advances have increased the applicability and range of electrochemical kinetic measurement. The increasing popularity and utility of ultramicroelectrodes allow electron transfer rates to be measured for more rapid redox reactions and in much more resistive solution than is possible with larger electrodes. The development of in situ scanning tunneling microscopes allows one to image electrodes surfaces with atomic scale resolution and scanning electrochemical microscopy can be used to measure local electron transfer rates. The development of compact self assembled monolayer films can be used to control the interfacial structure of the electrode and to probe both

the reactivity of redox molecules and the nature of the electronic coupling through the monolayer film. The theoretical progress rests on the Marcus electron transfer theory, which quantitatively describes the chemical reactions in the condensed phase. It is widely used to explain a number of important processes in chemistry and biology, including photosynthesis, corrosion, certain types of chemiluminescence, charge separation in some types of solar cell and more.

Current areas of interest in homogeneous electron transfer dynamics include long-range electron transfers in biological systems, the influences of the static and dynamic properties of solvents on the electron transfer rate, and the nature of the driving force dependence of electron transfer rates. Because electron transfers occurring at electrode surfaces share many of the same characteristics as homogeneous electron transfers, electrochemical techniques can play an important role in the elucidation and validation of electron transfer theories and in the characterization of redox active molecules kinetics.

1.2.2 Background

Part of the difficulty in following the recent advances in heterogeneous electron transfer kinetics is that one cannot use the standard Butler-Volmer equation, which fits the potential dependence of the electron transfer rate. The Butler-Volmer equation for the reduction rate constant at an electrode polarized to a potential *E*, $k_f(E)$, is

$$k_f(E) = k^0 e^{-\alpha n f (E - E^{0'})} \tag{1.1}$$

where k^0 is the rate constant measured when the electrode is polarized to the formal potential of the redox molecule, $E^{0'}$; α is the transmission coefficient; n is the number of electrons transferred; and f = F/RT, where F is Faraday's constant, R the gas constant, and T the absolute temperature. From a plot of the logarithm of the measured heterogeneous rate constant versus the formal over-

potential, one obtains α and k^0 parameters from the slope and intercept, which characterize the electron transfer reaction. Stemming from an empirical approach, this Butler-Volmer analysis is seriously deficient in describing the molecular factors that govern the electron transfer rate. To develop more deeply into these molecular factors, one must adopt a more general mathematical and conceptual framework for predicting and evaluating heterogeneous electron transfer data. Thus electron transfer rate expressions will be developed from the next-higher level of sophistication using a transition-state approach relying heavily on the Marcus theory approximations.

A useful characterization of electron transfer reactions is whether they involve an inner-sphere mechanism, the electron transfer occurs without a significant change in the redox molecule's internal structure. Qualitatively, outer-sphere mechanisms occur when there are no strong chemical interactions between the reactions. For a heterogeneous electron transfer, an outer-sphere redox mechanism requires only weak interactions between the redox molecule and the electrode surface. The electron transfer properties of such an outer-sphere redox molecule are the same at the electrode surface as in the bulk solution. In contrast, electron transfers that involve strong interactions between the redox molecule and the electrode can be characterized as inner-sphere electron transfers. In these cases the adsorbed redox molecule's internal structure and extent of solvation can be significantly different from that in solution. The actual reacting species can be considered to be a different molecule from its precursor in the solution. Because the structure of the reactive form of the redox species adsorbed at the electrode surface is not generally known, these inner-sphere electron transfer mechanisms are considerably more difficult to study and predict. Because of the added complications in describing inner-sphere

electron transfers, most of the experimental and theoretical effort has been focused on the simpler outer-sphere mechanism.

1.2.3 Marcus Theory of Electron Transfer

With the complex motion of the redox molecules and solvent and the involvement of quantum mechanical tunneling, the task of developing a mathematical expression for the electron transfer rate may seem daunting. However, expressions derived by Marcus have formed the basis of much of the theoretical work in modern electron transfer theory. Below is outlined a presentation of the Marcus theory.

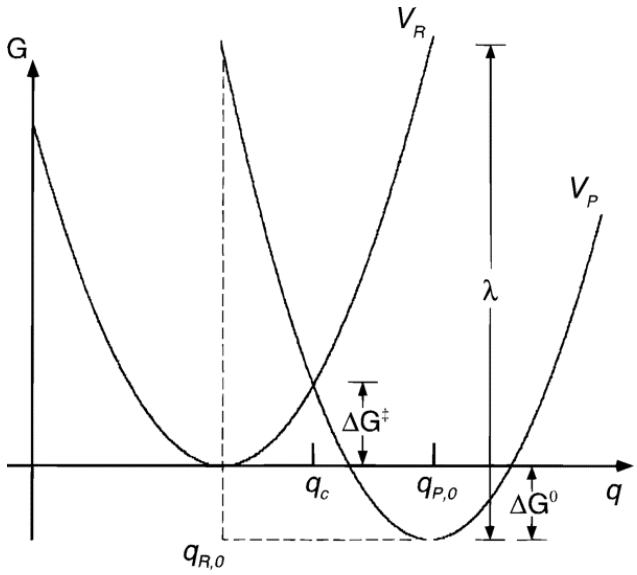

Figure 1.1 Free energy curve for an electron transfer reaction

The best known assumption of the Marcus theory of electron transfer is that the free energy of activation of the redox molecule can be approximated by considering two simple parabolic wells with respect to displacement along the reaction coordinate. In Figure 1.1, the Gibbs free energy surfaces are assumed to have a quadratic shape with the same force constant. The displacements q_R and q_P refer to the equilibrium geometry of the reactant and the product

respectively. By thermal fluctuation, reactant molecules reach point q_c, the transition state, and electron transfer can occur. The electron transfer rate constant k_{ET} is determined by the following expression,

$$k_{ET} = \upsilon_n \kappa_{el} \exp(-\Delta G^{\neq}/k_B T) \quad (1.2)$$

where κ_{el} is the electronic transmission coefficient, υ_n is the frequency of passage (nuclear motion) through the transition state corresponding to the point q_c, $\Delta G^{\neq}$ is the activation free energy, k_B is the Boltzmann constant, and T is the temperature. It is useful to distinguish two types of ET reaction: 1) adiabatic ET reaction if $\kappa_{el} \approx 1$, which means that almost every passage through the transition state leads to electron transfer, and 2) nonadiabatic ET reaction when $\kappa_{el} << 1$, which means that just a small fraction of passage through the transition state leads to electron transfer.

By assuming that the quadratic energy surfaces have the same force constant, the $\Delta G^{\neq}$ can be calculated from the free energy of reaction ΔG^0 and reorganization energy λ with the following equation,

$$\Delta G^{\neq} = (\lambda + \Delta G^0)^2/4\lambda \quad (1\text{-}3)$$

The reorganization energy λ is defined as the energy required to interconvert the most stable structures of the oxidized and reduced forms of the redox couple while maintaining their initial oxidation states.

Inserting equation 1-3 for the activation energy into equation 1-2 for the rate constant, we find the expression,

$$k_{ET} = \upsilon_n \kappa_{el} \exp[-\frac{(\lambda+\Delta G^0)^2}{4\lambda k_B T}] \quad (1\text{-}4)$$

Equation 1-4 follows from the transition state theory and is a highly useful relationship. However, there are clearly problems with the theory. The most evident case is temperature dependence.

Equation 1-4 predict infinite small electron transfer rate when temperature approaches zero. Experimentally, at low temperatures the rate constant is essentially temperature independent. The conflict appears because it is assumed that the barrier must be crossed. This issue was addressed by a number of workers, who borrowed the time dependent perturbation theory. Modes coupled to electron transfer must be treated as quantum mechanical if the spacing between the vibration levels is large compared to thermal energies. The rate constant from the Fermi "Golden Rule" give the expression in the high temperature region as,

$$k_{ET} = \frac{2\pi}{\hbar}\frac{|V_{rp}|^2}{\sqrt{4\pi\lambda k_B T}} exp[-\frac{(\lambda+\Delta G^0)^2}{4\lambda k_B T}] \quad (1\text{-}5)$$

where V_{rp} is the electronic coupling between reactant and product states.

For the specific case of electron transfer in metallic electrodes, the electrode and redox species can be considered to be electron donor and acceptor. In a cathodic reaction, electrons flow from filled metallic states to the vacant electronic states of the redox species, and the molecule is reduced. The free energy of this reduction reaction can be expressed as

$$\Delta G^0 = \varepsilon_f - \varepsilon + e\eta \quad (1\text{-}6)$$

where η is formal overpotential, ε_f is the Fermi energy. Combining equation 1-5 and equation 1-6, the electron transfer rate constant of transmission from one metallic level to a redox species is given as:

$$k_{RED} = \frac{2\pi}{\hbar}\frac{|V_{rp}|^2}{\sqrt{4\pi\lambda k_B T}} exp[-\frac{(\lambda+\varepsilon_f-\varepsilon+e\eta)^2}{4\lambda k_B T}] \quad (1\text{-}7)$$

At a conductive electrode surface, electrons can be exchanged between multiple redox electronic states and metallic electronic states meeting the requirement of conservation of energy. The rate constant may be obtained by taking the summation over these states, and be written as

$$k_{RED} = \frac{2\pi}{\hbar}\frac{|V_{rp}|^2}{\sqrt{4\pi\lambda k_B T}} \int_{-\infty}^{+\infty} \rho(\varepsilon) f(\varepsilon) exp[-\frac{(\lambda+\varepsilon_f-\varepsilon+e\eta)^2}{4\lambda k_B T}] d\varepsilon \quad (1\text{-}8)$$

where $\rho(\varepsilon)$ is the density of electronic states of the metallic electrode, and $f(\varepsilon)$ is the Fermi-Dirac distribution law,

$$f(\varepsilon) = \frac{1}{1+\exp\left[\frac{\varepsilon-\varepsilon_f}{k_B T}\right]} \tag{1-9}$$

The oxidation rate constant can be obtained in a similar way

$$k_{OX} = \frac{2\pi}{\hbar}\frac{|V_{rp}|^2}{\sqrt{4\pi\lambda k_B T}}\int_{-\infty}^{+\infty}\rho(\varepsilon)(1-f(\varepsilon))exp[-\frac{(-\lambda+\varepsilon_f-\varepsilon+e\eta)^2}{4\lambda k_B T}]d\varepsilon \tag{1-10}$$

Kinetics studies of redox species immobilized at a metallic electrode can be performed by cyclic voltammetry, which is a dynamic electrochemical method. In cyclic voltammetry, the current response is recorded as a function of the change of the potential scan rate. Equations 1-8 and 1-10 are modified to calculate synthetic cyclic voltammograms. In particular, the electronic density of states in the metal was approximiated as being constant over the energy regime that contributes significantly to the measured current. In this case equations 1-8 and 1-10 become

$$k_{RED,\eta} = \frac{2\pi}{\hbar}\frac{|V_{rp}|^2}{\sqrt{4\pi\lambda k_B T}}\rho k_B T\int_{-\infty}^{+\infty}\frac{exp[-(x-\frac{(\lambda+\eta)}{k_B T})^2(\frac{k_B T}{4\lambda})]}{1+\exp(x)}dx \tag{1-11}$$

$$k_{OX,\eta} = \frac{2\pi}{\hbar}\frac{|V_{rp}|^2}{\sqrt{4\pi\lambda k_B T}}\rho k_B T\int_{-\infty}^{+\infty}\frac{exp[-(x-\frac{(\lambda-\eta)}{k_B T})^2(\frac{k_B T}{4\lambda})]}{1+\exp(x)}dx \tag{1-12}$$

Where ρ is the effective density of electronic states in the metal electrode, x is $(\varepsilon-\varepsilon_f)/k_B T$.

The current i in the volammetric experiment is directly related to the reduction and oxidiation rate constants. The voltammograms can be simulated from the equation 1-11 and 1-12. The dimensionless current i may be written as

$$i = \frac{\Delta f}{\Delta E/(RT/F)} = \frac{RT/F}{\Delta E}\left(f_{target}-f_0\right)(1-\exp[-(k_{RED}-k_{OX})\Delta t] \tag{1-13}$$

$$f_{target} = \frac{1}{1+\exp(-EF/RT)} \tag{1-14}$$

$$\nu = \frac{\Delta E}{\Delta t} \tag{1-15}$$

where Δt is the time interval over which the potential applied, ΔE is the potential step size, ν is the potential sweep rate, and f_0 is the fraction of oxidized species initially present in the time interval over which the potential step is applied.

Working curves of log(ν/k) versus peak shift are generated. By fitting the experiment results to the simulation curve, the electron transfer rate can be extracted from the oxidation and reduction peak separation with respect to the potential scan rate.

1.3 INTERFACIAL ELECTRON TRANSFER OF CYTOCHROME *C*

1.3.1 The Structure and Conformation of Cytochrome *c*

Electron transfer is of major importance in biological systems. It is widely reflected in many areas, such as oxygen binding, photosynthesis, and respiration. In general, the electron transfer processes in organisms are realized through the redox reactions between the proteins. Biological electron transfer occurs at protein-protein interfaces and many proteins or enzymes can only maintain their activities in a biological environment.[33] Self- assembled monolayer films have been suggested to mimic the biological environment. Thus, proteins that are immobilized at chemically modified electrode surfaces can provide a useful model system for exploring some fundamental aspects of protein electron transfer.

Metalloproteins have many different functions in cells, such as enzymes, transport and storage proteins, and signal transduction proteins. Indeed, about one quarter to one third of all proteins require metals to carry out their functions. Recently, significant progress has been made in understanding the structure, function and redox properties of metalloproteins called

cytochrome *c*.[34] From the structural point of view, horse heart cytochrome *c* is a relatively simple metalloprotein (consisting only of 104 amino acids), and is often considered as a model metalloprotein. The most important details of its structure were already known in the mid-1970s and include[35] 1) the heme is covalently attached to the protein through two thioester bonds to cysteines 14 and 17; 2) there is a "closed crevice" in which the heme iron is held, with the axial ligands histidine 18 and the methionine 80; 3) and the presence of five α-helical segments, notably the N-terminal (residues 2-14), the C-terminal (residues 87-103), and the helical segments 49-55, 60-70, and 70-75. These structural properties dictate the function of cytochrome *c*. Among other biological functions, horse heart cytochrome *c* plays an important role as an electron carrier in the mitochondrial inter-membrane space between two membrane-bound protein complexes, cytochrome *c* reductase and cytochrome *c* oxidase. The formal redox potential for ferri/ferrocytochrome c couple is 0.265 V versus NHE (pH 7),[6] and is known to vary with temperature, pressure, electrolyte composition and ionic strength.

It is well known that cytochrome *c* can be strongly adsorbed on Pt, Hg, Au, Ag and other electrodes.[36] The adsorption has been shown to result in conformational changes of the cytochrome *c*, protein unfolding and often its denaturation.[37] To solve this problem, chemically modified electrodes, in particular with self-assembled monolayers, have been widely used to inhibit the denaturation while maintaining electroactivity. Cytochrome *c* has a net positive charge. When SAMs composed of carboxylic acid-terminated thiols present a negatively charged surface, cytochrome *c* binds electrostatically to the surface. The assembly provides a direct model to study the electron transfer reaction. If the methylene chain length is longer than 6 methylene units, the nonadiabatic electron transfer rate constant k^0 of cytochrome *c* appears to depend exponentially on distance. The decay coefficient β is close to 1.1 per methylene group

when the number of methylene groups *n* in the chain is larger than 8. Interestingly, when *n* is smaller than 6, k^0 depends weakly on distance, showing a 'plateau region'. This phenomenon suggests two different mechanisms of electron transfer for the thin and thick SAM films.[38]

Conformational transitions of proteins play a crucial role in many biochemical and biophysical reactions. Understanding the conformational changes of a protein upon adsorption to a substrate is very important in biotechnology, e.g. the development of modern protein chip technology, biocompatibility of implants, and other phenomena.[39,40] In many applications, it is important that a protein retains its activity when it binds onto the substrate.

One of the most fundamental of all properties of a protein is the ability to fold spontaneously to a unique three-dimensional structure. The goal of studies of protein folding is to understand the physical mechanisms by which amino acid sequence determines protein structure and stability. Cytochrome *c* has played an important role in understanding these mechanisms.[41,42] A number of workers have studied the folding and unfolding of cytochrome *c* and it has been reported that cytochrome *c* can be denatured by urea,[43,44] guanidine hydrochloride[41,45] or pH.[46-48] A great deal of valuable information on specific aspects of cytochrome *c* folding has been obtained from a variety of spectroscopic techniques.[49] For example, nuclear magnetic resonance (NMR) has probed the solvent exposure of exchangeable protons on the polypeptide backbone.[50] Techniques such as circular dichroism (CD)[51] and small-angle X-ray scattering[52] provide information on the secondary structure content and average molecular size of the protein molecule, respectively. Tryptophan fluorescence and optical absorption spectroscopies provide information about local interchain interactions by taking advantage of the presence of the heme prosthetic group.[53,54] Resonance Raman spectroscopy has

been demonstrated to be especially useful in visualizing folding intermediates along the folding coordinate.[55,56]

Cytochrome *c* plays a key role during apoptosis.[57] Apoptosis describes a common type of programmed cell death that has been repeatedly observed in various tissues and cell types. After releasing to the cytosol, cytochrome *c* binds Apaf-1 (apoptotic protease-activating factor-1) and activates procaspase 9 to form a complex designated apoptosome. Activated caspase-9 can activate other caspases that ultimately destroy the cell. Through apoptosis, a multicellular organism can tightly control cell numbers and tissue size, and protect itself from rogue cells that destroy homeostasis.

Cytochrome *c* is positively charged at neutral pH and the inner mitochondrial membrane contains a large fraction of negatively charged phospholipids, cardiolipin.[58] Cytochrome *c* interacts electrostatically with the inner membrane in the mitochondria. It has been shown that once bound to cardiolipin, cytochrome *c* will change its conformation and chemical reactivity.[59] Cytochrome *c* plays a critical role in early apoptosis as a cardiolipin-specific oxygenase to produce cardiolipin hydroperoxides required for the release of proapoptotic factors. Hence, the peroxidase activity of cytochrome *c* is very important. When cytochrome *c* is in its native state, the heme pocket is wrapped by the peptide chain and protected from the solvent, even though it is located near the protein edge. When cytochrome *c* is unfolded by lowering the pH or increasing the concentration of denaturants, the heme pocket loses its integrity, and can unwrap to expose the heme to solvent molecules. Easy access of the heme pocket can facilitate the hydroperoxide catalyzing reaction.

In the chapter 2 and 3, the denaturation of cytochrome *c* and its peroxidase activity are characterized by cyclic voltammetry. Cyclic voltammetry allows one to monitor the redox

reaction as cytochrome *c* is unfolded. For the denatured cytochrome *c*, adding H_2O_2 into the buffer solution causes a great enhancement of current, and the current is stable even after several continuous scans. Moreover, the current increases with the concentration of H_2O_2 and the cytochrome *c*'s peroxidase activity is enhanced by binding to cardiolipin.

In the current study, the substrate is usually modified by a self-assembled monolayer (SAM) to which proteins can be adsorbed electrostatically or attached covalently. This research program uses cytochrome *c*, which is an electron carrier in the respiratory chain, as a model to probe how surface adsorption affects the folding of a protein. We consider the interplay between the peroxidase activity and the conformation of cytochrome *c* with the ultimate goal of better understanding the specificity of mitochondrial lipid oxidation in apoptosis.

1.3.2 Electron Transfer in Respiratory Chain[60]

As human-beings, we convert chemical energy into bioactivity everyday and compensate for the loss of chemical fuel by consuming food. Microscopically, energy is stored in the form of ATP within the cell, and it is released by converting ATP into ADP. ATP is synthesized from ADP in mitochondria.

$$ATP \rightleftarrows ADP + 31kJ/mol$$

A mitochondrion consists of four distinct subregions, the outer membrane, the inner membrane, the intermembrane space and the matrix. Whatever the compartment in which biological oxidation occurs, all of these processes generate reduced electron carriers, primarily NADH. When this NADH is reoxidized by the enzymes of the respiratory chain which are firmly embedded in the inner membrane, ATP is regenerated.

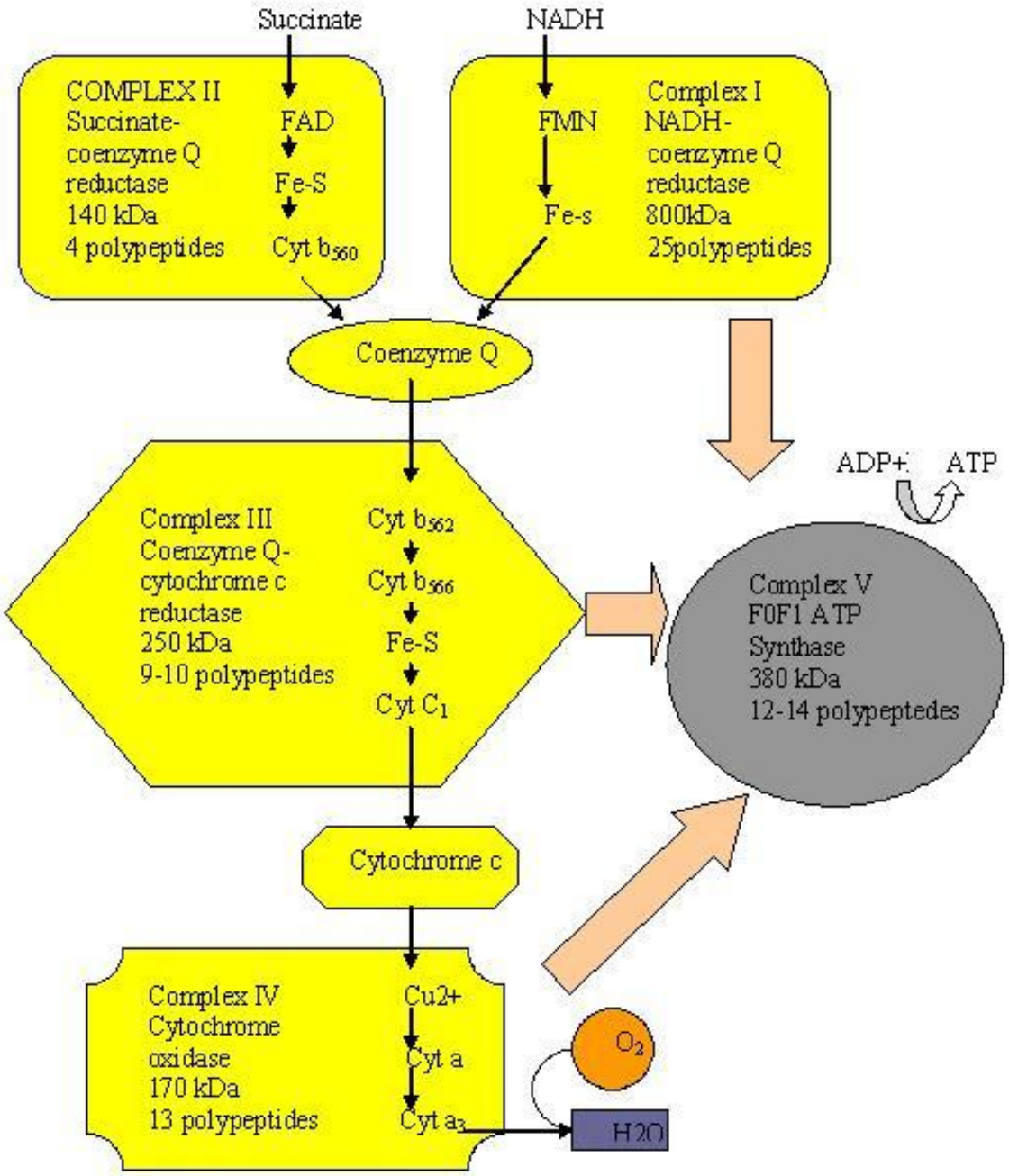

Figure 1.2 Multiprotein complexes in the respiratory assembly.

The inner membrane is highly folded into cristae throughout the interior of the mitochondrion. Because the protein carriers, primarily cytochromes, which constitute the

respiratory chain, are embedded within the inner membrane, the density of cristae is related to the respiratory activity of a cell. The higher the rate of respiration within a cell, the more densely the cristae are packed within a mitochondrion. For example, horse heart cells, which have a high rate of respiration, contain mitochondria with densely packed cristae. By contrast, liver cells, which have a slow rate of respiration, contain mitochondria with sparsely distributed cristae.

The protein carriers in the respiratory chain are assembled in the form of five multiprotein complexes, named complex I, II, III, IV and V (Figure 1.2). Complex I and complex II receive electrons from the oxidation of NADH and succinate, respectively, and pass them along to a lipid electron carrier, coenzyme Q, which moves freely through the membrane. Complex III gets the electron from coenzyme Q and passes it to cytochrome *c*. Finally, complex IV oxidizes the reduced form of cytochrome *c* and in turn reduces oxygen into water. The electron transfer process creates a proton gradient across the inner membrane, with protons being collected in the intermembrane space. Protons reenter the inner membrane through a specific channel in complex V. This process provides the necessary energy to drive the synthesis of ATP from ADP and inorganic phosphate.

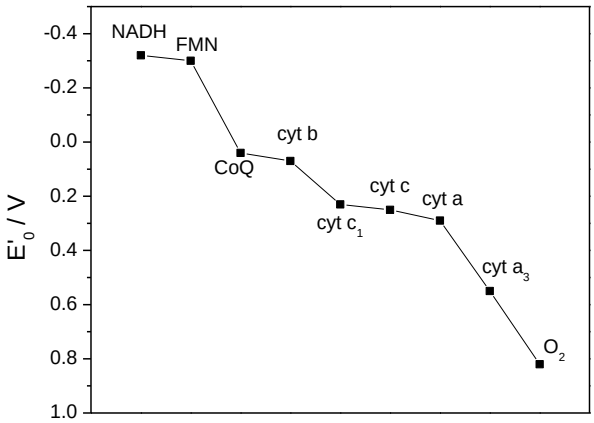

Figure 1.3 Standard reduction potentials of the major respiratory electron carriers.

If you compare the sequence of respiratory electron carriers with the standard reduction potentials of those carriers (Figure 1.3), you will see that $E_0^{'}$ for each carrier increases in the same order as the sequence of their use in electron transport. This order suggests that each individual redox reaction in electron transport is exergonic under standard conditions.

1.3.3 Apoptosis

Apoptosis, coined by Currie and colleagues in 1972, describes a common type of programmed cell death that has been repeatedly observed in various tissues and cell types.[61] This kind of programmed cell death is distinct from pathological cell death or necrotic cell death. Cells undergoing apoptosis show characteristic morphological features such as condensation of cytoplasmic and nuclear contents, blebbing of plasma membranes, fragmentation of nuclei, and ultimately breakdown into membrane-bound apoptotic bodies that are rapidly phagocytosed.[57] Stimuli, like cells in excess or potentially dangerous cells, will often trigger the release of proapoptotic proteins into the cytosol, then activation of caspases and a proteolytic cascade occurs, which finally results in apoptosis. In this way, a multicellular organism can tightly control cell numbers and tissue size, and protect itself from rogue cells that destroy homeostasis.[62]

The apoptotic regulators, the Bcl-2 family,[63] are a key factor for determining the fate of a cell: life or death. This Bcl-2 family consists of over a dozen proteins, which can be divided into three groups, based on structural similarities and functional criteria. Group I, such as Bcl-2 and Bcl-x_L, has the feature that all its members possess anti-apoptotic activity and protect cells from death. Group II, such as Bax and Bak, shares this feature with pro-apoptotic activity. Group III,

such as Bid and Bik, has the common feature which is the presence of ~12-16 amino acid BH3 domain.

Though the precise mechanism of how proapoptotic Bcl-2 members regulate the exit of cytochrome *c* is still unclear, two major models have been proposed.[57] The first model suggests Bcl-2 members insert into the lipid bilayer of the mitochondrial outer membranes and form channels that facilitate exit of cytochrome *c* and other apoptotic protein. This model is based on crystallography that suggests the three-dimensional structure of Bcl-x_L shares a similarity with the pore-forming domains of certain bacterial toxins, including diphtheria toxin (DT). Both structures contain two central hydrophobic helices surrounded by amphipathic α helices. The suggested function of the pore-forming domain of DT is to allow the subunit of the toxin to transit from the interior of lysosomes into the cytosol. Like these bacterial toxins, several members of the Bcl-2 family, including Bax and tBid, insert into lipid vesicles and planar lipid membranes, destabilize phospholipids bilayer, oligomerize and form channels. So far, only indirect support for this model exists; for instance, adding Bax, Bak and Bid to isolated mitochondria derived from liver or Hela cells results in permeabilization of the outer mitochondrial membrane, but the structure of the mitochondria is preserved. The second model suggests that Bcl-2 members interact with other proteins resulting in rupture of the outer membrane, while the inner membrane is conserved because of its larger surface area with its cristae.

Once released in the cytosol, cytochrome *c* binds Apaf-1 (apoptotic protease-activating factor-1) and activates procaspase 9 in the presence of dATP or ATP to form a complex designated apoptosome.[64] Activated caspase-9 can activate other caspases that ultimately destroy the cells. Fractionation of Hela cytosol revealed that three protein factors, Apaf-1, Apaf-2 and

Apaf-3, are necessary and sufficient to cause cell death. Apaf-2 has been identified as cytochrome *c* and Apaf-3 has been identified as caspase-9 while Apaf-1 has been identified as the human protein, homologous to the C. elegans cell death protein CED-4.[65]

1.4 ELECTROCHEMISTRY OF SEMICONDUCTOR NANOPARTICLES

1.4.1 Early Study of Semiconductor Nanoparticles

With the development and growth of human society, the demand for the energy grows. Solar energy is one of the most promising renewable forms of energy for the future. It has many unparallel advantages, such as low pollution and source unlimited. Semiconductor nanoparticles, such as TiO_2 and CdS, were first used to capture the solar spectrum.[66] It is necessary and interesting to understand the redox reactions at the nanoparticle surface by irradiation.

Early experiments of TiO_2 and CdS NPs in the dark and under illumination at a rotating disk electrode (RDE) demonstrated that these particles show the expected electrochemical behavior, such as mass transfer-controlled currents as a function of RDE rotation rate and current-potential curves that follow potential-controlled heterogeneous kinetics.[67,68] However, they were carried out with polydisperse preparations, so the unique molecular and nanoparticle nature of the systems could not be probed. Moreover, all of these studies were carried out in aqueous solutions, which limited the available potential window that could be explored, compared to the aprotic solvents used in later studies.

Films of discrete nanoparticles, as opposed to bulk films, have also been studied.[69,70] Because they provided much higher density particles on surface effect rather than being limited

to low concentrations of particles in solution, films have the advantage of yielding a large electrochemical signal. There have also been electrochemical studies of thicker films of nanoparticles, such as WO_3 and TiO_2.[71] For example, colloidal suspensions TiO_2 (particle size ~8 nm) were spin coated on ITO substrates in layers about 0.4 μm thick, and heated to 400 °C.[72] Repeated coatings and firings produced thicker films, up to 4 μm thick. A recent electrochemistry study demonstrated the capacitive and reactive properties of porous TiO_2 electrodes in an aqueous electrolyte.[73] Fundamental characteristics such as charge accumulation, charge transport, and interfacial charge were studied by voltammetry according to the competition between the different processes during the potential scan. Similarly, films of WO_3 (particle size 2 to 5 nm) up to 10 μm thick were prepared by drop coating and heating. Such films are of interest in electrochromic devices and in solar cells, but do not show the same effects as monolayers of nanoparticles.

1.4.2 Size Quantization Effects

A great deal of attention has been focused on the transformation from bulk material properties to molecular properties of various semiconductor nanoparticles.[74-76] Quantization in these nanoparticles arises from the confinement of charge carriers in the semiconductor with potential wells of small dimensions (less than the De Broglie wavelength of the electrons and holes). Under these conditions, the energy levels available for the electrons and holes in the conduction and valence bands become discrete. In addition to the very large effects on optical properties, size quantization also leads to major changes in the effective redox potential of the photogenerated carriers. Semiconductor particles that exhibit size-dependent optical and electronic properties are termed quantized particles or semiconductor clusters. Particles with

diameters greater than 15 nm typically behave as bulk semiconductors. However, similar prepared crystallites of approximately 1.5~5.0 nm diameter that possess a bulk lattice structure differ considerably in electronic properties.

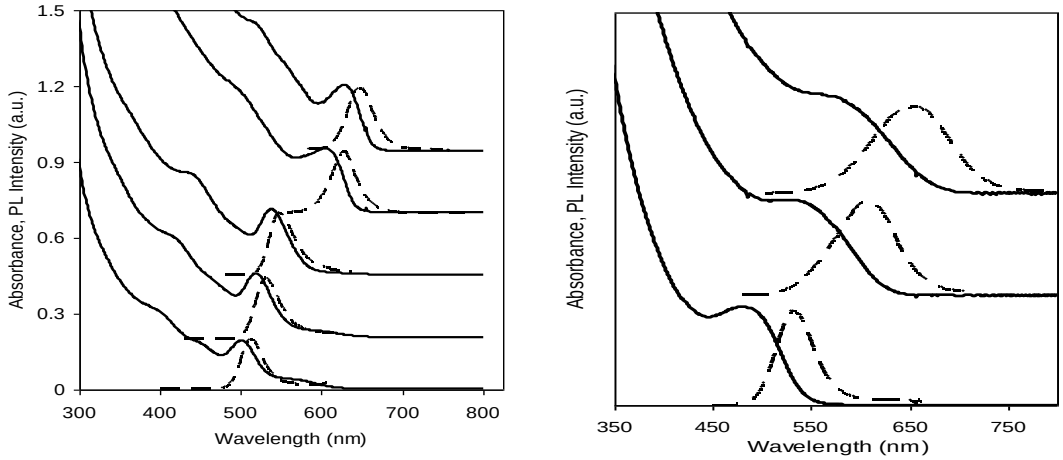

Figure 1.4 Normalized absorbance spectra (solid lines) and photoluminescence spectra (dashed lines, λ_{ex} = 400 nm) of five different sizes of CdSe nanoparticle samples in toluene (A) and three different sizes of CdTe nanoparticles samples in aqueous buffer (B); the curves for different NPs are shifted vertically for clarity.

Size quantization effects have been experimentally demonstrated in various laboratories around the world by controlling the synthetic procedure and monitoring the size-dependent optical effects.[10,77-79] Optical effects caused by size quantization in layered-type semiconductors have also been reported.[80-83] The absorption spectra of CdSe colloids of various particle sizes are compared in Figure 1.4. The absorption edge shifts to blue for smaller size particles as a result of the increase in the effective band gap.

Brus,[84,85] Henglein,[77] and Anderson[86] and co-workers have developed a quantum mechanical treatment to describe the various experimental results of wavelength threshold as a function of the diameter of CdS particles. A comparison of various models and the experimental results has been established. A plot of the wavelength of the onset of absorption versus the function of particle diameter seems to agree well with the proposed model. The majority of these

calculation start from the macroscopic solid state and determine the increase of the band gap with decreasing particle size on the basis of a particle-in-a-box assumption. The differences in the models lie in the complexity of the calculations and the boundary conditions. Efros et al. described the first calculation.[87] They used spherical, infinite potential wells and ignored the coulombic interaction. Brus et al. developed the energy levels of the first excited state by considering the coulombic interactions and polarization terms.[84,85] They showed that the coulombic interactions could not be ignored. However, comparison of the experimental results with different calculations showed that it is necessary to include finite barrier heights in the description of the experimental results.

1.4.3 Determination of Semiconductor Nanoparticle Band Positions

Among the mesoscopic properties of semiconductor nanoparticles, the size dependent bandgap of these particles is most prominent.[88] Detailed information about the bandgap can be determined by several spectroscopic methods such as absorption spectroscopy (AS), photoluminescence spectroscopy (PS), X-ray photoelectron spectroscopy (XPS), ultraviolet photoelectron spectroscopy (UPS), scanning tunneling microscopy (STM), deep-level transient spectroscopy (DLTS) and cyclic voltammetry (CV).[89] AS and PS provide only information about the energy of the bandgap, whereas XPS, UPS and CV are methods to measure absolute energy level position within the band structure. On one hand, the CV is an experimentally easy method that is especially suitable to examine semiconductor nanoparticles for their application in electrooptics like electroluminescent or photovoltaic devices.[90-97] On the other hand, it is a highly sensitive analytical method. It is possible to determine defect states in the band structure of the nanoparticles.[92]

Cyclic voltammetry is a dynamic electrochemical method, where current-potential curves are recorded at well defined applied potential depending on the scan rate. The electrochemical potentials found for reduction and oxidation provide information about the molecular orbital energies (Figure 1.5) and these can correlate with the band gap of the nanoparticles. By driving the electrode to more negative potential, the energy of the electrons is raised. If its energy is high enough, then it can transfer into vacant electronic states on the nanoparticles. In that case, a flow of electrons from electrodes to nanoparticles occurs. Similarly, the energy of the electrons can be lowered by imposing a more positive potential, and at some point electrons on nanoparticles will find a more favorable energy on the electrode and will transfer there. The measured oxidation potential of the nanoparticles correlates directly with the ionization potential I_p and the reduction potential with the electron affinity E_a. Because the vacuum level potentials of the common reference electrodes can be estimated, the band edge position of nanoparticles can be approximated.[98] Ideally, one peak couple of oxidation and reduction potential should appear in the CV measurement for the valence band (VB) and the conduction band (CB), respectively. Due to the fact that during the oxidation or reduction process charges are injected/taken to/from the material, reconfiguration of the structure may appear. Thus the onset values of oxidation as well as the reduction wave are considered as the bandgap edges. From previous work on CdSe nanoparticles films, it is known that this assumption leads to smaller bandgap values than allowed for the corresponding bulk material.[99] Hence, the values for all bandgap values were taken by considering the peak oxidation and reduction values.

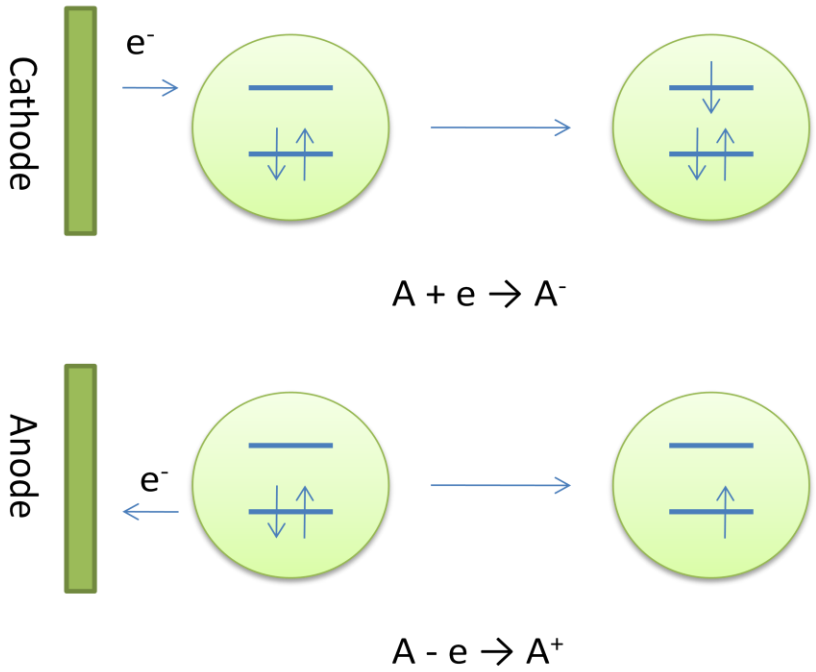

Figure 1.5 Schematic representation of electrochemical reduction and oxidation of a nanoparticle.

1.4.4 Electrochemical Reactions in Nanoparticles[100]

Several different paths are followed when an electron is injected or removed from a semiconductor nanoparticle:

Nanoparticle Charging. For elemental semiconductors, such as Si and Ge, as with Au nanoparticles, addition or removal of electrons can simply lead to charging of the nanoparticle. Multi-electron charging can continue until the field at the particle surface becomes sufficiently high to drive an electrochemical reaction.

Nanoparticle decomposition. The addition of charge can lead to reduction or oxidation reactions of the nanoparticle substituents. For example, for CdS

$CdS + 2e \rightarrow Cd + S^{2-}$ (electron injection)

$CdS - 2e \rightarrow Cd^{2+} + S$ (hole injection)

Nanoparticle doping. Charge added to the nanoparticle can be compensated for by moving an ion into the nanoparticle lattice. For example, the addition of an electron to WO_3 is compensated for by moving H^+ from solution into the semiconductor. This is sometimes called "n-doping". Hole injection could be compensated for by an anion, and this would constitute "p-doping".

1.4.5 Electrochemistry of CdSe NPs

CdSe NPs have been envisioned as material for photovoltaic and light-harvesting applications. However, few electrochemical data are reported for CdSe NPs, except for a thin film study by Guyot-Sionnest.[101] In that report, the quantitative electrochemical responses from the CdSe NP thin films, which were prepared using cross-linking molecules such as 3-mercaptopropyltrimethoxysilane and 1,6-hexanedithiol, was reported. The electrochemical kinetics and the stabilities of the films treated with cross-linkers were substantially improved compared with films prepared simply by drying on an ITO or Pt electrode.

On the other hand, differential pulse voltammetry (DPV) of 2.5 nm-diameter CdSe NPs was recently carried out.[102] NP reduction in the negative bias region was characterized by a doublet and then a continuous current increase when the applied potential became more negative, indicating two discrete charge transfers followed by multiple charge transfers. The doublet was assigned to the two consecutive electron injections to the first conduction band.[103] Additionally, two oxidation peaks were seen in the positive bias side of the DPV. These peaks were broader and the coulomb charging energy was larger than that of the negative side. These results were attributed to the higher density of valence levels and the close proximity between coulomb charging, level spacing as well as the multiplicity of the electronic structures. The

electrochemical gap was determined to be 2.34 eV from the separation of the first oxidation and reduction peaks in DPV. This is in good agreement with the optical band gap, 2.50 eV and 2.06 eV, estimated from the absorption onset and the broad PL peak of the NP, respectively.[102]

1.4.6 Electrochemistry of CdTe NPs

DPVs of two different batches of CdTe NPs were obtained by Bae et al.[104] In a 5:1 (v/v) benzene/acetonitrile mixture as a solvent, three anodic peaks were observed in the positive potential scan. Three cathodic peaks appear in the negative potential scan direction. The electrochemical band gap between the first anodic peak and cathodic peaks is 2.13 V, which is close to the value of 2 eV obtained spectroscopically. Recently, Gao and co-workers reported voltammetric current peaks of thioglycolic acid-stabilized CdTe NPs around -1 and +1 (vs. Ag/AgCl) in aqueous solution.[105] Similar voltammetric behavior was observed by Greene and co-workers from a solid film of dimethyldioctadecylammonium-stabilized CdTe NP monolayer.[106] They reported an electrochemical band gap that correlated with the optical value as well as anodic current peaks located at potentials inside the valence band edge, which were explained by hole injection into the surface traps of the particles. The diffusion coefficient of the NPs was estimated as being on the order of 10^{-6} cm^2/s.[104] The electrochemical behaviors of the synthetic precursor, like TOPO, $Cd(ClO_4)_2$, TOP and Te, were also investigated.[104]

1.4.7 CdSe and CdTe Sensitized Solar Cell[107]

Quantum dot-sensitized solar cells (QDSCs)[108-113] have drawn great attention recently to extend the latest dye-sensitized solar cells (DSSCs) invented by Grätzel. In the case of the QDSCs,

excited electrons of semiconductor NPs are injected into a large bandgap semiconductor such as TiO_2 or ZnO, and holes are scavenged by a redox couple. However, the overall power conversion efficiencies have remained below 5%.[114]

CdSe and CdTe bulk materials have bandgaps of 1.74 and 1.54 eV respectively. These characteristics make them ideal materials for harvesting near-infrared and visible photons in QDSCs. Low cost CdTe-based thin film solar modules are commercially manufactured by First Solar Inc. (Perrysburg, Ohio). In recent years, CdSe and CdTe NPs have been used as sensitizer to replace the dye molecules in QDSCs. By controlling the size of these semiconductor NPs, one can readily tune the band energies to efficiently capture the solar spectrum. CdSe NPs anchored onto TiO_2 NPs generate stable photocurrents during the operation of solar cells and power conversion efficiencies up to ~4.2% have been achieved.[115] Despite a successful module of CdTe/ CdSe heterojuction solar cell, the utilization of CdSe and CdTe NPs for solar energy conversion has been limited especially in photoelectrochemical cells with liquid electrolytes.[116-123]

Our research aims to link CdSe and CdTe NPs as dyads. Each dyad acts as a p-n junction with a tunable bandgap. To design such structures efficiently, one would like to know the position of the electronic states, both occupied and unoccupied, so that efficient charge separation can be made possible. In the study of chapter 4, the NPs are adsorbed onto a Au substrate that serves as an electrode. For any photoelectronic application, the energy of the HOMO (valence band) and LUMO (conduction band) of the NPs is of major importance. When NPs are adsorbed on electrodes the electrochemical potential of the solid and the NP layer come into equilibrium. Hence it is expected that the relative positions of the bulk electrode's Fermi level and the HOMO and LUMO of the NPs will adjust, and the adjustment will depend on the

properties of the interface and the size of the NPs. In a simple model, it is assumed that the HOMO-LUMO gap varies with size. To check the validity of the model, photoemission spectroscopy and cyclic voltammetry were applied.

In chapter 5 to explore the features of NPs, we have assembled monolayer and bilayer assembles of CdTe and CdSe nanoparticles (NPs) on Au electrodes using bifunctional surface modifiers of the type HS-R-HS. Absolute band gap positions were obtained from electrochemical measurements and photoemission measurements and they are discussed with regard to vacuum level values. Photophysical and photoinduced electron transfer processes that follow the excitation of the NP assemblies are probed by photoelectrochemical measurements. For bilayer assemblies of two different NPs on a Au substrate, the photocurrent response of the bilayer assemblies depends on the ordering of differently sized nanoparticles with respect to the surface.

References

(1) Marcus, R. A. *Advances in Chemical Physics*, *Volume 106* **1999**.

(2) Marcus, R. A. *J. Chem. Phys* **1956**, *24*, 966.

(3) Marcus, R. A. *J. Chem. Phys* **1957**, *26*, 1957.

(4) Marcus, R. A. *Discuss. Faraday Soc.* **1960**, *29*, 21.

(5) Markus, T. Z.; Wu, M.; Wang, L.; Waldeck, D. H.; Oron, D.; Naaman, R. *J. Phys. Chem. C* **2009**, *113*, 14200-14206.

(6) Dolla, A.; Blanchard, L.; Guerlesquin, F.; Bruschi, M. *Biochimie* **1994**, *76*, 471-9.

(7) Battistuzzi, G.; Borsari, M.; Sola, M.; Francia, F. *Biochemistry* **1997**, *36*, 16247-58.

(8) Cruanes, M. T.; Rodgers, K. K.; Sligar, S. G. *Journal of the American Chemical Society* **1992**, *114*, 9660-1.

(9) Yue, H.; Waldeck, D. H.; Petrovic, J.; Clark, R. A. *J. Phys. Chem. B* **2006**, *110*, 5062-5072.

(10) Kamat, P. V.; Murakoshi, K.; Wada, Y.; Yanagida, S. *Handb. Nanostruct. Mater. Nanotechnol.* **2000**, *3*, 291-344.

(11) Bigelow, W. C.; Pickett, D. L.; Zisman, W. A. *J. Colloid Interface Sci.* **1946**, *1*, 513.

(12) Ulman, A. *Chemical Reviews* **1996**, *96*, 1533-1554.

(13) Finklea, H. O. *Encyclopedia of Analytical Chemistry* **2000**, *11*, 10090-10115.

(14) Love, J. C.; Estroff, L. A.; Kriebel, J. K.; Nuzzo, R. G.; Whitesides, G. M. *Chemical Reviews (Washington, DC, United States)* **2005**, *105*, 1103-1169.

(15) Bain, C. D.; Troughton, E. B.; Tao, Y. T.; Evall, J.; Whitesides, G. M.; Nuzzo, R. G. *Journal of the American Chemical Society* **1989**, *111*, 321-35.

(16) Somorjai, G. A. *Chemistry in Two Dimensions - Surface*, Cornell University Press: Ithaca, New York, 1982.

(17) Nuzzo, R. G.; Fusco, F. A.; Allara, D. L. *Journal of the American Chemical Society* **1987**, *109*, 2358-68.

(18) Davis, K. L.; Drews, B. J.; Yue, H.; Waldeck, D. H.; Knorr, K.; Clark, R. A. *J. Phys. Chem. C* **2008**, *112*, 6571-6576.

(19) Yue, H.; Waldeck, D. H.; Schrock, K.; Kirby, D.; Knorr, K.; Switzer, S.; Rosmus, J.; Clark, R. A. *J. Phys. Chem. C* **2008**, *112*, 2514-2521.

(20) Lahiri, J.; Isaacs, L.; Tien, J.; Whitesides, G. M. *Analytical Chemistry* **1999**, *71*, 777-790.

(21) Petrovic, J.; Clark, R. A.; Yue, H.; Waldeck, D. H.; Bowden, E. F. *Langmuir* **2005**, *21*, 6308-6316.

(22) Sabatani, E.; Rubinstein, I. *The Journal of Physical Chemistry* **1987**, *91*, 6663-6669.

(23) Haddox, R. M.; Finklea, H. O. *The Journal of Physical Chemistry B* **2004**, *108*, 1694-1700.

(24) Pierrat, O.; Bourdillon, C.; Moiroux, J.; Laval, J.-M. *Langmuir* **1998**, *14*, 1692-1696.

(25) Hu, K.; Chai, Z.; Whitesell, J. K.; Bard, A. J. *Langmuir* **1999**, *15*, 3343-3347.

(26) Kumar, A.; Biebuyck, H. A.; Whitesides, G. M. *Langmuir* **1994**, *10*, 1498-1511.

(27) Willner, I.; Willner, B. *Coordination Chemistry Reviews* **2003**, *245*, 139-151.

(28) Miller, C. J. *Phys. Electrochem.* **1995**, 27-79.

(29) Barbara, P. F.; Meyer, T. J.; Ratner, M. A. *J. Phys. Chem.* **1996**, *100*, 13148-13168.

(30) Chidsey, C. E. D. *Science* **1991**, *251*, 919-922.

(31) Khoshtariya, D. E.; Dolidze, T. D.; Zusman, L. D.; Waldeck, D. H. *The Journal of Physical Chemistry A* **2001**, *105*, 1818-1829.

(32) Napper, A. M.; Liu, H.; Waldeck, D. H. *The Journal of Physical Chemistry B* **2001**, *105*, 7699-7707.

(33) Bertini, I.; Cavallaro, G.; Rosato, A. *Chemical Reviews (Washington, DC, United States)* **2006**, *106*, 90-115.

(34) Fedurco, M. *Coordination Chemistry Reviews* **2000**, *209*, 263-331.

(35) Scott, R. A.; Mauk, A. G.; Editors *Cytochrome c: A Multidisciplinary Approach*, 1996.

(36) Armstrong, F. A. *Struct. Bonding* **1990**, *72*, 137.

(37) Hawkridge, F. M.; Taniguchi, I. *Comments on Inorganic Chemistry: A Journal of Critical Discussion of the Current Literature* **1995**, *17*, 163 - 187.

(38) Wei, J.; Liu, H.; Khoshtariya Dimitri, E.; Yamamoto, H.; Dick, A.; Waldeck David, H. *Angewandte Chemie (International ed. in English)* **2002**, *41*, 4700-3.

(39) Zhu, H.; Snyder, M. *Current opinion in chemical biology* **2003**, *7*, 55-63.

(40) Lee, Y.-S.; Mrksich, M. *Trends in biotechnology* **2002**, *20*, S14-8.

(41) Yeh, S. R.; Rousseau, D. L. *Nature structural biology* **1998**, *5*, 222-8.

(42) Yeh, S.-R.; Han, S.; Rousseau, D. L. *Accounts of Chemical Research* **1998**, *31*, 727-736.

(43) Fedurco, M.; Augustynski, J.; Indiani, C.; Smulevich, G.; Antalik, M.; Bano, M.; Sedlak, E.; Glascock, M. C.; Dawson, J. H. *Journal of the American Chemical Society* **2005**, *127*, 7638-7646.

(44) Fedurco, M.; Augustynski, J.; Indiani, C.; Smulevich, G.; Antalik, M.; Bano, M.; Sedlak, E.; Glascock, M. C.; Dawson, J. H. *Biochimica et Biophysica Acta, Proteins and Proteomics* **2004**, *1703*, 31-41.

(45) Bixler, J.; Bakker, G.; McLendon, G. *Journal of the American Chemical Society* **1992**, *114*, 6938-9.

(46) Cheng, Y. Y.; Lin, S. H.; Chang, H. C.; Su, M. C. *Journal of Physical Chemistry A* **2003**, *107*, 10687-10694.

(47) Cheng, Y.-Y.; Chang, H.-C.; Hoops, G.; Su, M.-C. *Journal of the American Chemical Society* **2004**, *126*, 10828-10829.

(48) Goto, Y.; Calciano, L. J.; Fink, A. L. *Proceedings of the National Academy of Sciences of the United States of America* **1990**, *87*, 573-7.

(49) Evans, P. A.; Radford, S. E. *Current Opinion in Structural Biology* **1994**, *4*, 100-6.

(50) Roder, H.; Elove, G. A.; Englander, S. W. *Nature* **1988**, *335*, 700-4.

(51) Johnson, W. C., Jr. *Annual Review of Biophysics and Biophysical Chemistry* **1988**, *17*, 145-66.

(52) Lattman, E. E. *Current Opinion in Structural Biology* **1994**, *4*, 87-92.

(53) Elove, G. A.; Bhuyan, A. K.; Roder, H. *Biochemistry* **1994**, *33*, 6925-35.

(54) Elove, G. A.; Chaffotte, A. F.; Roder, H.; Goldberg, M. E. *Biochemistry* **1992**, *31*, 6876-83.

(55) Takahashi, S.; Yeh, S. R.; Das, T. K.; Chan, C. K.; Gottfried, D. S.; Rousseau, D. L. *Nature structural biology* **1997**, *4*, 44-50.

(56) Yeh, S.-R.; Takahashi, S.; Fan, B.; Rousseau, D. L. *Nature Structural Biology* **1997**, *4*, 51-56.

(57) Quinn, P. J.; Kagan, V. E.; Editors *Phospholipid Metabolism in Apoptosis: Subcellular Biochemistry, Volume 36. [In: Subcell. Biochem., 2002; 36]*, 2002.

(58) McMillin, J. B.; Dowhan, W. *Biochimica et Biophysica Acta, Molecular and Cell Biology of Lipids* **2002**, *1585*, 97-107.

(59) Jori, G.; Tamburro, A. M.; Azzi, A. *Photochemistry and photobiology* **1974**, *19*, 337-45.

(60) Mathews, C. K.; van Holde, K. E.; Ahern, K. G. *Biochemistry Addison Wesley Longman, 2000*, 1186 pp.

(61) Kerr, J. F.; Wyllie, A. H.; Currie, A. R. *British journal of cancer* **1972**, *26*, 239-57.

(62) Hengartner, M. O. *Nature (London)* **2000**, *407*, 770-776.

(63) Adams, J. M.; Cory, S. *Science (Washington, D. C.)* **1998**, *281*, 1322-1326.

(64) Li, P.; Nijhawan, D.; Budihardjo, I.; Alnemri, E. S.; Wang, X. *Cell (Cambridge, Massachusetts)* **1997**, *91*, 479-489.

(65) Zou, H.; Henzel, W. J.; Liu, X.; Lutschg, A.; Wang, X. *Cell (Cambridge, Massachusetts)* **1997**, *90*, 405-413.

(66) Frank, S. N.; Bard, A. J. *Journal of the American Chemical Society* **1977**, *99*, 303-304.

(67) Dunn, W. W.; Aikawa, Y.; Bard, A. J. *J Electrochemical Soc* **1981**, *128*, 222.

(68) Dunn, W. W.; Aikawa, Y.; Bard, A. J. *Journal of the American Chemical Society* **1981**, *103*, 3456-3459.

(69) Ogawa, S.; Fan, F.-R. F.; Bard, A. J. *The Journal of Physical Chemistry* **1995**, *99*, 11182-11189.

(70) Ogawa, S.; Hu, K.; Fan, F.-R. F.; Bard, A. J. *J Phys Chem* **1997**, *29*, 5707.

(71) Hotchandani, S.; Bedja, I.; Fessenden, R.; Kamat, P. *Langmuir* **1994**, *10*, 17-22.

(72) O'Regan, B.; Moser, J.; Anderson, M.; Graetzel, M. *The Journal of Physical Chemistry* **1990**, *94*, 8720-8726.

(73) Fabregat-Santiago, F.; Mora-Sero, I.; Garcia-Belmonte, G.; Bisquert, J. *The Journal of Physical Chemistry B* **2002**, *107*, 758-768.

(74) Henglein, A. *Chem. Rev* **1989**, *89*, 1989.

(75) Brus, L. *J. Phys. Chem.* **1986**, *90*, 2555-60.

(76) Weller, H. *Adv. Mater. (Weinheim, Fed. Repub. Ger.)* **1993**, *5*, 88-95.

(77) Weller, H.; Schmidt, H. M.; Koch, U.; Fojtik, A.; Baral, S.; Henglein, A.; Kunath, W.; Weiss, K.; Dieman, E. *Chem. Phys. Lett.* **1986**, *124*, 557-60.

(78) Hayes, D.; Schmidt, K. H.; Meisel, D. *J. Phys. Chem.* **1989**, *93*, 6100-9.

(79) Fischer, C. H.; Henglein, A. *J. Phys. Chem.* **1989**, *93*, 5578-81.

(80) Micic, O. I.; Li, Z.; Mills, G.; Sullivan, J. C.; Meisel, D. *J. Phys. Chem.* **1987**, *91*, 6221-9.

(81) Nozik, A. J.; Thacker, B. R.; Olson, J. M. *Nature (London)* **1985**, *316*, 51-3.

(82) Peterson, M. W.; Micic, O. I.; Nozik, A. J. *J. Phys. Chem.* **1988**, *92*, 4160-5.

(83) Peterson, M. W.; Nenadovic, M. T.; Rajh, T.; Herak, R.; Micic, O. I.; Goral, J. P.; Nozik, A. J. *J. Phys. Chem.* **1988**, *92*, 1400-2.

(84) Brus, L. E. *J. Chem. Phys.* **1983**, *79*, 5566-71.

(85) Brus, L. E. *J. Chem. Phys.* **1984**, *80*, 4403-9.

(86) Mohan, V.; Anderson, J. B. *Chem. Phys. Lett.* **1989**, *156*, 520-4.

(87) Efros, A. L. *Sov. Phys. Semicond. (Engl. Transl.)* **1982**, *16*, 772.

(88) Kucur, E.; Buecking, W.; Nann, T. *Microchim. Acta* **2008**, *160*, 299-308.

(89) Ogawa, S.; Fan, F.-R. F.; Bard, A. J. *J. Phys. Chem.* **1995**, *99*, 11182-9.

(90) Achermann, M.; Petruska, M. A.; Koleske, D. D.; Crawford, M. H.; Klimov, V. I. *Nano Lett.* **2006**, *6*, 1396-1400.

(91) Jun, S.; Jang, E.; Park, J.; Kim, J. *Langmuir* **2006**, *22*, 2407-2410.

(92) Kucur, E.; Buecking, W.; Giernoth, R.; Nann, T. *J. Phys. Chem. B* **2005**, *109*, 20355-20360.

(93) Liu, D.; Kamat, P. V. *J. Phys. Chem.* **1993**, *97*, 10769-73.

(94) Robel, I.; Subramanian, V.; Kuno, M.; Kamat, P. V. *Journal of the American Chemical Society* **2006**, *128*, 2385-2393.

(95) Steckel, J. S.; Zimmer, J. P.; Coe-Sullivan, S.; Stott, N. E.; Bulovic, V.; Bawendi, M. G. *Angew. Chem., Int. Ed.* **2004**, *43*, 2154-2158.

(96) Tang, A.-W.; Teng, F.; Gao, Y.-H.; Li, D.; Zhao, S.-L.; Liang, C.-J.; Wang, Y.-S. *J. Lumin.* **2007**, *122-123*, 649-651.

(97) Xuan, Y.; Pan, D.; Zhao, N.; Ji, X.; Ma, D. *Nanotechnology* **2006**, *17*, 4966-4969.

(98) Bard, A. J.; Faulkner, L. R. *Electrochemical Methods: Fundermentals and Applications; Second Edition* **2002**, *Wiley, New York.*

(99) Kucur, E.; Riegler, J.; Urban, G. A.; Nann, T. *J. Chem. Phys.* **2003**, *119*, 2333-2337.

(100) Bard, A. J.; Ding, Z.; Myung, N. In *Semiconductor Nanocrystals and Silicate Nanoparticles* 2005, p 1-57.

(101) Wang, C.; Shim, M.; Guyot-Sionnest, P.; Franck, J. *Science* **2001**, *291*, 2390.

(102) Zhou, J.; Zhu, J.; Brzezinski, J.; Ding, Z. *Can. J. Chem* **2009**, *87*, 386.

(103) Alperson, B.; Rubinstein, I.; Hodes, G.; Porath, D.; Millo, O. *Applied Physics Letters* **1999**, *75*, 1751-1753.

(104) Bae, Y.; Myung, N.; Bard, A. J. *Nano Lett.* **2004**, *4*, 1153-1161.

(105) Gao, M.; Sun, J.; Dulkeith, E.; Gaponik, N.; Lemmer, U.; Feldmann, J. *Langmuir* **2002**, *18*, 4098-4102.

(106) Greene, I. A.; Wu, F.; Zhang, J. Z.; Chen, S. *The Journal of Physical Chemistry B* **2003**, *107*, 5733-5739.

(107) Bang, J. H.; Kamat, P. V. *ACS Nano* **2009**, *3*, 1467-1476.

(108) Chong, S. V.; Suresh, N.; Xia, J.; Al-Salim, N.; Idriss, H. *J. Phys. Chem. C* **2007**, *111*, 10389-10393.

(109) Lee, H. J.; Yum, J.-H.; Leventis, H. C.; Zakeeruddin, S. M.; Haque, S. A.; Chen, P.; Seok, S. I.; Gratzel, M.; Nazeeruddin, M. K. *J. Phys. Chem. C* **2008**, *112*, 11600-11608.

(110) Leschkies, K. S.; Divakar, R.; Basu, J.; Enache-Pommer, E.; Boercker, J. E.; Carter, C. B.; Kortshagen, U. R.; Norris, D. J.; Aydil, E. S. *Nano Lett.* **2007**, *7*, 1793-1798.

(111) Mora-Sero, I.; Bisquert, J.; Dittrich, T.; Belaidi, A.; Susha, A. S.; Rogach, A. L. *J. Phys. Chem. C* **2007**, *111*, 14889-14892.

(112) Niitsoo, O.; Sarkar, S. K.; Pejoux, C.; Ruehle, S.; Cahen, D.; Hodes, G. *J. Photochem. Photobiol., A* **2006**, *181*, 306-313.

(113) Tena-Zaera, R.; Katty, A.; Bastide, S.; Levy-Clement, C. *Chem. Mater.* **2007**, *19*, 1626-1632.

(114) Shen, Q.; Kobayashi, J.; Diguna, L. J.; Toyoda, T. *Journal of Applied Physics* **2008**, *103*, 084304-5.

(115) Liu, D.; Kamat, P. V. *Journal of Electroanalytical Chemistry* **1993**, *347*, 451-456.

(116) Cao, X.; Chen, P.; Guo, Y. *J. Phys. Chem. C* **2008**, *112*, 20560-20566.

(117) Franzl, T.; Shavel, A.; Rogach, A. L.; Gaponik, N.; Klar, T. A.; Eychmueller, A.; Feldmann, J. *Small* **2005**, *1*, 392-395.

(118) Gross, D.; Susha, A. S.; Klar, T. A.; Da Como, E.; Rogach, A. L.; Feldmann, J. *Nano Lett.* **2008**, *8*, 1482-1485.

(119) Guldi, D. M.; Zilbermann, I.; Anderson, G.; Kotov, N. A.; Tagmatarchis, N.; Prato, M. *J. Mater. Chem.* **2005**, *15*, 114-118.

(120) Kampmann, A.; Lincot, D. *Journal of Electroanalytical Chemistry* **1996**, *418*, 73-81.

(121) Mathew, X.; Bansal, A.; Turner, J. A.; Dhere, R.; Mathews, N. R.; Sebastian, P. J. *J. New Mater. Electrochem. Syst.* **2002**, *5*, 149-154.

(122) McGregor, S. M.; Dharmadasa, I. M.; Wadsworth, I.; Care, C. M. *Opt. Mater. (Amsterdam)* **1996**, *6*, 75-81.

(123) Rogach, A. L.; Franzl, T.; Klar, T. A.; Feldmann, J.; Gaponik, N.; Lesnyak, V.; Shavel, A.; Eychmueller, A.; Rakovich, Y. P.; Donegan, J. F. *J. Phys. Chem. C* **2007**, *111*, 14628-14637.

2.0 DENATURATION OF CYTOCHROME *C* AND ITS PEROXIDASE ACTIVITY WHEN IMMOBILIZED ON SAM FILMS

This work has been published as Wang, Lei; Waldeck, David H. *J. Phys. Chem. C* **2008**, 112, 1351-1356

Abstract

This work uses cytochrome *c*, an electron carrier in the respiratory chain, as a model to probe how surface adsorption affects the folding of a protein. The electrochemical activities of the protein horse heart cytochrome *c* is studied under conditions where it is covalently attached onto a mixed carboxylic acid and hydroxyl terminated SAM, which covers a Au electrode's surface. Changing the pH of the electrochemical buffer solution changes the conformation of the cytochrome *c* and causes a change of the peak currents in cyclic voltammetry and a shift of the peak potential. In addition, the unfolded cytochrome *c* displays peroxidase activity; the apparent Michaelis-Menten constant K_m for cytochrome c at these surfaces has been determined to be 7.9 mM at pH 3 and 144.3 mM at pH 7.

2.1 Introduction

Cytochrome *c* is an electron carrier in the respiratory chain of mitochondria and has been studied extensively.[1] Despite almost 80 years of study and a vast accumulation of data, new facets of its biological role have been discovered recently.[2] In particular, cytochrome *c* plays an important role in apoptosis in which it acts to trigger the release of proapoptotic proteins into the cytosol and displays peroxidase behavior.[3] Upon interaction with anionic phospholipids, particularly mitochondria-specific cardiolipin (CL), cytochrome *c* loses its tertiary structure and its peroxidase activity dramatically increases.

Since the primary biological function of cytochrome *c* is to carry out oxidation-reduction reactions, it follows that measurements of the oxidation-reduction potentials and associated electron transfer kinetics are central to its understanding. The formal redox potential for the ferri/ferrocytochrome *c* couple in buffer solution at pH = 7 is 0.265 V versus NHE,[4] and is known to vary with temperature,[5] pressure,[6] electrolyte composition and ionic strength.[7] Although cytochrome *c* adsorbs strongly on Pt, Hg, Au, Ag and other electrodes, direct surface adsorption on the metal often results in significant conformational changes, protein unfolding and often its denaturation. Chemically modified electrodes, in particular with self-assembled monolayers(SAM), can be used to inhibit the denaturation and manipulate the protein's electroactivity,[8] however, at pH = 7, cytochrome *c* has a net positive charge of +5e to +6e. If SAMs composed of carboxylic acid-terminated thiols are used to present a negatively charged surface to the solution, cytochrome *c* can bind electrostatically to the SAM's exposed surface.[9] Such assemblies are used as a model for cytochrome *c in vivo*, where it binds electrostatically to membrane bound redox proteins, but allows the detailed study the electron transfer reaction.

When cytochrome *c* is in its native state, the heme pocket is wrapped by the peptide chain and protected from the solvent, even though it is located near the protein edge. When the folded structure of cytochrome *c* is perturbed by denaturants,[10] e.g. urea or guanidine hydrochloride, it displays peroxidase activity; unfolding renders cytochrome *c* a competent peroxidase.[3] Cheng and co-workers used optical absorption spectrometry to follow the pH induced protein unfolding of cytochrome *c*.[11] The Soret absorption peak is observed to shift from 409 nm to 397 nm as the pH of the solution decreases from 10 to 2.5, and it displays a sharp transition between pH 2.5 and 3.0. When cytochrome *c* is unfolded by lowering the pH, the heme pocket loses one of its axial ligand, causing the heme pocket to unwrap and expose the heme to solvent molecules. Easy access of solvent and H_2O_2 to the heme pocket facilitates the peroxidase activity and of the protein. For the denatured cytochrome *c*, adding H_2O_2 into the buffer solution causes a great enhancement of current, which is stable for some time and increases with the concentration of H_2O_2. This paper reports on pH induced denaturation of cytochrome *c* and its subsequent peroxidase activity, characterized by cyclic voltammetry.

Microperoxidase-11 (MP-11), which is obtained by proteolytic digestion of cytochrome *c*, consists of the protein's heme and the covalently attached eleven amino acids of its peptide chain, hence it provides a simple model for heme-containing enzymes. Despite the structural similarities between MP-11 and cytochrome *c*, the heme of the oligopeptide and the native protein differ substantially in their redox potentials.[12] The first electrochemical measurement of the direct electron transfer for MP-11 immobilized covalently at a gold electrode modified with cystamine was performed by Lotzbeyer et al,[12] and such monolayers have been used for bioelectrocatalytic reduction of H_2O_2 in aqueous solutions.[13] It should be noted that the electrocatalytic current for the reduction of H_2O_2 in aqueous solutions is observed at more

positive potentials than the apparent redox potential of MP-11 in aqueous solution. The reason for this potential shift is the formation of the Fe(IV) intermediate species in the presence of H_2O_2, *vide infra*.

This paper reports on the combined phenomena of the pH effect on the cytochrome *c* immobilized at SAM coated electrodes and its peroxidase activitiy. Cyclic voltammetry is used to monitor the redox reaction as cytochrome *c* is unfolded. Because of the structural similarities between cytochrome *c* and MP-11, increased peroxidase activities are expected, and observed, when cytochrome *c* is denatured.

2.2 Experimental Section

2.2.1 Chemicals

All reagents were used as received. All aqueous solutions were prepared with 18.3 MΩ cm^{-1} deionized water (Nanopure, Barnstead, Dubuque, IA). Horse heart cytochrome *c*, 16-mecaptohexadecanoic acid ($C_{15}COOH$) were purchased from Sigma. 14-mercaptotetradecanol ($C_{14}OH$) was synthesized as reported before.[8]

Phosphate buffer solution was made by mixing 10 mM potassium phosphate dibasic aqueous solution and 10 mM potassium phosphate monobasic aqueous solution and 10 mM phosphoric acid to the desired pH value. All the buffer solutions were stored below 5 ℃ to prevent bacteria from growing, and then they sat at ambient temperature for 1 hr before use.

Electrodes used in all experiments were gold ball electrodes made from gold wire (0.5 mm diameter,99.99%, Alfa Aesar).

2.2.2 Electrode Preparation

Gold ball electrodes. A gold wire (0.5 mm diameter, 99.99%) was cleaned by reflux in concentrated nitric acid (68-70%) at 130 °C overnight and then was washed with deionized

water. The tip of the gold wire was heated to form a ball of ~0.06-0.15 cm^2 surface area. The gold ball was reheated in the flame until glowing and then quenched in deionized water. This annealing process was performed more than 15 times to make a smooth gold ball. The exposed Au wire was sealed in a glass capillary tube, and the Au ball tip was annealed and cooled in a high-purity stream of Ar gas.

SAM solutions. For the pure carboxylic acid-terminated SAMs, the concentration of the solution is 2 mM in absolute ethanol. For the mixed carboxylic acid-terminated and hydroxyl-terminated $C_{15}COOH/C_{14}OH$ SAMs, the total concentration of the solution is 2 mM with the ratio of 1:1.

Immobilization of cytochrome *c*. Chemically modified electrodes were prepared by placing the gold ball electrodes into the SAM solution for overnight (> 12 hours). After that, the electrodes were taken out from the solution, rinsed with absolute ethanol, then rinsed with the supporting buffer solution (10 mM phosphate buffer pH 7), and finally dried by a stream of dry argon gas. To covalently immobilize cytochrome *c*, the modified electrodes were placed into a 5 mM CMC (1-cyclohexyl-3-(2-morpholinoethyl) carbodiimide metho-p-toluenexulfonate) solution in 100 mM phosphate buffer at pH 7 for half an hour to activate the carboxyl group in the SAM.[14] After the activation, the electrodes were rinsed with supporting buffer solution again and placed into 100 μM cytochrome *c* solution in 10 mM phosphate buffer pH 7 for 1 hour. To electrostatically immobilize cytochrome *c*, the carboxyl group activation step is skipped and the electrodes are placed directly into cytochrome *c* solution. After rinsing by buffer, these electrodes were immediately used in voltammetry studies.

Electrochemical Measurements. A computer-controlled CHI 618B electrochemical workstation (CH Instruments, Austin, TX) and a Faraday cage was used for all electrochemical

measurements. The three-electrode cell was composed of a platinum counter electrode, a Ag/AgCl (1 M NaCl) reference electrode, and the SAM-coated Au as a working electrode. The voltammetry measurements were performed in 10 mM phosphate buffer solution with different pH value under an argon atmosphere.

2.3 Results and Discussion

2.3.1 Folded protein. Figure 2.1A shows some cyclic voltammograms as a function applied potential scan rate for cytochrome *c* covalently attached onto a mixed $C_{15}COOH/C_{14}OH$ SAM at pH 7.5. For an electroactive reactant adsorbed at a surface that displays Nernstian behavior, the current-potential(i-E) curve should satisfy the following equation: [15]

$$i = \frac{n^2F^2\nu A\Gamma^* \exp[(nF/RT)(E-E^{0'})]}{RT\{1+\exp[(nF/RT)(E-E^{0'})]\}^2}$$

where n is number of electrons transferred, F is Faraday's constant, ν is the voltage scan rate, A is the electrode active area, Γ^* is the surface concentration of reactant, and $E^{0'}$ is the formal potential. For a redox couple that is immobilized on the electrode surface, the peak current is given by $i_p = \frac{n^2F^2}{4RT}\nu A\Gamma^*$. For the mixed $C_{15}COOH/ C_{14}OH$ SAM system, the observed current peak gives a surface coverage of $1.5 \pm 0.2 \times 10^{-12}$ mol/cm^2, when cytochrome *c* is in its native state at pH = 7.5 and using n=1. This result agrees with previous work,[7] and corresponds to submonolayer coverage of the protein.

As the potential scan rate increases, the separation of the peak-potentials becomes larger and the Full-Width-at-Half-Maximum (FWHM) for both cathodic and anodic peaks become broader, indicating that the redox reaction is quasi-reversible. The standard electrochemical rate constant k^0 can be extracted from the relationship between scan rate and peak separation by fitting with the Marcus model. Figure 2.1B shows a plot of peak shift, from the apparent formal

potential (E_p-E^0), versus the voltage scan rate along with the best fit by the classical Marcus theory for the electron transfer rate constant with a reorganization energy of 0.6 eV. The procedure provides a standard rate constant k^0 = 2.5 s^{-1} which matches well with the results of cytochrome *c* covalently attached to $C_{15}COOH/C_{14}OH$ mixed SAMs reported by Yue.[14] The FWHM is 92.3 mV at the lowest scan rate of 25 mV/s and is 194 mV at the highest scan rate of 1V/s. The FWHM for a reversible redox couple should be 90.6 mV and the value at 25 mV/s is within 2% of this limit.

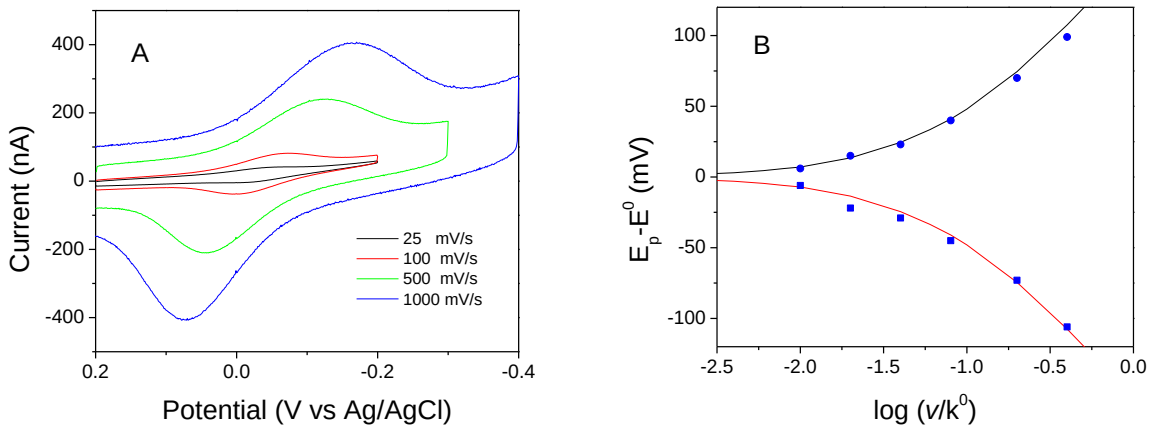

Figure 2.1 A) The figure shows cyclic voltammograms of covalently attached cytochrome *c* on mixed carboxylic SAM (50% $C_{15}COOH$ and 50% $C_{14}OH$) at different scan rates in 10 mM phosphate buffer, pH 7. B) The experimental peak separation is plotted as a function of scan rate. The circles ● are cathodic peak potential shift from the apparent formal potential, the squares ■ are anodic peak potential shift from the apparent formal potential, and the line is a fit by the Marcus model.

2.3.2 pH effect. The effect of pH on the electrochemical reduction and oxidation of ferricytochrome *c* is shown in figure 2.2A. As the pH decreases, the peaks become broader with a concomitant decrease in peak current. At pH = 4, the Faradaic peak current drops almost to zero. It is evident from these data that the amount of active His/Met-ligated protein decreases from 100% to almost zero upon decreasing the pH. By integrating the charge under the peak, the percentage of active His/Met-ligated protein at pH 6, 5 and 4 was determined to be 91%, 56%

and 5%, respectively. The fact that cytochrome *c* is covalently attached to the SAM rules out the possibility that cytochrome *c* is simply diffusing away. It was reported that the peak potential for pH-dependent reductive desorption of 11-mercaptoundecanoic acid SAM is in the range of -1.0 V to -0.9 when pH is changing from 12 to 4.[16] Hence, the COOH-terminated alkanethiol SAMs are stable within the experiment potential window from 0.3 V to -0.4 V in the acid condition. Spectroscopic studies demonstrate that orientation and conformational changes occur for cytochrome *c* as a function of pH.[17] Hence we infer that the change of pH induces an important change in conformation of cytochrome *c*, which causes the loss of electroactivity in the potential window.

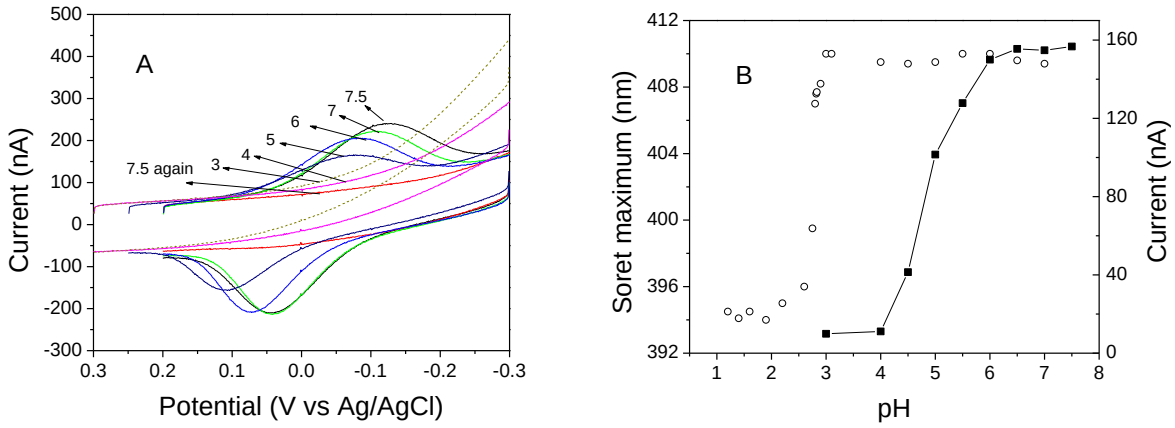

Figure 2.2 A) The figure shows cyclic voltammograms of covalently attached cytochrome *c* on mixed carboxylic SAM (50% $C_{15}COOH$ and 50% $C_{14}OH$) for different pH values. Scan rate: 500 mV/s. The dashed line voltammograms was obtained at pH 7.5 after the system had been exposed to pH 3. B) The anodic peak currents (■) are plotted as a function of pH. On the same graph, the ○ points represent the shift of the Soret bands of cyt *c* in free solution reported by Cheng.[17]

To provide a more complete picture, figure 2.2B shows the peak current's dependence on pH. The peak current decreases as the pH goes from high to low, and it has a sigmoidal shape. The peak currents of covalently immobilized cytochrome *c* decrease sharply with solution pH between 6 and 4; the midpoint of the transition is found between pH 4.5 and 5 which is 2 pH

units higher than that observed for the protein in solution.[17] This phenomenon indicates that cytochrome *c* immobilized on the surface is more vulnerable to denaturation by pH. This observed transition range of pH = 4 to 6 correlates well with the pK_a = 5.2 of histidine residues. The sudden decrease in peak current is attributed to unfolding of the cytochrome *c*, in particular changes in the heme pocket and its exposure to solvent.

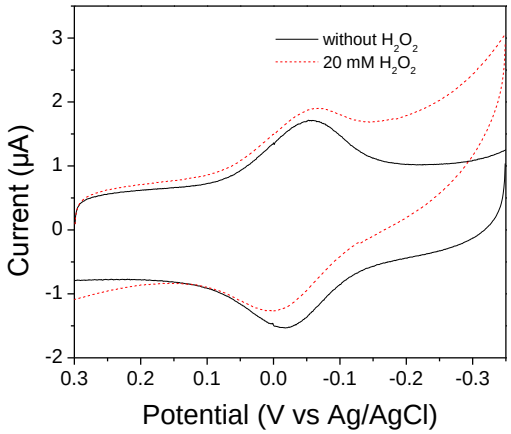

Figure 2.3 The figure shows cyclic voltammograms of immobilized cytochrome *c* at pH 7 phosphate buffer, both with (dashed line) and without (solid line) H_2O_2. Scan rate: 1 V/s.

When the pH is 3 both the anodic and cathodic peaks, which are associated with the electron transfer of the native protein, have disappeared. In addition, an enhanced current starts to appear at negative potential which is very sensitive to the trace concentration of oxygen in the solution. When the pH is back titrated to pH 7.5, only the charging current is observed, i.e., the native protein conformation is not recovered by changing the pH back after the denaturation. When the pH is low, the protein irreversibly loses its structure and can not be refolded by simply raising the pH.

2.3.3 Peroxidase acitivity. When cytochrome *c* is in its native state, the heme is protected from the solvent by the peptide pocket, even though it is located near the protein edge. When cytochrome *c* is unfolded by lowering the pH, the heme pocket unwraps and exposes the heme to

solvent molecules. This structural change presents the heme moiety to the solution and substrate, enabling peroxidase activity.

For the native protein at pH 7, addition of H_2O_2 into the buffer solution causes the current to increase slightly at negative biases (see figure 2.3). The cyclic voltammogram still displays the reversible one electron oxidation-reduction of the heme center, indicating that the electron transfer for native cytochrome *c* is not affected by H_2O_2.

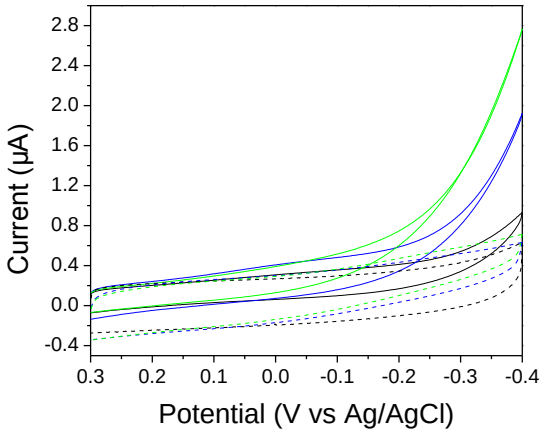

Figure 2.4 The figure shows cyclic voltammograms of at different concentrations of H_2O_2 in pH 3, 1M phosphate buffer, at a gold electrode with cytochrome *c* (solid line) and without cytochrome *c* (dash line). Scan rate: 500 mV/s. Black line 0 mM, blue line 5 mM, yellow line 10 mM H_2O_2.

Figure 2.4 shows the voltammetric behavior of the cytochrome *c* modified gold electrodes for different concentrations of H_2O_2 at pH 3. After adding H_2O_2 into the buffer solution, a significant enhancement of current was observed, and the current was stable over several scans. Moreover, the current increased systematically with the concentration of H_2O_2. The curves with dashed lines show control experiments in which no protein is present on the SAM at each of the different H_2O_2 concentrations. These voltammograms do not change significantly with the concentration of H_2O_2. The slight change of the current may be caused by the non-specific adsorption of H_2O_2 or its byproducts at the interface, changing the capacitance

and affecting the charging current. The concern that the increasing current arises from oxidation of the SAM by H_2O_2 can be excluded by this control experiment.

Other researchers have reported a similar phenomenon for microperoxidase-11 (MP-11), which consists of the active-site of cytochrome *c* obtained by proteolytic digestion of heme protein.[13,18] The electrocatalytic current rises at ca. 0.2 V with respect to Ag/AgCl (sat. KCl solution). It should be noted that the electrocatalytic current for the reduction of H_2O_2 in aqueous solution is observed much higher than the redox potential $E^{0'}$ = -0.398 V vs SCE of MP-11 itself. The reason for this potential shift is hypothesized to result from the formation of the Fe(IV) intermediate species in the presence of H_2O_2.[19,20] The reduction of the high-valency compound at +200 mV vs Ag/AgCl is compatable with the redox potentials for the Compound I/Compound II and Compound II/ Fe(III) couples of horseradish peroxidase, which are more positive than +900 mV vs NHE at pH 6.4.[21] The reaction mechanism is hypothesized to be:[22,23]

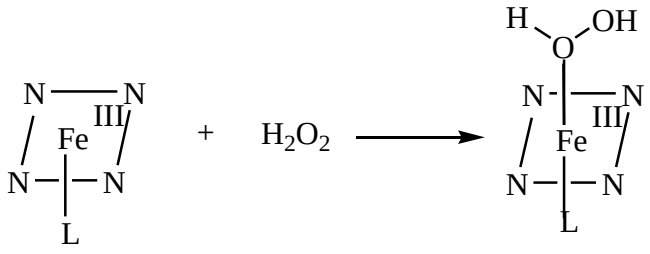

(1)

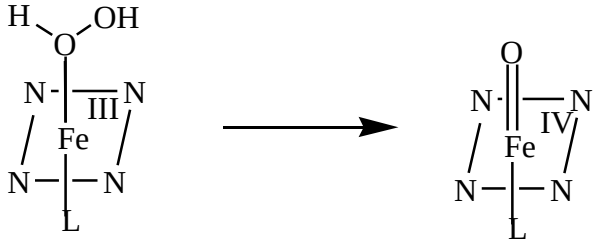

(2)

Compound I

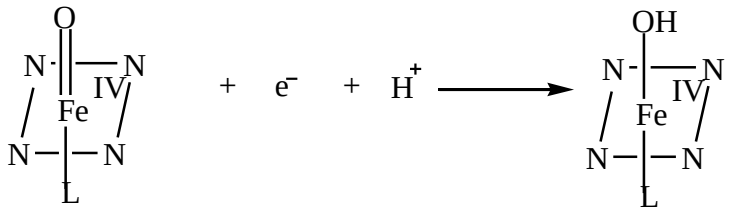

(3)

Compond II

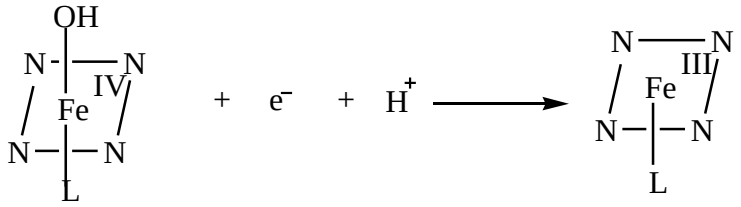

(4)

Figure 2.5A shows the steady-state current response to successive injection of 100 μL of 200 mM H_2O_2 into 20 mL pH 3 phosphate buffer solution while stirring. The H_2O_2 concentration in the bulk solution changes by about 1 mM for each injection. The catalytic peak current was measured at the potential of -0.5 V and clearly increases with the increasing amount of H_2O_2 injected. When H_2O_2 is added into the buffer solution, the catalytic current rises steeply until it reaches a stable value, the response time is less than 3 s because of the stirring. The apparent Michaelis-Menten constant K_m, which is an indication of the enzyme-substrate kinetics, can be calculated using a Lineweaver-Burk plot:[24]

$$\frac{1}{i_{cat}} = \frac{K_m}{i_{\max}} \cdot \frac{1}{C_{H_2O_2}} + \frac{1}{i_{\max}}$$

where i_{cat} is the electrocatalytic current, C_{H2O2} is the bulk concentration of H_2O_2, and i_{max} is the maximum current under saturated substrate conditions.

The reciprocal of the catalytic peak current was plotted versus the reciprocal of the substrate concentration (Figure 2.5B). The intercept of this plot yields a value for i_{max}, and the slope yields a value for K_m/ i_{max}, from which K_m can be obtained. The apparent kinetic

parameters of i_{max} and K_m are found to be 31.6 μA and 7.9 mM, respectively. The K_m is two orders larger than that found for MP-11 immobilized on a nanohybrid film[24] or gold electrode,[25] a significant peroxidase activity for denatured cytochrome *c*. This weak activity, in comparison to small peroxidases, is not surprising. Compared with MP-11 which only has a peptide of 11 amino acid residues, cytochrome *c* has 104 amino acid residues even though its heme pocket is exposed to the solvent, and this may sterically hinder the access of solvent and H_2O_2 molecules to the heme, hence lowering the electrocatalytic rate.

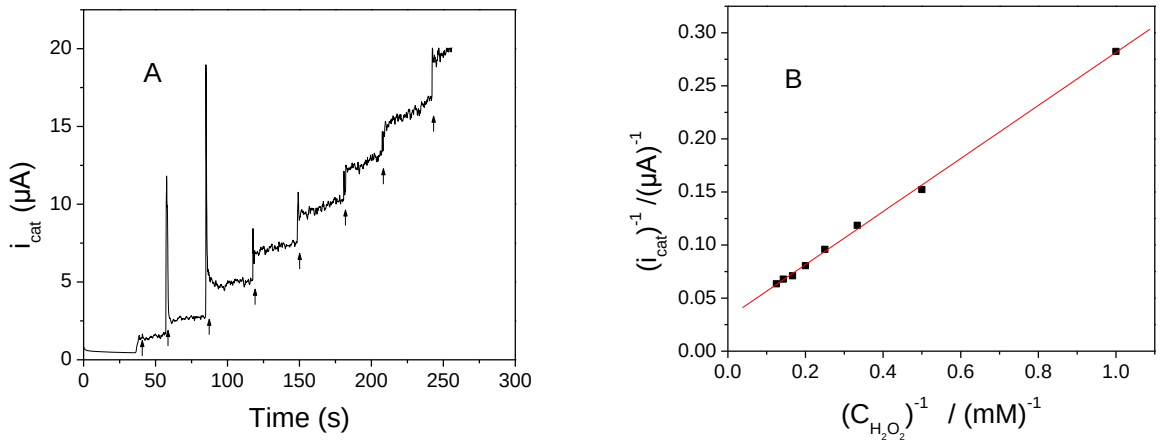

Figure 2.5 A) The figure shows the typical steady-state response of the cytochrome *c* immobilized electrode on successive injection of 100 μL of 200 mM H_2O_2 into 20 mL of pH 3 phosphate buffer solution. The arrows mark the points when an aliquot of peroxide was added. B) The currents observed in panel A were used here to make a Lineweaver-Burk plot (■). These data curve fit a line to yield the K_m and i_{max} parameters.

Figure 2.6 compares the peroxidase activity of denatured cytochrome *c* at two different pH values. The figure shows steady-state current response to addition of 100 μL of 1 M H_2O_2 into 20 mL of pH 3 and pH 7 phosphate buffer solutions under stirring, so that the H_2O_2 concentration in the bulk solution changes by about 5 mM for each injection. The surface coverage for both electrodes was estimated by integrating the charge associated with the electron transfer at pH 7 for the cytochrome *c* before it was denatured. From the Lineweaver-Burk plot, the K_m value for cytochrome *c* at pH 7 is 144.3 mM which is eighteen times larger than that at

pH 3. This is to say, at lower pH value, the peroxidase activity of cytochrome *c* is higher. When the H_2O_2 concentration is higher than 50 mM, the electrocatalytic current became unstable.

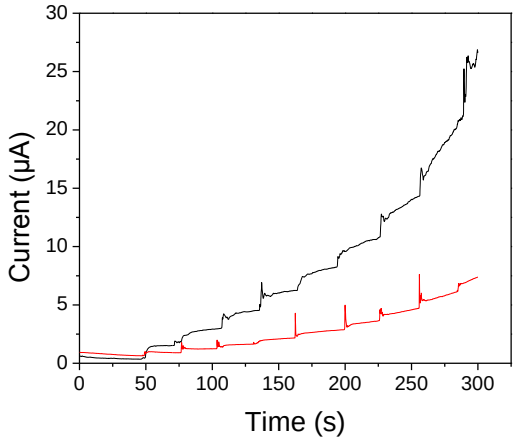

Figure 2.6 This figure shows the steady state current response of the cytochrome *c* immobilized electrode on successive injection of 100 μL of 1 M H_2O_2 into 20 mL of phosphate buffer solutions at pH 3 (black line) and at pH 7 (red line).

2.4 Conclusions

The present work uses a chemically modified gold ball electrode to explore how the unfolding of cytochrome *c* affects its electrochemistry. Covalently attaching cytochrome *c* onto mixed carboxylic acid and hydroxyl terminated SAM coated electrodes prevents the loss of cytochrome *c* during the experiment. The amount of immobilized cytochrome *c* onto the SAM is 1 to 2 pmol/cm^2, a surface coverage of 7%~10%.

Cyclic voltammetry allows one to monitor the redox reaction as cytochrome *c* unfolds with decreasing pH. The effect of pH on cytochrome denaturation is irreversible. As the pH decreases, the peak currents strongly decrease. At pH = 4, the Faradaic peak current drops almost to zero. The amount of active His/Met-ligated protein at pH 6, 5 and 4 was determined to be 91%, 56% and 5%, respectively, by integrating the charge under the peak. The midpoint of the transition is found between pH 4.5 and 5 which is two units higher than that reported for

cytochrome *c* in solution. This phenomenon indicates that the folded form of cytochrome *c*, which is covalently immobilized on the surface, is less stable than in solution, more vulnerable to a reduction in pH. The currents do not recover when the pH value is reversed.

When cytochrome *c* is in its native state, the heme pocket is wrapped by the peptide chain and protected from the solvent. When cytochrome *c* is unfolded by lowering the pH, the heme pocket loses its integrity and unwraps, exposing the heme to solvent molecules. Easy access to the heme pocket by the H_2O_2 substrate facilitates the heme's peroxidase activity and electrocatalytic current can be observed. The current increased with the concentration of H_2O_2 and the apparent Michaelis-Menten constant K_m was determined to be 7.9 mM and 144.3 mM for cytochrome *c* at pH 3 and pH 7 respectively, indicating that the peroxidase activity of denatured cytochrome *c* decreases at higher pH.

2.5 Acknowledgments

We thank NSF (CHE-0415457) for partial support of this work.

References

(1) Scott, R. A.; Mauk, A. G.; Editors *Cytochrome c: A Multidisciplinary Approach*, 1996.

(2) Kagan, V. E.; Tyurin, V. A.; Jiang, J.; Tyurina, Y. Y.; Ritov, V. B.; Amoscato, A. A.; Osipov, A. N.; Belikova, N. A.; Kapralov, A. A.; Kini, V.; Vlasova, I. I.; Zhao, Q.; Zou, M.; Di, P.; Svistunenko, D. A.; Kurnikov, I. V.; Borisenko, G. G. *Nature Chemical Biology* **2005**, *1*, 223-232.

(3) Basova, L. V.; Kurnikov, I. V.; Wang, L.; Ritov, V. B.; Belikova, N. A.; Vlasova, I. I.; Pacheco, A. A.; Winnica, D. E.; Peterson, J.; Bayir, H.; Waldeck, D. H.; Kagan, V. E. *Biochemistry* **2007**, *46*, 3423-3434.

(4) Dolla, A.; Blanchard, L.; Guerlesquin, F.; Bruschi, M. *Biochimie* **1994**, *76*, 471-9.

(5) Battistuzzi, G.; Borsari, M.; Sola, M.; Francia, F. *Biochemistry* **1997**, *36*, 16247-58.

(6) Cruanes, M. T.; Rodgers, K. K.; Sligar, S. G. *J Am Chem Soc* **1992**, *114*, 9660-1.

(7) Petrovic, J.; Clark, R. A.; Yue, H.; Waldeck, D. H.; Bowden, E. F. *Langmuir* **2005**, *21*, 6308-6316.

(8) Wei, J.; Liu, H.; Dick, A. R.; Yamamoto, H.; He, Y.; Waldeck, D. H. *J Am Chem Soc* **2002**, *124*, 9591-9599.

(9) Tarlov, M. J.; Bowden, E. F. *J Am Chem Soc* **1991**, *113*, 1847-9.

(10) Fedurco, M.; Augustynski, J.; Indiani, C.; Smulevich, G.; Antalik, M.; Bano, M.; Sedlak, E.; Glascock, M. C.; Dawson, J. H. *J Am Chem Soc* **2005**, *127*, 7638-7646.

(11) Cheng, Y.-Y.; Chang, H.-C.; Hoops, G.; Su, M.-C. *J Am Chem Soc* **2004**, *126*, 10828-10829.

(12) Loetzbeyer, T.; Schuhmann, W.; Katz, E.; Falter, J.; Schmidt, H.-L. *J Electroanal Chem* **1994**, *377*, 291-4.

(13) Loetzbeyer, T.; Schuhmann, W.; Schmidt, H.-L. *J Electroanal Chem* **1995**, *395*, 339-43.

(14) Yue, H.; Waldeck, D. H.; Petrovic, J.; Clark, R. A. *J Phys Chem B* **2006**, *110*, 5062-5072.

(15) Bard, A. J.; Faulkner, L. R. *Electrochemical Methods: Fundamentals and Applications*, 1980.

(16) Munakata, H.; Oyamatsu, D.; Kuwabata, S. *Langmuir* **2004**, *20*, 10123-10128.

(17) Cheng, Y. Y.; Lin, S. H.; Chang, H. C.; Su, M. C. *J Phys Chem A* **2003**, *107*, 10687-10694.

(18) Huang, W.; Jia, J.; Zhang, Z.; Han, X.; Tang, J.; Wang, J.; Dong, S.; Wang, E. *Biosensors & Bioelectronics* **2003**, *18*, 1225-1230.

(19) Traylor, T. G.; Xu, F. *J Am Chem Soc***1990**, *112*, 178-86.

(20) Baldwin, D. A.; Marques, H. M.; Pratt, J. M. *J Inorg Biochem* **1987**, *30*, 203-17.

(21) Hayashi, Y.; Yamazaki, I. *J Biol Chem* **1979**, *254*, 9101-6.

(22) Tatsuma, T.; Watanabe, T. *Anal Chem* **1991**, *63*, 1580-5.

(23) Van Rantwijk, F.; Sheldon, R. A. *Current Opinion in Biotechnology* **2000**, *11*, 554-564.

(24) Kamin, R. A.; Wilson, G. S. *Anal Chem* **1980**, *52*, 1198-205.

(25) Moore, A. N. J.; Katz, E.; Willner, I. *J Electroanal Chem* **1996**, *417*, 189-192.

3.0 CARDIOLIPIN SWITCH IN MITOCHONDRIA: SHUTTING OFF THE REDUCTION OF CYTOCHROME C AND TURNING ON THE PEROXIDASE ACTIVITY

This work has been published as Liana V. Basova, Igor V. Kurnikov, Lei Wang, Andy A. Pacheco, Vladimir B. Ritov, David H. Waldeck, Valerian E. Kagan, *Biochemistry* **2007**, 46, 3423-3434. The cyclic voltammetry study and analysis were performed by the thesis author.

Abstract

Upon interaction with anionic phospholipids, particularly mitochondria-specific cardiolipin (CL), cytochrome *c* (cyt *c*) loses its tertiary structure and its peroxidase activity dramatically increases. CL induced peroxidase activity of cyt *c* has been found to be important for selective CL oxidation in cells undergoing programmed death. During apoptosis, the peroxidase activity and the fraction of CL-bound cyt *c* markedly increases suggesting that CL may act as a switch to regulate cyt *c*'s mitochondrial functions. Using cyclic voltammetry and equilibrium redox-titrations, we show that the redox potential of cyt *c* shifts negatively by 350-400 mV upon binding to CL-containing membranes. Consequently, functions of cyt *c* as an electron transporter and cyt *c* reduction by complex III are strongly inhibited. Further, CL/cyt *c* complexes are not effective in scavenging superoxide anions and are not effectively reduced by ascorbate. Thus, both redox properties and functions of cyt *c* change upon interaction with CL in the mitochondrial membrane, diminishing cyt *c*'s electron donor/acceptor role and stimulating its peroxidase activity.

3.1 Introduction

Cytochrome *c* (cyt *c*) is a globular redox protein that shuttles electrons between respiratory complexes III and IV in mitochondria.[1,2] Despite almost 80 years of studies and a vast accumulation of data, new facets of its biological role have been discovered recently. One newly established function of cyt *c*, associated with its electron donor-acceptor properties, is realized during its interactions with superoxide.[3] In this capacity, cyt *c* assumes an antioxidant role by effective quenching of this oxygen radical.[4] Another newly discovered function of cyt *c*, which is not redox-related, is realized outside of mitochondria. After its release into the cytosol during apoptosis,[5,6] cyt *c* binds to Apaf-1 protein, causing its oligomerization and thus activates caspase cascades.[7]

Recently, we described another important role of cyt *c* in apoptosis in which it displays peroxidase behavior.[8] Cyt *c* acts as a catalyst for peroxidation of cardiolipin (CL), which is a mitochondria-specific anionic phospholipid, by hydrogen peroxide that is generated in the early stages of apoptosis. CL peroxidation contributes to the permeabilization of the outer mitochondrial membrane and the release of cyt *c* and other pro-apoptotic factors from the inter-membrane space into the cytosol. At later stages of apoptosis, the cytosolic cyt *c* catalyzes peroxidation of another anionic phospholipid, phosphatidylserine (PS), in the plasma membrane. Thus, it plays a part in PS externalization and generates an "eat-me" signal for clearance of apoptotic cells by macrophages.[9]

The involvement of cyt *c* in several intra-mitochondrial tasks suggests that a regulation mechanism exists to switch from the electron shuttling (or normal) function to the peroxidase (or apoptotic) function of the hemoprotein. Under 'normal' conditions complex III (cytochrome bc_1) located in the inner mitochondrial membrane reduces cyt *c*, while complex IV (cytochrome *c*

oxidase) oxidizes it.[1] Cyt *c* accepts electrons from complex III at a redox potential of about +250 mV while it donates electrons to Cu_A site in Complex IV at a redox potential of around +285 mV.[10] Any significant change of the redox potential of cyt *c* is likely to disrupt the electron transfer reactions and inhibit electron transport between the complexes. One potentially important distinction between the mitochondrial 'electron shuttle' pool of cyt *c* and the mitochondrial 'peroxidase' pool of cyt *c* is the association of the latter with CL.[8,11] The CL associated cyt *c* has a redox potential, which is significantly more negative than the 'native' form (*vide infra*). During apoptosis, the peroxidase activity and the fraction of CL-bound cyt *c* markedly increases. These findings suggest that CL acts as a switch to regulate cyt *c*'s mitochondrial functions; however, specific mechanisms through which this key function is realized remain to be elucidated.

Because porphyrin and two axial ligands (His-18 and Met-80) of iron in cyt *c* prevent direct interaction of hydrogen peroxide with the catalytic metal site, native cyt *c* in solution is a poor peroxidase.[12] In the presence of CL- (or PS-) containing liposomes, the peroxidase activity of cyt *c* increases by two orders of magnitude.[8,11,13] Apparently, increased peroxidase activity of cyt *c* upon its interaction with anionic membranes is associated with destabilization of its tertiary structure.[14-16] Although interactions of cyt *c* with negatively charged membranes have been examined in numerous studies,[17-21] the findings relevant to the redox properties of cyt *c* bound to anionic lipid membranes are conflicting. Tollin et al. reported a positive shift of the redox-potential of cyt *c* interacting with a CL-containing bilayer deposited on the surface of an electrode.[22] Wang et al. reported a small negative shift of the cyt *c* redox potential upon interaction with CL-containing lipid monolayers.[23] Electrochemical studies on metal electrodes

covered with anionic self-assembled monolayers (SAMs) reveal a significant negative shift of the cyt *c*'s redox potential.[24,25]

The redox potential of cyt *c* is critical to understanding its role in normally functioning mitochondria *vs* "death-machines" in apoptotic cells. Therefore, this in this work we examined the redox properties of cyt *c* in its complex with CL. The redox behavior of cyt *c* bound to anionic membranes was studied using two different approaches – direct electrochemistry of cyt *c* molecules bound to monolayers and redox titrations of cyt *c* bound to CL-containing liposomes. In addition, the effect of CL binding on the reduction potential of cyt *c* in liver and brain mitochondria, as well as on the regulation of electron transport activity in the mitochondrial electron transport chain, were examined by EPR and optical absorbance. The data show that binding of cyt *c* to CL causes: 1) a significant (~350-400 mV) negative shift of the redox potential of cyt *c*; 2) an inhibition of cyt *c* reduction in mitochondria, 3) an interruption of mitochondrial electron transport; and 4) an inability to oxidize superoxide and ascorbate.

3.2 Experimental section

Materials. Horse heart cyt *c* (type C-7752, purity of >95%), ascorbate, sodium hydrosulfite (dithionite), monobasic and dibasic sodium phosphate, Hepes, diethylenetriaminepentaacetic acid (DTPA), phosphate buffered saline (PBS), hydrogen peroxide (H_2O_2), ethylene glycol-bis (2-aminoethylether)-*N,N,N′,N′*-tetraacetic acid (EGTA), sucrose, Tris, 2-methyl-2-nitrosopropane (MNP), myxothiazol, alamethicin, mannitol, xanthine, xanthine oxidase, 7-carboxy-1-heptanethiol ($HOOC-(CH_2)_7-HS$), (1-cyclohexyl-3-(2-morpholinoethyl) carbodiimide metho-p-toluenesulfonate) $C_{14}H_{26}N_{30}C_7H_7O_3S$ - carbodiimide linker (CMC) were purchased from Sigma. 1,2-Dioleoyl-*sn*-Glycero-3-Phosphocholine (PC, DOPC), 1,1'2,2'-Tetraoleoyl Cardiolipin (CL, TOCL) were purchased from Avanti Polar Lipids Inc.

Small unilamellar liposomes were prepared using a tip sonicator (Ultrasonic, Homogenizer 4710 Series, Cole-Palmer-Instrument Co., Chicago, IL) as described on the website www.avantilipids.com. Liposomes were made from TOCL and DOPC (1:1 molar ratio) and DOPC alone in 20 mM sodium phosphate or Hepes buffers containing 100 μM DTPA, pH 7.4.

Cyclic Voltammetry (CV) was performed using a CH Instrument Electrochemical Analyzer 618B. The three-electrode electrochemical cell, which was used for collecting immobilized cyt *c* data, contained a platinum wire counter electrode, an Ag/AgCl (1 M KCl) reference electrode, and a SAM-modified gold working electrode. The Ag/AgCl reference electrode was calibrated against a saturated calomel electrode before experimentation. All redox potentials in the paper are reported versus the standard hydrogen electrode (SHE).

Electrode Preparation. A gold wire (0.5 mm diameter, 99.99%) was cleaned by reflux in concentrated nitric acid (68-70%) at 130^0C for 1 hour and then was washed with deionized water. The tip of the gold wire was heated to form a ball of ~0.06-0.15 cm^2 surface area. The gold ball was reheated in the flame until glowing and then quenched in deionized water. This annealing process was performed more than 15 times to make a smooth gold ball. The exposed gold wire was sealed in a glass capillary tube, and the gold ball tip was annealed and cooled in a high-purity stream of Ar gas.

Self-assembled monolayer (SAM) solutions. For the pure carboxylic acid-terminated SAMs, the concentration of the solution was 2 mM alkanethiol in absolute ethanol. For the mixed carboxylic acid-terminated and hydroxyl-terminated alkanethiols (seven methylenes) SAMs, the total concentration of the solution was 2 mM at a ratio of 1:1.

Immobilization of cyt c. Chemically modified electrodes were prepared by placing the gold ball electrodes into the SAM solution overnight. Subsequently, the electrodes were removed from the solution, first rinsed with absolute ethanol, then rinsed with the supporting buffer solution (10 mM sodium phosphate buffer, pH 7.0), and finally dried by a stream of dry argon gas. To covalently immobilize cyt *c*, the modified electrodes were placed into a 5 mM CMC solution in 100 mM sodium phosphate buffer at pH 7.0 for half an hour to activate the carboxyl group in the SAM. After the activation, the electrodes were rinsed with supporting buffer solution again and placed into 100 μM cyt *c* solution in 10 mM phosphate buffer pH 7.0 for 1 hour. To electrostatically immobilize cyt *c*, we skipped the carboxyl group activation step and directly placed the modified electrodes into the cyt *c* solution. After rinsing with buffer solution, these electrodes were immediately used in voltammetry studies.

Redox Titration. The absorbance spectra of cyt *c* at different dithionite concentrations were recorded on a Cary Bio 50 UV/Vis spectrophotometer. All dithionite titrations were performed in a glove box under strictly anaerobic conditions. Two redox dyes (mediators) were used in the titration experiments: gallocyanine (E^0=+20 mV)[26] and indigo carmine (E^0=-125 mV). Concentrations of reduced and oxidized forms of cyt *c* and mediators were obtained by least-squares fitting of the optical absorption spectra of the reaction mixture to a superposition of the individual optical spectra of the redox forms of the dyes, the liposomes, and the redox states of cyt *c* bound to liposomes at low and high lipids/protein ratios.

Isolation of Mitochondria. Mitochondria fractions were prepared by differential centrifugation of homogenate from rat liver and rat brain tissue.[27] Briefly, male Sprague–Dawley rats were perfused transcardially with ice cold phosphate-buffered saline, decapitated and the brains (minus cerebellum) were rapidly removed and placed in 10 V/w of ice cold 0.32 M

sucrose in 10 mM Tris buffer (pH 7.4). The tissue was homogenized in a Teflon/glass homogenizer (clearance 0.1–0.15 mm) by 10 gentle up and down strokes. The homogenate was spun at 1,000 g for 10 min to remove nuclei and cell debris. The resulting supernatant was centrifuged at 10,000 g for 20 min to obtain the crude mitochondrial pellet. The final pellet was washed with 2 ml of phosphate buffer saline and centrifuged (4 min, 10,000 g, 4 ℃). The pellet was frozen at -80 ℃ for later use. Liver mitochondria were isolated from male Sprague–Dawley rats using a percoll gradient as described previously.[8]

Complex III Enzymatic Activity. Ubiquinol:ferricytochrome *c* oxidoreductase (Complex III) activity was measured in the absence of detergent by a modification of the method by Gudz et al.[28] Reduction of cyt *c* by decylubiquinol was monitored by an increase in the absorbance at 550 nm at 30^{o}C. To provide access of cyt *c* to Complex III, a mitochondria suspension (in 0.32 M sucrose in 10 mM Tris buffer (pH 7.4)) was subjected to nitrogen cavitation. To achieve effective exchange of cyt *c* between complex III, which is bound in the inner mitochondrial membrane, and CL-containing liposomes, the outer mitochondrial membrane was mechanically (without detergent) removed. According to Storrie and Madden,[29] nitrogen cavitation in a mini-bomb (Model 4639, Parr Instrument Company; www.parrinst.com) at high nitrogen saturation (2,200 psi, 30 min) yields mitochondria without the outer membrane. After subjecting the mitochondria sample to high nitrogen saturation (more than 1,000 psi), the gas pressure was sharply dropped through the inlet valve. The nitrogen bubbles formed by the pressure release strip off the outer mitochondrial membrane.[29] The assay mixture (total volume 2 ml) contained 0.5 mM EGTA, 0.2 mg/ml bovine serum albumin, or TOCL (62 μM)/DOPC (125 μM) and DOPC (250 μM), 10 μM oxidized cyt *c*, 100 μM decylubiquinol, 2 mM NaN_3, and 25 mM KH_2P0_4, (pH 7.0 at 21^{o}C). The reaction was started after a 5-min pre-incubation by the

addition of an aliquot of mitochondrial suspension (20-50 μg mitochondrial protein). The activity was measured in the presence and in the absence of 2.5 μM myxothiazol, an inhibitor of the activity of complex III.[30] Ubiquinol:ferricytochrome *c* oxidoreductase activity was expressed in μmol of reduced cyt c/min/mg mitochondrial protein. Optical absorbances, with extinction coefficients of ε_{550} =1.9 x 10^4 M^{-1} cm^{-1} for free cyt *c* and ε_{550} = 1.6 x 10^4 M^{-1} cm^{-1} for CL-bound cyt *c*, were used to determine its concentrations. Decylubiquinol was prepared according to the method of Birch-Machin et al.[31]

Succinate-Oxidase Activity in mitochondria was measured after treatment with alamethicin using the assay of fumarase dehydrogenase reaction to oxidize fumarate in the presence of cyt *c* (10 μM) and TOCL (62 μM)/DOPC (125 μM) and DOPC (250 μM) liposomes. The incubation medium contained KCN.[32]

EPR Measurements. EPR spectra were recorded at room temperature on JEOL-REIX spectrometer with 100 kHz modulation (Kyoto, Japan). A 50 μL sample was placed in teflon tubing (0.8 mm internal diameter, 0.013 mm thickness) obtained from Alpha Wire Corp. (Elizabeth, NJ). The tubing was folded and placed in an open 3.0 mm internal diameter EPR quartz tube. EPR spectra of a reduced spin trap, MNP (MNP-H$^{\bullet}$, t-butyl hydronitroxide), were recorded at 3350 G, center field; 100 G, sweep width; 20 mW, microwave power; 0.79 G, field modulation; 4x10^3, receiver gain; 0.1 s, time constant; 4 min, scan time. The spectra of MNP-H$^{\bullet}$ are presented as an average of three recordings. The simulated spectra were generated using the WinSim program of the NIEHS public EPR software package (http://epr.niehs.nih.gov). The ascorbate radical EPR spectra were recorded under the following instrumental settings: 3350 G, center field; 10 G, sweep width; 10 mW, microwave power; 0.5 G, field modulation; 10^3, receiver gain; 0.03 s, time constant; 4 min, scan time. The time courses of ascorbate radical

generation were obtained by repeated scanning of the EPR spectrum (5 G, sweep width; other instrumental conditions were the same as above).

Cyt *c* Reduction by Ascorbate and Superoxide. The time course of cyt *c* reduction by ascorbate and superoxide generated in the xanthine/xanthine oxidase system[33] were recorded on a UV160U spectrophotometer (Shimadzu, Japan) in 1.0 cm pathlength cuvette. For both reactions, cyt *c* was preincubated (15 min) with TOCL/DOPC (1:1) liposomes. Ascorbate or xanthine was added to start the reaction and the absorbance at 550 nm was recorded for 10 and 5 min, respectively. The reference cuvette contained the same amount of liposomes.

Statistics. Data are expressed as means (SD of at least triplicate determinations. Changes in variables were analyzed by one-way ANOVA for multiple comparisons. Difference was considered significant at $p < 0.05$.

3.3 Results

3.3.1 Cyclic voltammetry of Cyt *c* in the Presence of CL. Cyclic voltammetry was used to characterize the redox properties of CL/cyt *c* complexes. Cyt *c* molecules were covalently attached to the terminal carboxyl functionalities of alkanethiol (seven methylenes) SAM coated gold electrodes. A typical cyclic voltammogram showed the reduction and oxidation peaks centered close to +220 mV (Figure 3.1a). The redox potential of cyt *c* on the anionic SAM is shifted by -40 mV *vs* that of cyt *c* in solution (+260 mV).[34] This shift is consistent with that reported earlier[25] and probably arises from the electrostatic field of negatively charged carboxylic groups of the SAM. Figure 1a shows the time-dependent changes of cyclic voltammograms of cyt *c* in the presence of TOCL-liposomes. Addition of CL-containing liposomes (TOCL/DOPC 1:1) resulted in gradual disappearance of the reduction peak at around +220 mV and the emergence of a new reduction peak at around -180 mV, over the course of an

hour (Figure 3.1a). The oxidation peak was also shifted to more negative potentials, by about 50 mV. Addition of pure DOPC liposomes did not result in changes of the position of either reduction or oxidation peaks of cyt *c*, however the capacitive current increased (Figure 3.1b). Apparently the TOCL interacts with the cyt c and causes a change in the cyt *c* redox-potential.

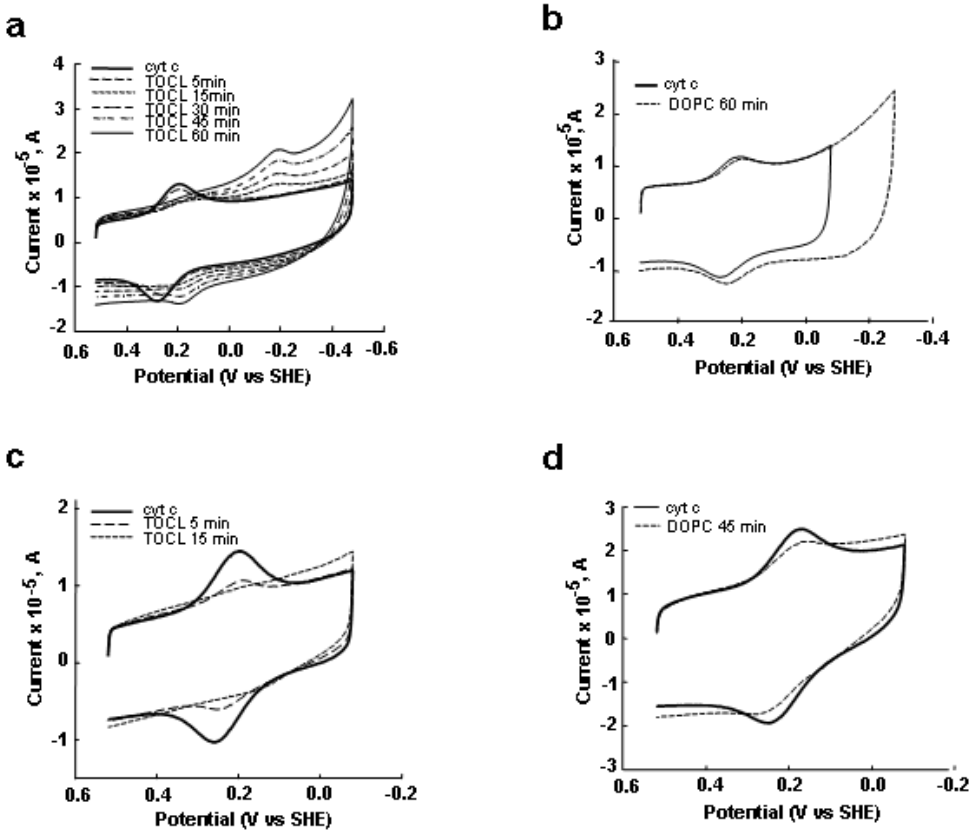

Figure 3.1 Cyclic voltammograms for cyt *c* covalently (a, b) and electrostatically (c, d) attached to carboxylic acid-terminated SAM covered gold electrodes in the presence of liposomes: 4 mM TOCL/DOPC 1:1 (a, c) and 4 mM DOPC alone (b, d). a) Changes of the voltammograms of cyt *c* in the presence of TOCL-liposomes were measured every 15 min during 60 min; b) cyt *c* in the presence of DOPC after incubation during 60 min; c) cyt *c* after incubation in TOCL liposomes during 5 and 15 min; d) cyt *c* in the presence DOPC after incubation during 45 min. The voltammograms of cyt *c* without liposomes (solid line) are shown for comparison on each figure. Measurements were performed in 10 mM phosphate buffer at pH 7.0 and a scan rate of 20 V/s.

Cyt *c*, which is noncovalently (i.e., electrostatically) adsorbed on the carboxy-SAMs, also showed a disappearance of the reduction and oxidation peaks at +220 mV (Figure 3.1c, broken

lines), however faster compared to covalently attached cyt *c*. No current was observed at negative potentials, likely because of desorption of the non-covalently attached TOCL/cyt *c* complexes from the electrode surface. The DOPC liposomes did not affect the redox peak positions of electrostatically attached cyt *c* (Figure 3.1d).

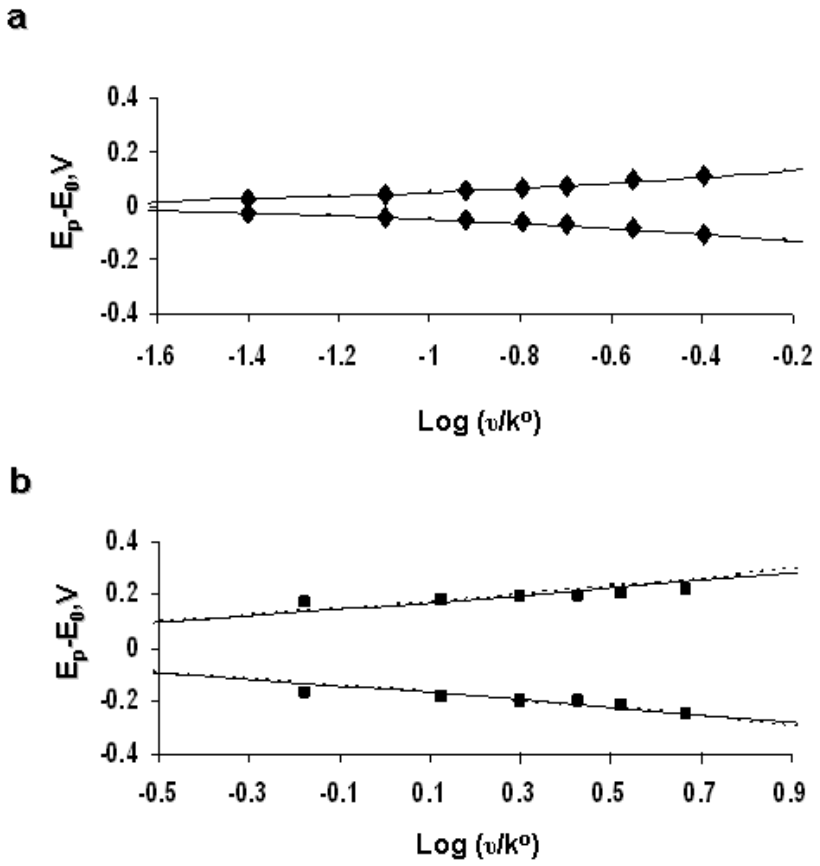

Figure 3.2 Dependence of the peak potential on the scan rate for the native cyt *c* (a) and cyt *c*/TOCL complex (b). Fits of the data to Marcus theory predictions are also shown for two different reorganization energies. See text for details.

The dependence of the reduction and oxidation peaks' position on the voltage scan rate can be used to characterize the standard electrochemical rate constant k^0 (This rate constant corresponds to $\Delta G=0$).[35,36] Figure 3.2 shows a plot of the peak shift from apparent formal potential (E_p-E^0) versus the logarithm of the voltage scan rate for native cyt *c* (Figure 3.2a) and TOCL/cyt *c* (Figure 3.2b) complexes. The separation of the current peaks at a scan rate of 20 V/s

is 80 mV for cyt *c* and 363 mV for cyt c in the presence CL, which demonstrates a slower rate constant for the protein exposed to CL. The solid curves show the best fit to the classical Marcus theory for the electron-transfer rate constant. For native cyt *c* the best fit is a reorganization energy of 0.6 eV and a rate constant (k^0) of 250 s^{-1}, which is in good agreement with previous work.[35,37] For cyt *c*/CL complexes the best fit reorganization energy is 1.0 eV, and the rate constant k^0 is 15 s^{-1}. Unless one can reach high overpotentials, this method, however, is not very sensitive to variations in the reorganization energy.

3.3.2 Redox Titration of Cyt *c* in the Presence of CL-Containing Liposomes. Although several research groups have studied the interaction of cyt *c* with different anionic phospholipids in liposomes,[11,13-23] the redox properties of cyt *c* in the presence of CL-containing liposomes have not been characterized. The redox behavior of cyt *c* under equilibrium conditions was determined by titrating it with sodium dithionite (E^0=-564 mV)[38] in the presence of indicator dyes (mediators) so that it could be followed optically. The cyt *c* in complex with CL-containing liposomes was titrated in the presence of gallocyanine redox dye. The standard redox potential of gallocyanine is +20 mV; thus at redox-potentials higher than ~+125 mV this dye is predominantly the oxidized form while at redox-potentials lower than -80 mV it is predominantly the reduced form. Figure 3.3a shows the titration results for different molar ratios of TOCL/cyt *c*, ranging from 25:1 to 200:1 at pH 7.0. For low concentrations of TOCL (TOCL/cyt *c* 25:1, 50:1), addition of dithionite stoichiometrically reduced cyt *c* while gallocyanine remained oxidized. After a certain amount of dithionite titrant, however, the reduction of cyt *c* almost completely stopped and did not resume until all of the gallocyanine was reduced. The titration results clearly showed the presence of two fractions of cyt *c* complexes. One fraction was reduced before the gallocyanine was reduced, thus it has a relatively high redox

potential (>+100 mV), while the other fraction was reduced after the gallocyanine was reduced so that it must have a more negative redox-potential (< -80 mV). Analysis of these titration curves shows that the fraction of cyt *c* with negative redox potential constitutes only about 20% of cyt *c* molecules at 25:1 CL/cyt *c* ratio, but that this fraction increases to more than 90% at 200:1 TOCL/cyt *c* ratio. Our previous studies demonstrated that increasing TOCL/cyt *c* ratios was associated with increased CL binding and denaturing of cyt *c*.[11] Hence, it is likely that the easily reduced fraction of cyt *c* corresponds to protein molecules in a native-like conformation, whereas the fraction of cyt *c* with the more negative redox potential corresponds to molecules partially denatured by the interaction with CL-containing liposomes.

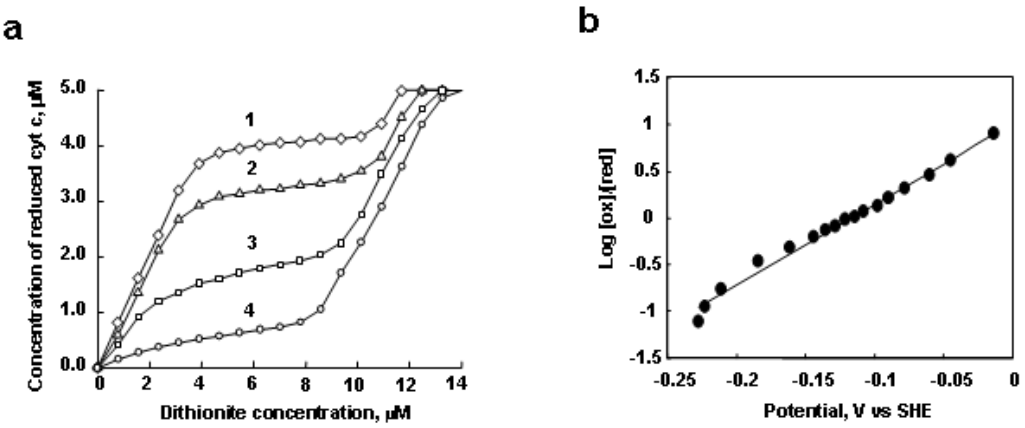

Figure 3.3 Redox titration of cyt *c* in the presence of TOCL by dithionite. a) Concentration dependence of reduced form of cyt *c* in the presence of TOCL and dithionite obtained by titration in the presence of gallocyanine (8 μM). The molar ratios of TOCL/cyt *c* were 25:1 (curve 1), 50:1 (curve 2), 100:1 (curve 3), 200:1 (curve 4); b) the Nernst plot obtained from spectro-electrochemical titration of cyt *c* (5 μM) in complex with TOCL at the molar ratio of 1:200 versus the potential range of indigo carmine (10 μM). b) Cyt *c* was incubated with liposomes for 15 min, and then a redox mediator was added. After this, titration by dithionite was started. 2 μL of stock solution of fresh dithionite (0.8 μM) was added 20 times, after each addition the absorbance spectra from 700 to 250 nm were measured. Each point represents addition of dithionite. Gallocyanine and indigo carmine were used as indicators of redox potential.

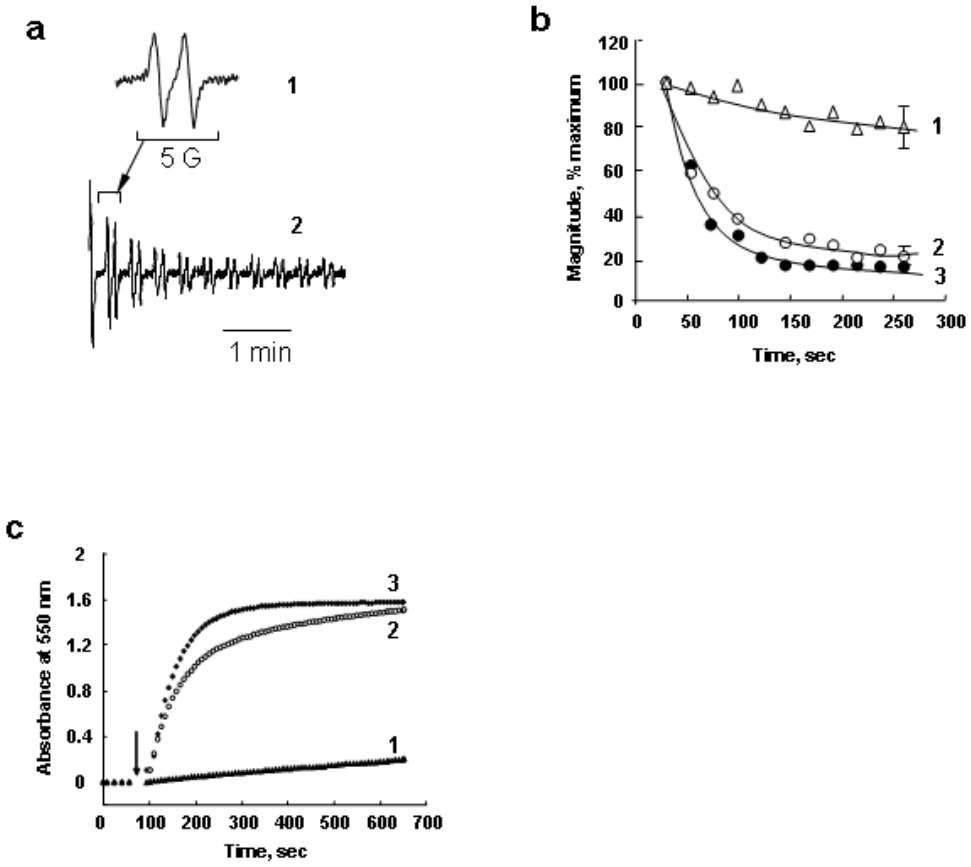

Figure 3.4 Effect of TOCL on cyt *c* reduction by ascorbate. a) EPR spectrum (1) and time course (2) of ascorbate radicals formed in the incubation medium containing cyt *c* and ascorbate (25 μM cyt *c*, 500 μM ascorbate, 20 mM phosphate and 100 μM DTPA, pH 7.4); b) time course of ascorbate radical generation in the absence (curves 3) or presence (curve 1, 2) of liposomes. Cyt *c* (25 μM) was incubated with DOPC or TOCL/DOPC liposomes (1 mM) for 5 min at 21^0C then ascorbate (500 μM) was added and recording of EPR ascorbate radical signal was started in 30 sec. Results are normalized to the initial ascorbate radical signal intensity taken as 100%. c) time course of cyt *c* reduction by ascorbate in the presence and absence of TOCL/DOPC (1:1) and DOPC liposomes monitored by absorbance at 550 nm. Cyt *c* (10 μM, buffer 20 mM phosphate and 100 μM DTPA) was pre-incubate with TOCL/DOPC 1:1 (400 μM) for 15 min at room temperature then ascorbate (200 μM) was added and absorbance was measured during 10 min (curve 1). Cyt *c* at the same concentration in the presence of ascorbate (curve 3) and DOPC (400 μM) liposomes (curve 2) are shown for comparison. Arrow indicates the time point when ascorbate was added.

To further characterize the redox-properties of the cyt *c* that is denatured by CL, we performed dithionite titration of cyt *c* bound to TOCL/DOPC liposomes (200:1 lipids/protein ratio) in the presence of another redox mediator, indigo carmine. Figure 3.3b shows that cyt *c*

bound to TOCL was gradually reduced as the redox-potential changed from -20 mV to -220 mV (computed from the molar ratios of the reduced and oxidized indigo carmine species). The dependence of $\log_{10}([cytc_{ox}]/[cytc_{red}])$ vs redox potential (Nernst Plot) is approximately linear over the range of the redox potentials probed, however the slope of the linear fit multiplied by 59 mV is 0.5 (±0.07), which differs substantially from the theoretical value of 1 that is expected from the Nernst equation for a one electron process. The unusually small value of the slope of the Nernst plot and a wide range (~200 mV) of redox potentials, over which the reduction of the membrane-bound cyt *c* occurs, indicates the presence of two or more sub-fractions in the low redox-potential (denatured) fraction of cyt *c* bound to TOCL/DOPC liposomes. These data are in line with other reports that describe several sub-fractions of the denatured cyt *c*, which differ in heme ligation.[18]

3.3.3 Reduction of Cyt *c*/CL Complexes by Ascorbate. Ascorbate is a universal reductant in cells[39] and biofluids; the redox potential of ascorbate is +58 mV,[38] i.e. significantly lower than that of cyt *c* (+260 mV).[34] Accordingly, ascorbate readily reduces cyt *c*. The reduction potential of TOCL/cyt *c* complexes is around -200 mV, it is unlikely that ascorbate can reduce the CL/cyt *c* complex. The reduction of cyt *c* in complex with TOCL by ascorbate were studied using two protocols: 1) we followed the one-electron reduction of ascorbate by the formation of its radical using EPR spectroscopy, and 2) we monitored cyt *c* reduction directly by its optical spectra. The typical doublet signal of ascorbate radical with a hyperfine splitting constant of 1.7 G was detected upon incubation of ferri-cyt *c* with ascorbate (Figure 3.4a, 1). The time course of the ascorbate oxidation was observed as a rapid decrease of the ascorbate radical signal (Figure 3.4a, 2; b, curve 3). In contrast, TOCL/cyt *c* complexes (20:1 molar ratio) oxidize ascorbate much less effectively (Figure 3.4b, curve 1). The slowing of the ascorbate oxidation rate by cytochrome c

seems to be specific for TOCL, since the presence of DOPC liposomes does not inhibit the process (Figure 3.4b, curve 2). In line with these results, ascorbate reduction of cyt *c* alone and cyt *c* pre-incubated with PC was effective and rapid (Figure 3.4c, curves 2 and 3 accordingly), whereas TOCL/cyt *c* complexes displayed very slow reduction by ascorbate (Figure 3.4c, curve 1). The rate of reduction of cyt *c* in the presence of CL decreased sixty times as found by the comparison of initial slopes of reduction curves in Figure 3.4c. The decrease in the observed reduction rate due to the presence of CL corresponds to the change of the second order rate constant for the reaction of ascorbate with cyt *c* from 2.1×10^5 $M^{-1}s^{-1}$,[40] to 3.4×10^3 $M^{-1}s^{-1}$. Thus the reduction of cyt *c* bound to CL is effectively blocked, in agreement with the drastic negative shift of redox potential of the cyt *c* in the complex with CL.

3.3.4 Interactions of CL/Cyt *c* Complexes with Superoxide. Because the redox potential of the O_2/O_2^- couple is about -130 mV,[41] i.e. comparable with that of TOCL/cyt *c* complexes (see above), it was important to test whether electron transfer is possible between superoxide and TOCL/cyt *c*. A superoxide-generating system, xanthine oxidase/xanthine, was used to assess the reduction of cyt *c*[33] and its complex with TOCL (Figure 3.5a). The data in Figure 3.5b shows that TOCL inhibited the reduction of cyt *c* by superoxide at TOCL/cyt *c* ratios >25:1, however less effectively than cyt *c* reduction by ascorbate. The observed rate of cyt *c* reduction dropped five times in the presence of CL (estimated by the comparison of initial slopes of reduction curves in Figure 3.5a). This decrease in reduction efficiency corresponds to a drop of the bimolecular rate constant for the reaction of the superoxide anion with cyt *c* from 2.1×10^5 $M^{-1}s^{-1}$,[42] to 4.2×10^4 $M^{-1}s^{-1}$. CL is less effective at inhibiting cyt *c* reduction by superoxide than for the reaction with ascorbate, consistent with the more negative potential of superoxide, compared to that of ascorbate.

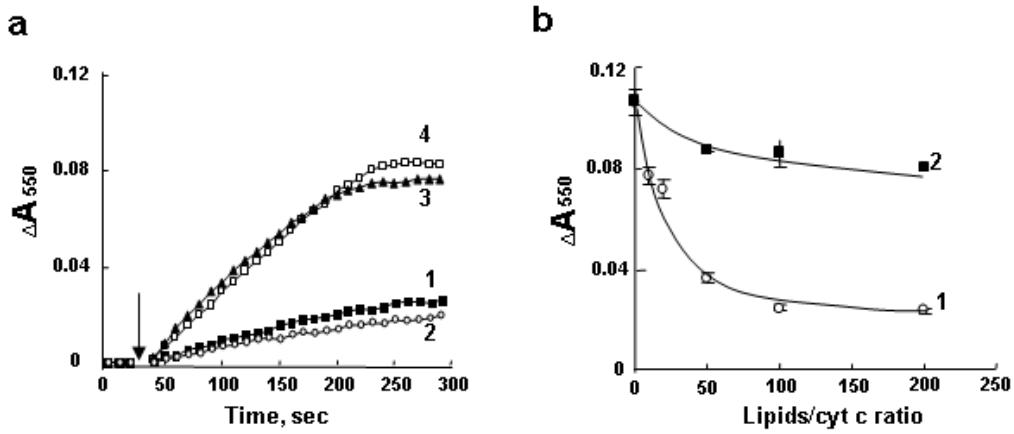

Figure 3.5 Cyt *c* reduction by superoxide radicals generated in xanthine/xanthine oxidase system. a) Time course of cyt *c* reduction by superoxide in the presence of TOCL/DOPC (curves 1,2) and DOPC (curve 3) liposomes and its absence (curve 4) monitored at 550 nm. Cyt *c* in the presence of DOPC (curve 3) and cyt *c* (curve 4) alone are shown for comparison. Arrow indicates the moment when xanthine oxidase was added; b) dependence of cyt *c* reduction by superoxide on lipids/cyt *c* ratio: TOCL/DOPC:cyt *c* 25:1 and 50:1 (curve 1,2 respectively), DOPC/cyt c 100:1 (curve 3) and cyt *c* alone (curve 4). b) Samples of cyt *c* (5 μM) were preincubated with TOCL/DOPC 1:1 liposomes at different concentrations for 15 min at room temperature in 20 mM Hepes buffer (plus 100 μM DTPA, pH 7.4). After the preincubation 25 μM xanthine (5 mM stock solution) was added and absorbance spectrum was recorded (the reference cuvette contained the same amount of liposomes). To start $O_2^{-\bullet}$ production xanthine oxidase was added (0.002 unit/ml). The time course of cyt *c* reduction was recorded every 10 sec measuring the absorption at 550 nm. After 5 min the total absorbance spectrum was recorded again. Differences between two spectra (ΔA_{550}) were calculated after alignment in 530-570 nm region.

3.3.5 Effects of CL on the Reduction of Cyt *c* by Complex III in Mitochondrial Membranes.

The first step in the interaction of ferri-cyt *c* with the electron transport chain is its reduction by Complex III. The latter participates in the electron transfer from coenzyme Q to cyt *c* and generates a proton-motive force during the Q cycle.[43] The effect of CL on the electron transfer between Complex III and cyt *c* was assessed by measuring the reduction of ferri-cyt *c* by decylubiquinol, which is catalyzed by Complex III (ubiquinol:ferri-cyt *c* oxidoreductase activity) in the inner membrane of mitochondria, in the presence of either DOPC liposomes or a mixture of TOCL/DOPC (1:1) liposomes. The time course of cyt *c* reduction was followed by absorbance at 550 nm (Figure 3.6). For rat liver mitochondria, the rate of cyt *c* reduction by decylubiquinol

decreased from 3.7±0.2 to 2.6±0.1 mU/min/mg protein in the presence of TOCL. Similarly, TOCL decreased the rate of cyt *c* reduction in rat brain cortex mitochondria (Figure 3.6b). In this case, the total ubiquinol:ferri-cyt *c* oxidoreductase activity dropped from 2.6±0.2 to 0.9±0.1 mU/min/mg protein in the presence of TOCL. The decreased activity of cyt *c* reduction by Complex III was determined using a specific Complex III inhibitor, myxothiazol.[44] Curves 3 and 4 in Figure 3.6b show that the reduction was much slower in the presence of the inhibitor than in its absence (curves 1 and 2). Further, the Complex III-mediated reduction of cyt *c* by decylubiquinol was also sensitive to TOCL. Curve 3 shows a significantly lower reduction rate than curve 4 (Figure 3.6b) suggesting that a strong competition for cyt *c* between CL and protein complexes in the mitochondrial respiratory chain.

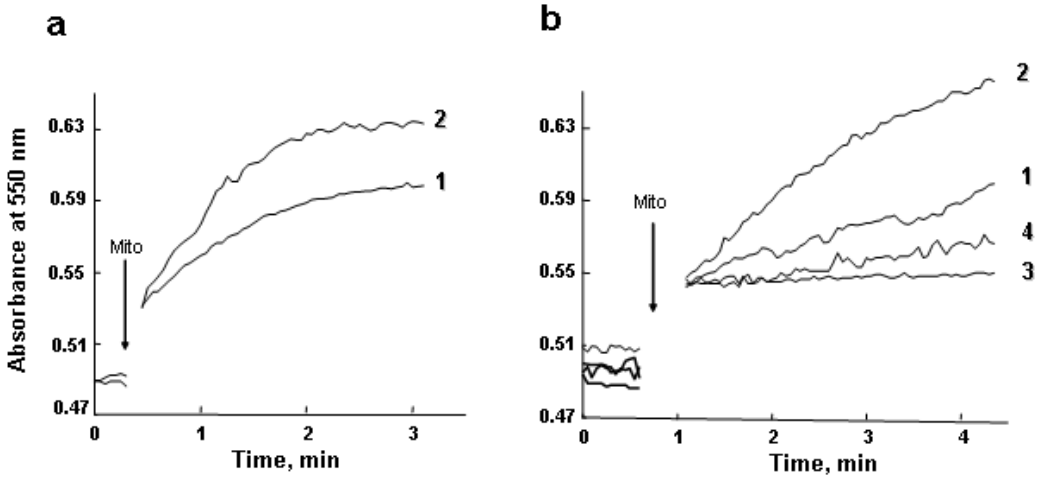

Figure 3.6 Effect of TOCL on the reduction of ferri-cyt *c* by decylubiquinol in the presence of rat liver (a) and brain (b) mitochondria. Assay mixture (total volume 2 ml) contained 0.5 mM EGTA, 0.2 mg/ml bovine serum albumin, TOCL (62 μM)/DOPC (125 μM) (a, curve 1, b, curve 1,3) and DOPC (250 μM) (a-curve 2, b-curve 2,4), 10 μM oxidized cyt *c*, 100 μM decylubiquinol, 2 mM NaN_3, and 25 mM KH_2P0_4, (pH 7.1 at 21^0C). The reaction was started after a 5-min pre-incubation by the addition of aliquot of mitochondrial suspension (20-50 μg mitochondrial protein). Arrow indicates the moment when mitochondria were added. The activity in brain mitochondria was also monitored in the presence of 2.5 μM myxothiazol (b), TOCL/DOPC (curve 3) and DOPC (curve 4) liposomes.

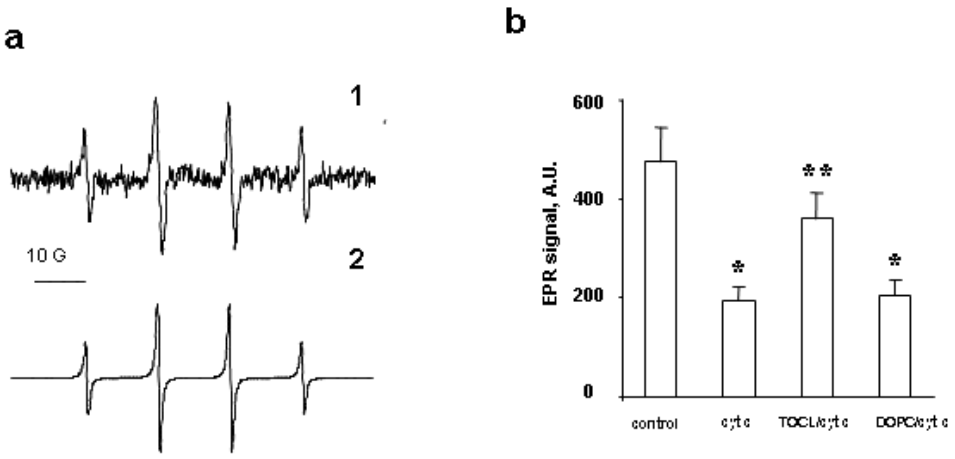

Figure 3.7 Effect of cyt *c* on EPR signal of MNP reduced to MNP-H• in rat liver mitochondrial suspension. Mitochondrial suspension (4 mg protein/ml) in buffer (230 mM mannitol, 70 mM sucrose, 20 mM Tris/HCl, 2.5 mM phosphate, 0.5 mM EGTA, pH 7.4) was supplemented with 20 mM MNP and succinate (7.5 mM). Spectra of reduced MNP (MNP-H$^{\bullet}$) were recorded 10 min after succinate addition. a) EPR spectrum of MNP-H$^{\bullet}$: (1) - an experimental spectrum, (2) – computer simulation using hyperfine coupling constants $a^N=a^H\beta=14.4$G. b) Magnitude of EPR signal of MNP-H$^{\bullet}$. Control: magnitude of MNP-H$^{\bullet}$ signal after addition of succinate to mitochondrial suspension. Cyt *c* (20 μM) with or without liposomes (400 μM total lipid) was added to mitochondria before addition of succinate. The results are representative of five independent experiments. Data are presented as mean ±S.E. (n=3) (*, $p<0.01$ *vs* control; **, $p<0.05$ *vs* cyt *c*).

3.3.6 Inhibition of Mitochondrial Electron Transport by CL. A substantial negative shift of the redox potential (by 350-400 mV) of TOCL/cyt *c* complexes causes the failure of its reduction by decylubiquinol via complex III (see above), and implies that the CL/cyt *c* complex can not operate as an effective electron shuttle in the mitochondrial respiratory chain. To test this hypothesis, we studied the effects of exogenously added TOCL on succinate-dependent electron transport through respiratory complexes of mitochondria using two different approaches. In the first one, we examined succinate-dependent reduction of a spin trap, MNP, to MNP-H•.[45] We employed mitochondria with their outer membrane mechanically removed by the nitrogen cavitation protocol (see above). After addition of succinate to mitochondria incubated in the presence of MNP, a typical four-line EPR spectrum of the MNP-H• radical was observed (Figure 3.7a) – in line with the known one-electron reduction of MNP by mitochondrial electron

transport.[45] Expectedly, the magnitude of the signal (concentration of MNP-H•) increased over 10 min.[46,47] Thus, succinate induced reduction of MNP occurred in the absence of endogenous cyt c washed away from the inter-membrane space during the removal of the outer membrane (Figure 3.7b). Addition of exogenous cyt *c* resulted in a significant decrease of the signal intensity. Cyt *c* added along with TOCL/DOPC liposomes, was much less efficient in quenching of the MNP-H• signal. Without TOCL, DOPC liposomes did not affect cyt *c* dependent quenching of the succinate induced signal. These results demonstrate that the electron acceptor function of cyt *c* in mitochondria was impaired by CL.

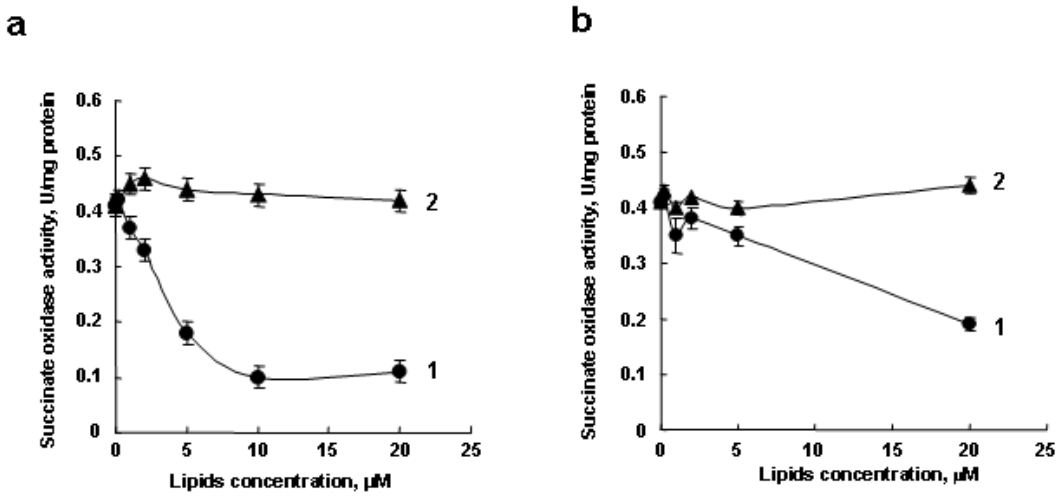

Figure 3.8. Effects of phospholipids on succinate oxidase activity of mouse liver (a) and brain (b) mitochondria. Curves 1 (a, b) were obtained in the presence of different concentration of TOCL-containing liposomes, curve 2 (a, b) - in the presence of DOPC liposomes. For experimental details see Methods section.

We further tested effects of TOCL on succinate-dependent electron transport through respiratory complexes of liver and brain mouse mitochondria (Figure 3.8). Electron-transport (succinate oxidase) activity in mitochondria was measured before and after treatment with alamethicin, which is known to permeabilize mitochondrial membranes and remove loosely (electrostatically) bound cyt *c* from mitochondria. Alamethicin caused almost complete

inhibition of succinate oxidase activity. This was accompanied by a removal of most (~85 %) cyt *c* from mitochondria, in line with previously published results.[32,48,49] For both liver and brain mitochondria, the electron transport activity could be fully restored by exogenously added cyt *c*. When TOCL/DOPC were added along with cyt *c*, however, the reconstitution of succinate oxidase activity was incomplete and dependent on the amount of TOCL. DOPC had essentially no effect on succinate oxidase activity of alamethicin-treated mitochondria reconstituted with exogenously added cyt *c*. These results suggest that interaction of cyt *c* with CL inhibits cyt *c*'s ability to effectively participate in electron transport.

3.3.7 Cyclic Voltammetry of Peroxidase Reaction Catalyzed by Cyt *c* in the Presence of CL. The peroxidase activity of cyt *c* and its dependence on CL was studied by cyclic voltammetry of cyt *c* covalently attached to SAM covered gold electrodes (Figure 3.9). Addition of H_2O_2 resulted in a concentration-dependent decrease of magnitudes of +220 mV oxidation and reduction peaks and appearance of reduction and oxidation peaks at -180 mV potential (data not shown). A probable interpretation of these observations is that the chemical modification of cyt *c*, as a result of the peroxidase reaction, reduces the protein stability so that it is more vulnerable to denaturation by the anionic SAM. The position of the reduction wave for cyt *c* reacted with H_2O_2 was similar to the reduction wave of cyt *c* modified by the interaction with TOCL, however, the oxidation peak of cyt *c* reacted with H_2O_2 was observed at a potential of ~-150 mV while TOCL/cyt *c* complexes were oxidized around +100 mV. Apparently, the reduction of chemically intact cyt *c* denatured by CL is accompanied by a conversion of cyt *c* into a native-like conformation, with respect to the heme pocket. In contrast, cyt *c* molecules chemically damaged by H_2O_2 are not refolded by heme reduction.

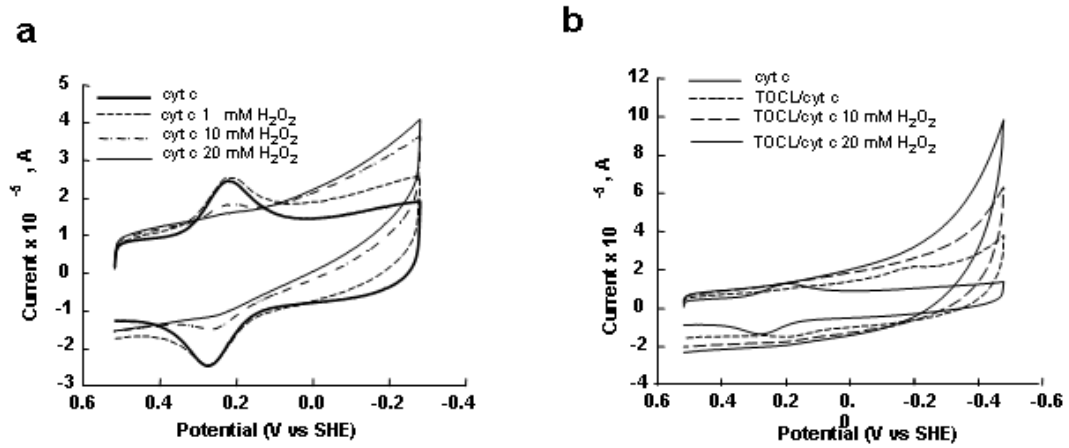

Figure 3.9. Cyclic voltammograms of cyt *c* covalently attached to SAM at different concentrations of H_2O_2 in the absence (a) and presence of TOCL/DOPC liposomes (b). Cyt *c* was incubated with liposomes during 60 min and then H_2O_2 was added. The voltammograms were recorded after pre-incubation with H_2O_2 during 15 min under N_2. The voltammograms of cyt *c* without liposomes at pH 7.0 are shown for comparison on both figures (solid line). Scan rate 20 V/s.

At higher H_2O_2 concentrations, a complete disappearance of the native cyt *c* redox waves was observed along with the appearance of H_2O_2 concentration-dependent reduction waves at the negative potentials (Figure 3.9a). Apparently, reactive compounds I and II of cyt *c*, formed as a result of the peroxidase reaction, were quickly reduced, perhaps by neighboring reduced cyt *c* molecules. Consequently, the concentration of the oxidized (and denatured) forms of cyt *c* increased resulting in a greater amplitude of the reduction wave at the negative electric potentials. The peroxidase activity of cyt *c* in the presence of TOCL was higher than in its absence (compare the current in the negative potential region to the peak current of the reversible cyt *c* wave in Figures 3.9b and 3.9a).

3.4 Discussion

3.4.1 CL as a Switch of Cyt *c* Peroxidase Activity. Our previous work has identified CL/cyt *c* complexes as important components of mitochondrial machinery that are triggered by pro-apoptotic stimuli and initiate the release of pro-apoptotic factors, including cyt *c*[8] This engages

subsequent segments of the cell death program such as caspase cascades. The essential redox function of CL/cyt *c* complexes is realized through their specific peroxidase activity directed towards oxidation of polyunsaturated molecular species of CL and accumulation of CL oxidation products, which act as pro-apoptotic signals in mitochondria.[8] The molecular switch that turns off the electron shuttling function of cyt *c* and turns on its peroxidase activity was not specifically identified, however. It is tempting to speculate that the same CL that binds cyt *c* and causes its partial unfolding acts as the switch playing this important role.

This work demonstrates that the redox potential of cyt *c* changes by about -350-400 mV upon its interaction with CL-containing phospholipid membranes. Redox titration experiments showed the simultaneous presence of two fractions of cyt *c* in the complex with CL: one - readily reducible - with a native-like redox-potential, and the second fraction – more resistant to reduction - with a more negative redox potential. The population of the protein fraction resistant to reduction grew with the increase in lipid/protein ratio and apparently corresponded to cyt *c* molecules unfolded by interactions with CL membranes, previously identified by tryptophan fluorescence measurements in similar conditions.[11] The redox titration also showed that the reduction-resistant fraction of cyt *c* bound to CL (denatured cyt *c* molecules) was heterogeneous and consisted of two or more sub-fractions, reduceable over a wide range of redox potentials between -50 and -200 mV. This finding is consistent with an analysis by Hildebdrandt et al.[18] who showed that fractions of cyt *c* denatured on Ag electrodes with different ligation (in Hildebrandt's classification penta-coordinate B2/5cHS and hexa-coordinate B2/6cLS) have different redox-potentials (in the range of -93 mV and -143 mV, respectively).

Our results established that CL prevents reduction of cyt *c* by complex III, ascorbate, and superoxide and blocks its participation in mitochondrial electron transport. The inhibitory effects

of CL were concentration-dependent, in agreement with our finding of two fractions of CL/cyt *c* with drastically different redox-properties. Our assessments of ubiquinol:ferri-cyt *c* oxidoreductase showed that CL can compete with complex III for cyt *c*. Therefore, operation of the electron transport chain in mitochondria appears to depend on the availability of CL.[2] Normally, over 95% of CL is confined to the inner mitochondrial membrane.[8] During apoptosis, CL migrates from the inner leaflet to the outer leaflet of the inner membrane and further to the outer mitochondrial membrane, setting the stage for its facilitated interaction with cyt *c*. Recent data shows that CL plays a very important role in structural organization of the electron transport chain into integrated respiratory super-complexes by "gluing together" individual respiratory complexes.[50,51] A part of the inter-membrane cyt *c* pool is embedded into respiratory chain super-complexes.[52] Our results suggest that CL-bound cyt *c* is not a component of respiratory super-complexes. Moreover, it is possible that excess CL and its interaction with cyt *c* – as it happens during apoptosis - prevents the correct assembly of respiratory complexes.

The reduction of cyt *c* in mitochondria may be accomplished not only directly via Complex III, but also by superoxide anion radicals generated as a result of univalent reduction of molecular oxygen by mitochondrial protein complexes.[3,4] We demonstrated that superoxide cannot effectively reduce cyt c/CL complexes. Thus CL/cyt *c* complexes are neither directly reduced by complex III nor indirectly by O_2^-. This suggests that CL/cyt *c* complexes are excluded from electron-transport in mitochondria and are likely present in their oxidized form, increasing the probability of the formation of peroxidase compounds I and II in the presence of oxidizing equivalents such as H_2O_2 or organic and lipid hydroperoxides.

The redox environment of mitochondria is significantly affected by the presence and reactions of ascorbate as a potent reductant localized in mitochondria.[53] However, ascorbate-

driven reduction of cyt *c* to its ferrous form would be inhibitory to the peroxidase reactions of cyt *c* realized within CL/cyt *c* complexes (see below). EPR monitoring of ascorbate radicals and cyt *c* reduction clearly demonstrated that CL/cyt *c* complexes were not readily reducible by ascorbate. This finding is in line with the other results of this report indicating that association with CL acts as a switch turning off normal electron donor-acceptor functions of cyt *c* and facilitating its peroxidase function.

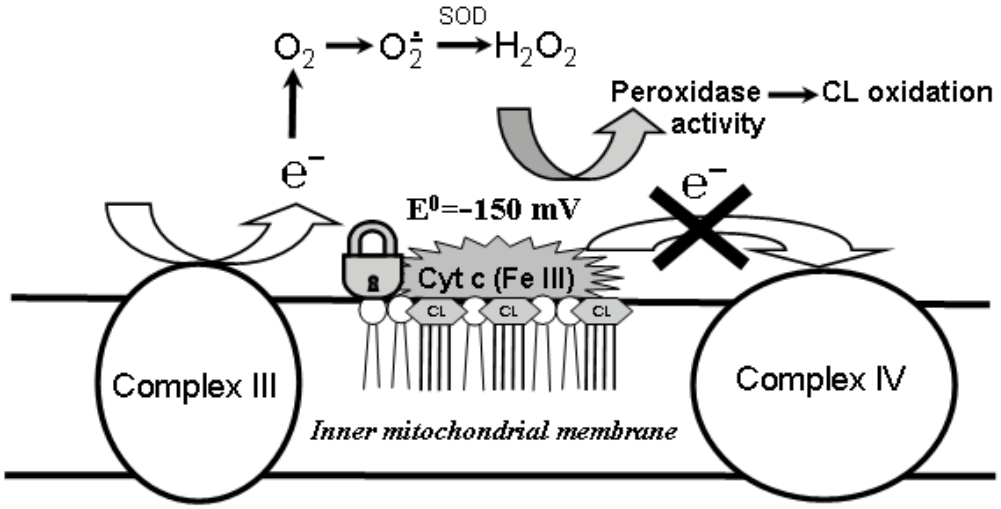

Scheme 3.1. Interactions of cyt *c* with CL resulting in a drastic negative shift of the cyt *c* redox potential: a possible mechanism of disruption of mitochondrial electron transport and increased production of ROS.

Overall, interactions of cyt *c* with CL during apoptosis represent an essential part of a well coordinated mechanism of programmed cell death (see Scheme 3.1). A marked negative shift of the cyt *c* redox potential by CL favors the accumulation of ferri-cyt *c* which is essential for effective peroxidase catalysis. Moreover, the negative redox potential of cyt *c*/CL complexes excludes them from the electron transport chain, causing disruption of electron flow and facilitating generation of superoxide radicals. Dismutation of the latter yields H_2O_2 that feeds the peroxidase function of cyt *c*/CL complexes.

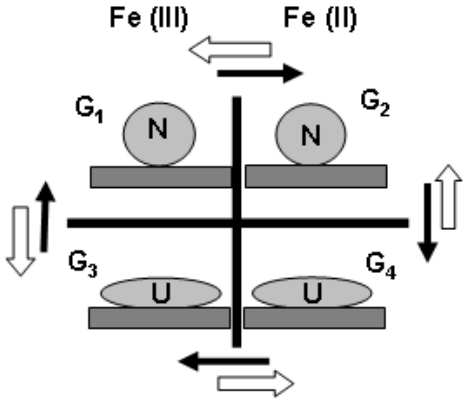

Scheme 3.2 Thermodynamic cycle of reduction and unfolding of cyt *c* in the presence of CL.

3.4.2 The Redox State of CL/cyt *c* Complexes and Their Peroxidase Function. Inhibition of cyt *c* reduction is important for its peroxidase function, particularly during apoptosis, for several reasons. Peroxidase reactions utilize oxidizing equivalents of H_2O_2 and/or organic (lipid) hydroperoxides to generate potent oxidizing oxo-ferryl intermediates from ferri-cyt *c* (Fe(III)), in which a highly oxidized state of Fe(IV) is active in producing catalytically competent protein-derived (often tyrosyl) radicals.[54,55] It is possible that interactions of ferro-cyt *c* with hydroperoxides will lead to the production of hydroxyl (alkoxyl) radicals that are known to indiscriminately attack biomolecules.[56] As a result, loss of substrate selectivity and enzymatic specificity are likely to occur. Further, the negative shift of the cyt *c* redox potential associated with CL-induced protein structural changes implies that the reduced cyt *c* is much more resistant to denaturation by anionic lipids than the oxidized cyt *c* in line with previous reports.[16,57] Indeed, consideration of a thermodynamic cycle, depicted in Scheme 3.2, for cyt *c* bound to CL membranes electrostatically (the native tertiary structure) or hydrophopically (partially denatured protein) in the two redox states shows that the free energy of the conversion of cyt *c* into a denatured form is much more positive in the reduced state than in the oxidized state:

$$\Delta G_{red}^{denat} - \Delta G_{ox}^{denat} = (G_4 - G_2) - (G_3 - G_1) = (G_4 - G_3) - (G_2 - G_1) = e(E_N^0 - E_{denat}^0) \approx 9kcal/mol$$

The denaturing of cyt *c* upon its oxidation and subsequent refolding to a native-like tertiary structure upon reduction was observed in our voltammetry experiments, resulting in a very large separation of oxidation and reduction peaks for cyt *c* interacting with CL. The peroxidase activity of cyt *c* is associated with a destabilization of the protein tertiary structure. Thus, the reduced cyt *c* is less likely to convert into a peroxidase than the oxidized cyt *c*. Factors affecting the redox state of cyt *c* should influence its peroxidase activity and may change the development of apoptosis. For example, an increased production of NO•, known to block complex IV function and increase the concentration of reduced cyt *c*[53,58] will likely inhibit the peroxidase function of CL/cyt *c* complexes. Along with direct interactions of NO• with reactive intermediates of CL/cyt *c* during peroxidase catalysis[55] this may represent an important antioxidant and anti-apoptotic mechanism. Moreover, a reducing redox-environment for mitochondria (e.g., during hypoxic or ischemic conditions) is also counter-productive for the peroxidase function whereas reoxygenation and re-oxidation of cyt *c* is likely to favor its conversion into a catalytically active peroxidase. Not surprisingly, reoxygenation, rather than hypoxia/ischemia are associated with increased apoptotic damage.[59]

Finally, while CL binds cyt *c* with a very high affinity, it is not unique as a modifier of cyt *c*'s redox behavior. Other anionic phospholipids, particularly PS, can also confer peroxidase activity on the protein although less effectively than CL.[13] Studies in this and other laboratories characterized unfolding of the protein upon its binding with CL. Further studies are necessary to detail specific mechanisms through which these conformational rearrangements, particularly in the heme-binding site, translate into changes of cyt *c* redox potential and electrochemistry.

References

(1) Mathews, C. K., van Holde, K.E., Ahem, K.G. (1999) *Biochemistry*, third ed., Addison Wesley Longman, San Francisco.

(2) Pettigrew, G. W., and Moore, G. R. (1987) *Cytochrome c - Biological aspects*, Springer-Verlaf: Berlin, Heidelberg.

(3) Pereverzev, M. O., Vygodina, T. V., Konstantinov, A. A., and Skulachev, V. P. (2003) Cytochrome c, an ideal antioxidant. *Biochem Soc Trans 31*, 1312-1315.

(4) Turrens, J. F. (2003) Mitochondrial formation of reactive oxygen species. *J Physiol 552*, 335-344.

(5) Gogvadze, V., Orrenius, S., and Zhivotovsky, B. (2006) Multiple pathways of cytochrome c release from mitochondria in apoptosis. *Biochim Biophys Acta*. *1757*, 639-647.

(6) Garrido, C., Galluzzi, L., Brunet, M., Puig, P. E., Didelot, C., and Kroemer, G. (2006) Mechanisms of cytochrome c release from mitochondria. *Cell Death Differ*. *13*, 1423-1433.

(7) Fadeel, B., and Orrenius, S. (2005) Apoptosis: a basic biological phenomenon with wide-ranging implications in human disease. *J Intern Med 258*, 479-517.

(8) Kagan, V. E., Tyurin, V. A., Jiang, J., Tyurina, Y. Y., Ritov, V. B., Amoscato, A. A., Osipov, A. N., Belikova, N. A., Kapralov, A. A., Kini, V., Vlasova, II, Zhao, Q., Zou, M., Di, P., Svistunenko, D. A., Kurnikov, I. V., and Borisenko, G. G. (2005) Cytochrome c acts as a cardiolipin oxygenase required for release of proapoptotic factors. *Nat Chem Biol 1*, 223-232.

(9) Yoshida, H., Kawane, K., Koike, M., Mori, Y., Uchiyama, Y., and Nagata, S. (2005) Phosphatidylserine-dependent engulfment by macrophages of nuclei from erythroid precursor cells. *Nature 437*, 754-758.

(10) Wang, H., Blair, D.F., Ellis, W.R.Jr., Gray, H.B. and Chan S.I. (1986) Temperature dependence of the reduction potential of CuA in carbon monoxide inhibited cytochrome c oxidase. *Biochemistry 25*, 167-171.

(11) Belikova, N. A., Vladimirov, Y. A., Osipov, A. N., Kapralov, A. A., Tyurin, V. A., Potapovich, M. V., Basova, L. V., Peterson, J., Kurnikov, I. V., and Kagan, V. E. (2006) Peroxidase activity and structural transitions of cytochrome c bound to cardiolipin-containing membranes. *Biochemistry 45*, 4998-5009.

(12) Diederix, R. E., Ubbink, M., and Canters, G. W. (2002) Peroxidase activity as a tool for studying the folding of c-type cytochromes. *Biochemistry 41*, 13067-13077.

(13) Kagan, V. E., Borisenko, G. G., Tyurina, Y. Y., Tyurin, V. A., Jiang, J., Potapovich, A. I., Kini, V., Amoscato, A. A., and Fujii, Y. (2004) Oxidative lipidomics of apoptosis: redox catalytic interactions of cytochrome c with cardiolipin and phosphatidylserine. *Free Radic Biol Med 37*, 1963-1985.

(14) Pinheiro, T. J. (1994) The interaction of horse heart cytochrome c with phospholipid bilayers. Structural and dynamic effects. *Biochimie 76*, 489-500.

(15) Nantes, I. L., Zucchi, M. R., Nascimento, O. R., and Faljoni-Alario, A. (2001) Effect of heme iron valence state on the conformation of cytochrome c and its association with membrane interfaces. A CD and EPR investigation. *J Biol Chem 276*, 153-158.

(16) Letellier, L., and Shechter, E. (1973) Correlations between structure and spectroscopic properties in membrane model system. Fluorescence and circular dichroism of the cytochrome c-cardiolipin system. *Eur J Biochem 40*, 507-512.

(17) Pinheiro, T. J., Cheng, H., Seeholzer, S. H., and Roder, H. (2000) Direct evidence for the cooperative unfolding of cytochrome c in lipid membranes from H-(2)H exchange kinetics. *J Mol Biol 303*, 617-626.

(18) Oellerich, S., Lecomte, S., Paternostre, M., Heimburg, T., and Hildebrandt, P. (2004) Peripheral and integral binding of cytochrome c to phospholipids vesicles. *J Phys Chem B 108*, 3871-3878.

(19) Brown, L. R., and Wuthrich, K. (1977) NMR and ESR studies of the interactions of cytochrome c with mixed cardiolipin-phosphatidylcholine vesicles. *Biochim Biophys Acta 468*, 389-410.

(20) Soussi, B., Bylund-Fellenius, A. C., Schersten, T., and Angstrom, J. (1990) 1H-n.m.r. evaluation of the ferricytochrome c-cardiolipin interaction. Effect of superoxide radicals. *Biochem J 265*, 227-232.

(21) Domanov, Y. A., Molotkovsky, J. G., and Gorbenko, G. P. (2005) Coverage-dependent changes of cytochrome c transverse location in phospholipid membranes revealed by FRET. *Biochim Biophys Acta 1716*, 49-58.

(22) Salamon, Z., and Tollin, G. (1997) Interaction of horse heart cytochrome c with lipid bilayer membranes: effects on redox potentials. *J Bioenerg Biomembr 29*, 211-221.

(23) Jing, W. G., Liu, C.W., Tang, J.L., Wu, Z.Y., Dong, S.J., Wang, E.K. (2003) Electrochemical and spectroscopic study on the interaction of cytochrome c with anionic lipid vesicles *Chinese Journal of Chemistry 21*, 544-549.

(24) Wackerbarth, H., and Hildebrandt, P. (2003) Redox and conformational equilibria and dynamics of cytochrome c at high electric fields. *Chemphyschem 4*, 714-24.

(25) Petrovic, J., Clark, R. A., Yue, H., Waldeck, D. H., and Bowden, E. F. (2005) Impact of surface immobilization and solution ionic strength on the formal potential of immobilized cytochrome C. *Langmuir 21*, 6308-6316.

(26) Zahn, J.A., Arciero, D.M., Hooper, A.B., Coats, J.R. and DiSpirito, A.A. (1997) Cytochrome *c* peroxidase from Methylococcus capsulatus Bath. Arch Microbiol. 168, 362-72.

(27) Weiler, M.H., Gundersen, C.B., and Jenden, D.J. (1981) Choline uptake and acetylcholine synthesis in synaptosomes: investigations using two different labeled variants of choline. *J Neurochem. 36*, 1802-1812.

(28) Gudz, T. I., Tserng, K. Y., and Hoppel, C. L. (1997) Direct inhibition of mitochondrial respiratory chain complex III by cell-permeable ceramide. *J Biol Chem 272*, 24154-24158.

(29) Storrie, B., and Madden, E. A. (1990) Isolation of subcellular organelles. *Methods Enzymol 182*, 203-225.

(30) Thierbach, G., and Reichenbach, H. (1981) Myxothiazol, a new inhibitor of the cytochrome b-c1 segment of th respiratory chain. *Biochim Biophys Acta 638*, 282-289.

(31) Birch-Machin, M. A., Briggs, H. L., Saborido, A. A., Bindoff, L. A., and Turnbull, D. M. (1994) An evaluation of the measurement of the activities of complexes I-IV in the respiratory chain of human skeletal muscle mitochondria. *Biochem Med Metab Biol 51*, 35-42.

(32) Ritov, V. B., Menshikova, E. V., and Kelley, D. E. (2004) High-performance liquid chromatography-based methods of enzymatic analysis: electron transport chain activity in mitochondria from human skeletal muscle. *Anal Biochem 333*, 27-38.

(33) McCord, J. M., and Fridovich, I. (1968) The reduction of cytochrome c by milk xanthine oxidase. *J Biol Chem 243*, 5753-5760.

(34) Heineman, W. R., Meckstroth, M.L., Norris, B.J., and Su, C.-Ho. (1979) Optically Transparent thin layer electrode techniques for the study of biologigal redox systems. *J. Electroanal.Chem. 104*, 577-585.

(35) Yue, H., Waldeck, D. H., Petrovic, J., and Clark, R. A. (2006) The effect of ionic strength on the electron-transfer rate of surface immobilized cytochrome C. *J Phys Chem B Condens Matter Mater Surf Interfaces Biophys 110*, 5062-72.

(36) Napper, A. M., Liu, H. and Waldeck, D. H. (2001) The Nature of Electronic Coupling between Ferrocene and Gold through Alkanethiolate Monolayers on Electrodes: The Importance of Chain Composition, Interchain Coupling, and Quantum Interference *J. Phys. Chem. B. 105*, 7699-7707.

(37) Feng, Z. Q., Imabayashi, Sh., Kakiuchi, T. and Niki, K. (1997) Long-range electron-transfer reaction rates to cytochrome c across long- and short-chain alkanethiol self-assembled monolayers: Electroreflectance studies. *Journal of the Chemical Society, Faraday Transactions 93*, 1367-1370.

(38) Handbook of Chemistry and Physics, 75th Ed. 1994/95, editor D. Lide, Cleveland, OH: CRC Press, p. 965.

(39) Sagun, K. C., Carcamo, J.M. and Golde, D.W. (2005) Vitamin C enters mitochondria via facilitative glucose transporter 1 (Glut1) and confers mitochondrial protection against oxidative injury. *The FASEB Journal 19*, 1657-1667.

(40) Myer, Y. P., and Kumar, S. (1984) Ascorbate reduction of horse heart cytochrome c. A zero-energy reduction reaction. *J Biol Chem 259*, 8144-50.

(41) Petlicki, J., Theo G.M. van de Ven. (1998) The equilibrium between the oxidation of hydrogen peroxide by oxygen and the dismutation of peroxyl or superoxide radicals in aqueous solutions in contact with oxygen. *J.Chem.Soc., Faraday Trans. 94*, 2763-2767.

(42) Butler, J., Koppenol, W. H., and Margoliash, E. (1982) Kinetics and mechanism of the reduction of ferricytochrome c by the superoxide anion. *J Biol Chem 257*, 10747-50.

(43) Birch-Machin, M. A., and Turnbull, D. M. (2001) Assaying mitochondrial respiratory complex activity in mitochondria isolated from human cells and tissues. *Methods Cell Biol 65*, 97-117.

(44) Taylor, R. W., Birch-Machin, M. A., Bartlett, K., Lowerson, S. A., and Turnbull, D. M. (1994) The control of mitochondrial oxidations by complex III in rat muscle and liver mitochondria. Implications for our understanding of mitochondrial cytopathies in man. *J Biol Chem 269*, 3523-3528.

(45) Kalyanaraman, B., Perez-Reyes, E., and Mason, R.P. (1979) The reduction of nitroso-spin traps in chemical and biological systems. A cautionary note. *Tetrahedron Letters 50*, 4809-4812.

(46) Kennedy, Ch.H., Pryor, W.A., Winston, G. W., and Church, D. F. (1986) Hydroperoxide-induced radical production in liver mitochondria. *Biochemical and Biophysical research communications 141*, 1123-1129.

(47) Chen, Y.R., and Mason, R.P. (2002) Mechanism in the reaction of cytochrome c oxidase with organic hydroperoxides: an ESR spin-trapping investigation. *Biochem J 365*, 461-469.

(48) Petrosillo, G., Ruggiero, F. M., and Pistolese, M. (2004) Paradies G. Ca2+-induced reactive oxygen species production promotes cytochrome c release from rat liver

mitochondria via mitochondrial permeability transition (MPT)-dependent and MPT-independent mechanisms: role of cardiolipin. *J. Biol. Chem. 279*, 53103-53108.

(49) Crouser, E. D., Gadd, M. E., Julian, M. W., Huff, J. E., Broekemeier, K. M., Robbins, K. A., and Pfeiffer, D. R. (2003) Quantitation of cytochrome c release from rat liver mitochondria. *Analytical Biochemistry 317*, 67-75.

(50) Zhang, M., Mileykovskaya, E., and Dowhan, W. (2005) Cardiolipin is essential for organization of complexes III and IV into a supercomplex in intact yeast mitochondria. *J Biol Chem 280*, 29403-29408.

(51) Zhang, M., Mileykovskaya, E., and Dowhan, W. (2002) Gluing the respiratory chain together. Cardiolipin is required for supercomplex formation in the inner mitochondrial membrane. *J Biol Chem 277*, 43553-43556.

(52) Bianchi, C., Genova, M. L., Parenti Castelli, G., and Lenaz, G. (2004) The mitochondrial respiratory chain is partially organized in a supercomplex assembly: kinetic evidence using flux control analysis. *J Biol Chem 279*, 36562-36569.

(53) Heck, D. E., Kagan, V. E., Shvedova, A. A., and Laskin, J. D. (2005) An epigrammatic (abridged) recounting of the myriad tales of astonishing deeds and dire consequences pertaining to nitric oxide and reactive oxygen species in mitochondria with an ancillary missive concerning the origins of apoptosis. *Toxicology 208*, 259-271.

(54) Chen, Y. R., Chen, C. L., Chen, W., Zweier, J. L., Augusto, O., Radi, R., and Mason, R. P. (2004) Formation of protein tyrosine ortho-semiquinone radical and nitrotyrosine from cytochrome c-derived tyrosyl radical. *J Biol Chem 279*, 18054-18062.

(55) Vlasova, II, Tyurin, V. A., Kapralov, A. A., Kurnikov, I. V., Osipov, A. N., Potapovich, M. V., Stoyanovsky, D. A., and Kagan, V. E. (2006) Nitric oxide inhibits peroxidase

activity of cytochrome c.cardiolipin complex and blocks cardiolipin oxidation. *J Biol Chem 281*, 14554-145562.

(56) Huie, R. E., and Neta, P. (1999) *Chemistry of Reactive Oxygen Species In Reactive Oxygen Species in Biological Systems: An Interdisciplinary Approach*, Kluwer Academic/Plenum Publishers, New York.

(57) Bhuyan AK, Udgaonkar JB. Folding of horse cytochrome *c* in the reduced state. *J Mol Biol. 312,* 1135-1160.

(58) Brunori, M., Giuffre, A., Forte, E., Mastronicola, D., Barone, M. C., and Sarti, P. (2004) Control of cytochrome c oxidase activity by nitric oxide. *Biochim Biophys Acta 1655*, 365-371.

(59) Du, G., Mouithys-Mickalad, A., and Sluse, F. E. (1998) Generation of superoxide anion by mitochondria and impairment of their functions during anoxia and reoxygenation in vitro. *Free Radic Biol Med 25*, 1066-1074.

4.0 THE ELECTRONIC STRUCTURE OF CDSE NANOPARTICLES ADSORBED ON AU ELECTRODES BY AN ORGANIC LINKER: FERMI LEVEL PINNING OF THE HOMO

This work has been published as T. Z. Markus, M. Wu, L. Wang, D. H. Waldeck, D. Oron, R. Naaman, *J Phys Chem C*; **2009**; 113; 14200-14206. The voltammetry study of the nanoparticles and band edge analysis were performed by the thesis author.

Abstract

Assemblies of CdSe nanoparticles (NPs) on a dithiol coated Au electrode were created and their electronic energetics were quantified. This report describes the energy level alignment of the filled and unfilled electronic states of CdSe nanoparticles with respect to the Au Fermi level. Using cyclic voltammetry it was possible to measure the energy of the filled states of the CdSe NPs with respect to the Au substrate relative to a $Ag/AgNO_3$ electrode, and by using photoemission spectroscopy it was possible to independently measure both the filled state energies (via single photon photoemission) and those of the unfilled states (via two photon photoemission) with respect to the vacuum level. Comparison of these two different measures shows good agreement with the IUPAC accepted value of the absolute electrode potential. In contrast to the common model of energy level alignment, the experimental findings show that the CdSe filled states become 'pinned' to the Fermi level of the Au electrode, even for moderately small NP sizes.

4.1 Introduction

Semiconductor nanoparticles (NPs) are envisioned as materials for light harvesting and photovoltaic applications. This desire has sparked intensive research into the nature of light induced charge transfer between NPs and between NPs and various substrates.[1,2,3,4,5,6] One may envision that a device based on NPs will contain NPs of various band gaps, so as to cover the entire solar spectrum, and that one could engineer the device so that the NPs self-assemble into a robust superstructure. To design such structures efficiently, one would like to know the position of the electronic states, both occupied and unoccupied, so that efficient charge separation can be made possible. This work describes a set of studies that measures this energetics for CdSe NPs on gold electrodes.

In this study, the NPs are adsorbed onto a solid substrate that serves as an electrode. For any photoelectronic application, the energy of the HOMO (valence band) and LUMO (conduction band) of the NPs relative to the Fermi level of the electrode is of major importance. When NPs are adsorbed on electrodes the electrochemical potential of the solid and the NP layer come into equilibrium. Hence it is expected that the relative positions of the bulk electrode's Fermi level and the HOMO and LUMO of the NPs will adjust, and the adjustment will depend on the properties of the interface and the properties of the NPs, *e.g.*, their size. In a simple model, the effective mass approximation, it is assumed that the HOMO-LUMO gap varies with size, so that the shift is inversely proportional to the effective mass of the relevant charge carrier, i.e., the hole and electron.[7,8,9,10]

This work addresses the questions, 'How do the HOMO and LUMO vary as a result of attaching the NPs to a metal electrode and how does its variation depend on the size of the NPs?'. We use two independent methods for determining the energy alignment between a gold

substrate and the HOMO and LUMO of CdSe NPs as a function of size; the NPs are linked to the gold through a self-assembled monolayer of dithiols. In the first method we combine single photon photoelectron spectroscopy with two photon photoelectron spectroscopy[11] to provide a direct measure of the position of the electronic states, both HOMO and LUMO, with respect to the vacuum level. In the second method, we apply cyclic voltammetry to measure the position of the HOMO and LUMO with respect to a Ag/AgCl reference potential. In both cases we compare the energy gaps with the peak fluorescence emission wavelength of the nanoparticles and find good agreement. Comparison of these results (photoemission, voltammetry, and fluorescence) provides a consistent view of the electronic state energies and how they evolve with the nanoparticle size.

A few studies have investigated the position of the electronic states of NPs relative to the Fermi level of the substrate on which they are adsorbed. These studies include tunneling spectroscopy,[12,13] cyclic voltammetry,[14,15,16,17] and photoemission.[18] The voltammetry studies relate most directly to the work reported here. Previous work has assigned a strong oxidation peak between 1 and 1.5 V versus $Ag/AgNO_3$ to the injection of a hole into the HOMO of the CdSe nanoparticle. In most studies a corresponding reduction wave, albeit weaker, is also observed. The voltammetry studies reported here provide reasonable agreement with earlier studies. A new feature of this study is the comparison of the voltammetry measurements of the band position with electron photoemission measurements of the band positions under UHV conditions. This comparison provides an important test of the voltammetry assignment and an assessment of the accuracy in assigning an absolute electrochemical potential for the NPs.

4.2 Experimental Section

The CdSe nanoparticles were synthesized, purified, and characterized using standard protocols and details of these procedures are provided in the Supplementary Material.

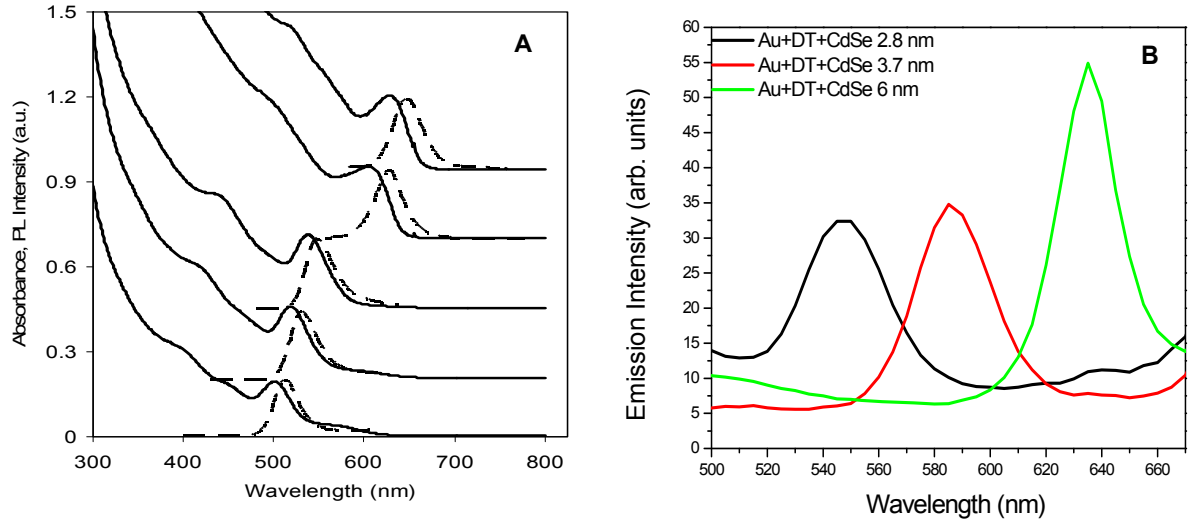

Figure 4.1 Panel A shows normalized absorbance spectra (solid lines) and photoluminescence spectra (dashed lines, λ_{ex} = 400 nm) of five different sizes of CdSe nanocrystal samples in toluene; the curves for different NPs are shifted vertically for clarity. Panel B shows the photoluminescence signal (λ_{ex} = 350 nm) obtained for three sizes of CdSe NPs when adsorbed to the gold substrate through the organic linker.

4.2.1 Absorption and Fluorescence Emission Spectra

The absorption and emission spectra for five of the NPs in solution are presented in Figure 4.1A, and the emission from three of the NPs monolayer assemblies (NPs attached to Au electrodes via a dithiol linker) are shown in Figure 4.1B. The UV-vis absorption spectra in panel A were measured at room temperature with an Agilent 8453 spectrometer. Photoluminescence (PL) spectra in panel A were measured at room temperature with a Horiba J-Y Fluoromax 3 Fluorescence Spectrophotometer, using an excitation wavelength of 400 nm. The photoluminescence (PL) spectra in panel B were collected in a Fluorolog-3 Spectrofluorometer (Horiba Jobin Yvon, France) at room temperature using an excitation wavelength of 350nm. The sample was placed at an angle of 30º to the incident light and the emitted PL was collected

(Front Face PL measurement) through a monochromator. In general, only a small shift of about 2 nm was observed in the spectra of the adsorbed NPs, as compared to those taken in solution.

The position of the first absorption peak was used to define the NP size, by using the empirical formula

$$d = (1.6122 \cdot 10^{-9})\lambda^4 - (2.6575 \cdot 10^{-6})\lambda^3 + (1.6242 \cdot 10^{-3})\lambda^2 - (0.4277)\lambda + 41.57 \quad \textbf{(1)}$$

where d and λ are in nm.[19]

4.2.2 Voltammetry Studies

Gold ball electrodes. A Au wire (0.5 mm diameter, 99.99% purity) was cleaned by reflux in concentrated nitric acid (68-70%) at 130 °C overnight and then was washed with deionized water. The tip of the gold wire was heated to form a ball of ~0.06-0.15 cm^2 surface area. The gold ball was reheated in the flame until glowing and then quenched in deionized water. This annealing process was performed more than 15 times to make a smooth gold ball. The exposed Au wire was sealed in a glass capillary tube, and the Au ball tip was annealed and cooled in a high-purity stream of Ar gas.

Immobilization of CdSe nanoparticles (NPs). Chemically modified electrodes were prepared by placing the gold ball electrodes into the 5 mM 1,10-decanedithiol SAM solution for overnight (> 12 hours). After that, the electrodes were taken out from the solution, rinsed with absolute ethanol, and dried under a nitrogen stream. The CdSe NP layers were prepared by immersing the Au-dithiol sample into a CdSe NP dispersion for 6 hours, rinsed with toluene, dried and immediately used in voltammetry studies.

Electrochemical Measurements. A computer-controlled CHI 618B electrochemical workstation (CH Instruments, Austin, TX) and a Faraday cage was used for all electrochemical

measurements. The three-electrode cell was composed of a platinum counter electrode, a Ag|0.01 M $AgNO_3$, 0.1 M $TBAPF_6$ as reference electrode, and the SAM-coated Au as a working electrode. The voltammetry measurements were performed in 100 mM solution of $TBAPF_6$ in acetonitrile to inhibit corrosion. The $Ag/AgNO_3$ has a potential at 0.54 V versus NHE. [20]

4.2.3 Photoemission studies

Sample preparation and characterization:

The NP/electrode assemblies consisted of CdSe NPs linked to a gold film by a monolayer of 1,9-nonanedithiol (DT). First a DT monolayer on Au was prepared according to the procedures described in reference [21] by immersing a clean gold substrate[22] in a methanol solution of 1 mM DT. Adsorption was carried out overnight in N_2-filled vials that were placed in a desiccator. After adsorption, the samples were rinsed with ethanol and then dried with N_2. In order to attach the CdSe NPs, the DT-SAM coated gold substrates were immersed in 0.5-10 μM solutions of CdSe NPs in anhydrous toluene (99.8%, Aldrich). Four different CdSe NPs were used, large with an average diameter of 6 nm (maximum emission at 635 nm), medium-large with average diameter of 3.7 nm (maximum emission at 590 nm), medium-small with average diameter of 2.8 nm (maximum emission at 550 nm), and small with an average diameter of 2.3 nm (maximum emission at 500 nm). The samples were than rinsed and sonicated in toluene to remove excess NPs that were not covalently attached. The samples were dried under an N_2 gas flow.

SEM Characterization: High-resolution scanning electron microscope (HRSEM) inlense-detector imaging was carried out with a LEO-Supra 55 VP HRSEM. Figure 4.2 shows a clean Au substrate (A) and a monolayer of CdSe NPs 6 nm in diameter on the Au-DT substrate (B). A uniform high coverage was observed for all three larger sizes of NPs.

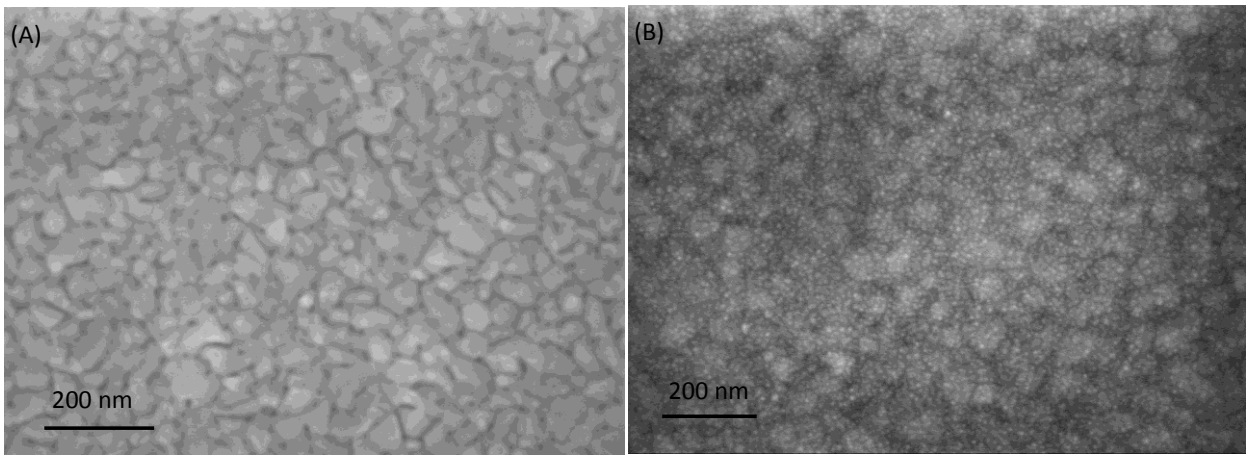

Figure 4.2 SEM Image: (A) Au reference (B) Au covered with a DT monolayer and CdSe NPs. Contrast the small bright spots in panel B with the reference image in panel A.

Photoemission Measurement:

The photoemission experiments were based on ejection of photoelectrons from the NP-coated-Au assemblies. The experimental setup is similar to that described in ref [23]. The experiments were performed in an ultrahigh vacuum chamber ($<10^{-8}$ Torr). The photoelectrons are emitted from the sample to the vacuum, where their energy is measured by a time-of-flight spectrometer. Because of the short lifetime of the electrons that are captured by the NPs and monolayer and because of the low laser intensity and repetition rate, the monolayer and the NPs are not charged by electrons between laser pulses. This was verified by observing a stable electron energy spectrum which does not vary with time.

In the Low Energy Photoelectron Transmission (LEPET) method, electrons are ejected by photons with energy higher than the work function of the sample. The photoelectrons are emitted from states below the Fermi level to above the vacuum level, from which they escape the sample and are transmitted to the detector. These studies provide information about the density of states below the Fermi level, hence the position of the HOMO.

In two-photon photoelectron (TPPE) spectroscopy, photons with energy lower than the work function of the sample are used. The “pump” photons interact with electrons that reside in

states below the Fermi level and excite them to states above the Fermi level but below the vacuum level of the sample. If the laser pulses used are not very intense and are relatively long, the electrons excited by these first photons can relax either back to states below the Fermi level or to originally unoccupied states in the monolayer, an 'intermediate' state. The second laser pulse, the "probe", also has photons with energies below the work function of the sample; nevertheless they are able to photoeject electrons from occupied 'intermediate' states to an energy above the vacuum level, from which they can escape the sample and be detected. The measured kinetic energy of these photoelectrons provides information on the binding energy of the electron in the intermediate state, the LUMO of the NPs.

In this experiment we used two photons from the same laser pulse to induce the two-photon-photoemission of electrons. Because of the relatively long laser pulse (laser pulse length of ~10 nsec) and the low intensities, no significant contribution to the signal from a two-photon coherent process was observed. In the coherent process the kinetic energy of electrons would be $2h\nu - (\Phi + E_b)$ because of energy conservation; Φ is the substrate workfunction and E_b is the electron binding energy. Thus when varying the energy of the photons the change in the kinetic energy difference between photoelectrons should increase as twice the photon energy. In contrast, the observed photoelectron energy increases as one times. This observation indicates that the observed photoelectrons from the TPPE process arise from long lived intermediate states; the first photon excites an electron that relaxes to some long-lived intermediate state, and only then can the electron be photoejected from this intermediate state by the second photon. In order for these intermediate states to be long-lived, they must be localized on the NPs. Hence, the kinetic energy of the electrons reflects their binding energy in the monolayer so that

$$E_b = \Phi - (h\nu - E_k) \quad \textbf{(2)}$$

In all of these studies, the sample was biased by -1 V versus the detector.

4.3 Results

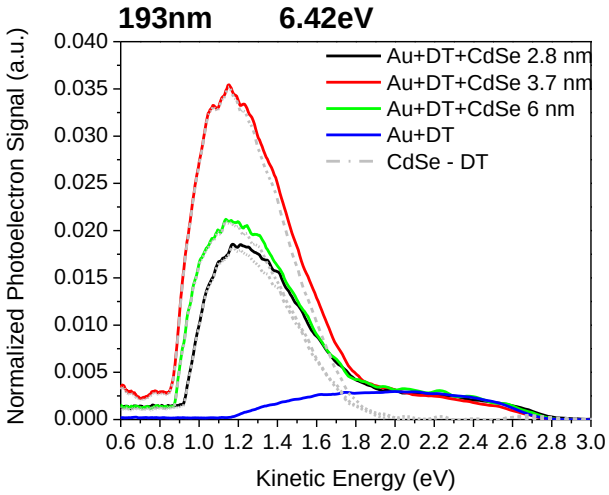

Figure 4.3 LEPET spectra are shown for the four NPs monolayers studied. The dashed gray curves show difference spectra that are obtained by subtracting the spectrum of the Au-DT; note the similar peak for the NP's in this case.

4.3.1 Photoemission

Figure 4.3 shows photoelectron energy distributions for photoelectrons that are ejected by 6.42 eV photons impinging on NP/gold assemblies (LEPET spectra). The high energy cutoff in the spectra results from electrons near the Fermi level that are the most easily ejected to above the vacuum level. Their kinetic energy is taken to be $h\nu - \Phi$, where Φ is the substrate work function. The work function is calculated from the total width of the signal which is ~1.8 eV for Au-DT and ~2.1 eV for the Au-DT-NP; so that Φ = ~4.6 eV for Au-DT and ~4.3eV for the monolayers containing NPs (depending on the coverage). The photoemission spectrum taken for a Au substrate that is covered only by the organic monolayer (DT) is weak, broad, and peaks at a kinetic energy of about 2 eV (Figure 4.3). The spectra for the monolayers containing NPs are much more intense and they can be qualitatively described as having two characteristic peaks: one with a maximum kinetic energy of ~1.15 eV and a second with a maximum kinetic energy of

~2 eV. While the peak at 2 eV is also observed for the Au-DT sample, the peak at 1.15 eV is a unique feature of the monolayers containing NPs. In addition, if one subtracts the spectrum obtained for the Au-DT sample from that obtained for the Au-DT-NP assemblies, then the resulting difference peak rises similarly for all three assemblies of the larger NPs. These difference spectra are shown in Figure 4.3 by the dashed gray curves. Although the intensity of the subtracted spectra varies with the NP size, the difference spectra shown here occur at the same energy. Because of the likely variation of the NP absorption cross section with size and the variability in the surface coverage of NPs, no effort was made to interpret the variation in signal intensity between samples. Because the LEPET spectra reflect the energy dependence of the density of states below the Fermi level, these data show that all three sizes of NPs have the HOMO located at nearly the same energy of 1.25 ± 0.05 eV below the Fermi level. In the case of the smallest NPs with an average diameter of 2.3 nm, the LEPET shows no variations as compared to the LEPET of Au-DT (Data not shown). Hence, no direct evidence for its position can be obtained. It is important to appreciate that for the same samples the fluorescence spectra indicate the existence of a monolayer of 2.3 nm diameter NPs.

Figure 4.4 presents the TPPE spectra for three sizes of NPs, presented either as a function of the binding energy (top) or kinetic energy (bottom) of the electrons. The spectra were taken at three different wavelengths. As a control experiment, photoelectron spectra of a Au-DT sample (no NPs) were collected at the same laser intensities used to obtain the spectra in Figure 4.4. In these control experiments, no significant photoelectron current was observed, indicating that the photoelectron signals shown in Figure 4.4 originate from the NPs. In the top row, the spectra for a given laser wavelength are shown for all three sizes. The peak at high binding energy for the 285 nm wavelength laser pulse (see panel A) results from a contribution by a single photon

process**.** The sharp cutoff at the high energy edge reflects the density of states in the NPs. In addition, the LUMO seems to be broadened but not symmetrically, perhaps because of a higher density of states in the gold at lower energies. The clear shift in the peak positions for the different NP's spectra, indicates that the state, from which electrons are ejected by the second photon, changes with the NPs size; its energy shifts relative to the Fermi level, indicating a shift in the LUMO position with the size of the NPs. Panels D through F show the spectra for each of the NP sizes at the three wavelengths used. These data clearly demonstrate that the high kinetic energy edge of the spectrum shifts as ($\Delta h\nu$) rather than as $2x(\Delta h\nu)$. This variation indicates that the TPPE process is not a coherent one; namely after absorption of the first photon the electron relaxes to an intermediate state and then absorbs the second photon. Based on Figure 4 we can conclude that the LUMO varies with the NP's size. The shifts observed correspond to an energy of ~0.15 eV between the NPs, which is the optical energy gap difference between the different NPs. By assigning the peak to the LUMO state we get the values of 0.95 eV, 0.8 eV, and 0.65 eV above the Fermi level for the medium-small, medium-large, and large NPs respectively.

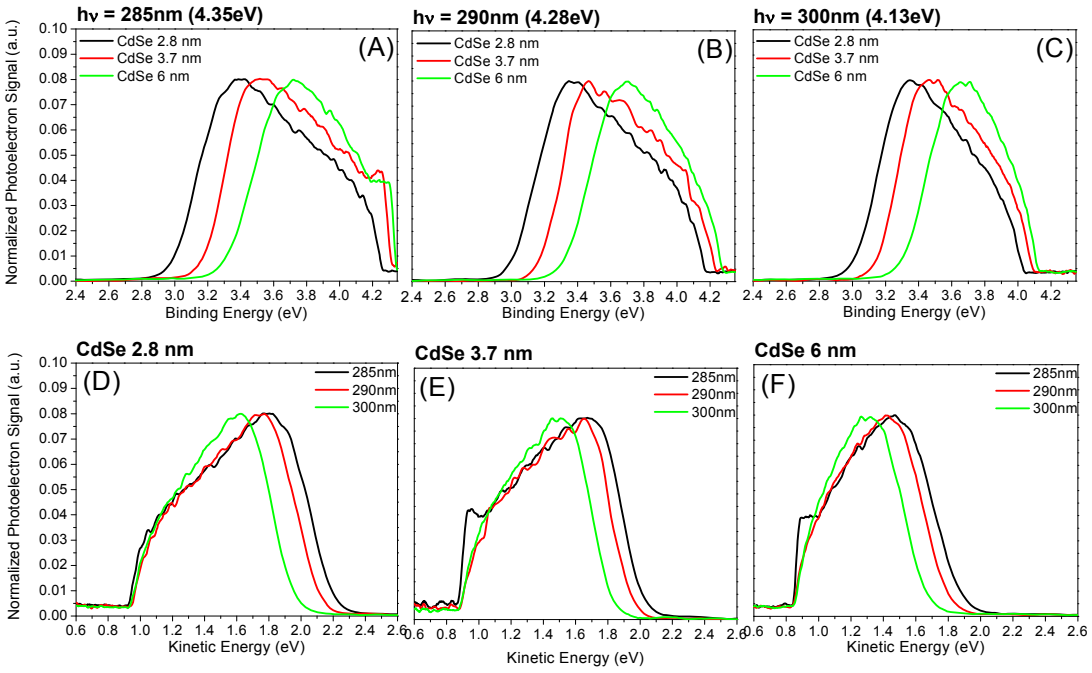

Figure 4.4 TPPE spectra for the systems containing the three different NPs and represented by the electrons binding energy relative to the Fermi level (A-C). The TPPE spectra for each of the NPs size obtained with different laser wavelength (D-F).

Figure 4.5 presents the inferred density of states above and below the Fermi level for the systems containing the three sizes of nanoparticles and for the gold covered with DT only. The peaks from the TPPE and the LEPET were normalized for this analysis. While, as mentioned above, the HOMO seems to have the same energy for all sizes, the LUMO position varies. The energy gap between the HOMO and LUMO positions found from the photoemission data are in excellent agreement with the band gap energy obtained from the fluorescence emission data. Figure 4.5 clearly shows that the HOMO position of the larger NPs is pinned to the same energy level while the LUMO of the system shifts in a way that is expected from the fluorescence data and the changing size of the NPs.

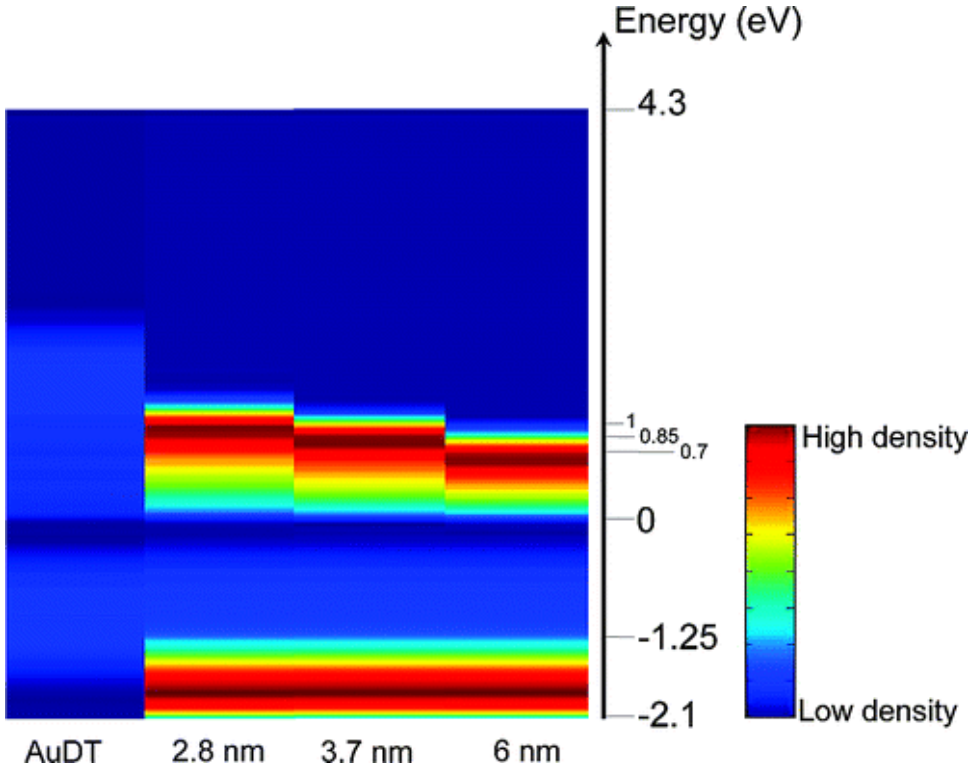

Figure 4.5 Inferred density of states for the four monolayers studied. The results are in good agreement with the optical energy gap observed for the three sizes of NPs (2.8, 3.7 and 6 nm) when positioning the HOMO at the deviation from the Au-DT spectra (1.25eV below the Fermi).

4.3.2 Voltammetry

Figure 4.6 shows cyclic voltammograms for three differently sized CdSe NPs adsorbed on a dithiol SAM on a gold electrode in acetonitrile solution. The voltammograms in Figure 4.6A show strong oxidation waves in the range of 1.22 V to 1.44 V versus NHE that depend on the different particle sizes. The oxidation and corresponding reduction peaks do not appear to change significantly with the potential scan rate. These voltammograms are in good agreement with those reported by others; e.g., see Ref. 16 The weak peak near 0.7 V is not assigned, however such a peak could arise from filled interband (i.e., between the HOMO and LUMO) trap states in the particle. The position of this peak is similar to that reported by Inamdar et al.[15] In contrast to Inamdar, the fluorescence spectra (see Figure 4.1) do not reveal the presence of such trap states; however the peak observed in the voltammograms is much weaker than that reported by Inamdar; these differences may reflect a difference in the number density of such defect states between the two studies. Following these earlier results, the peak of the oxidation wave is assigned to the oxidation potential of the NP. Eventually, with subsequent potential scans the oxidation peaks disappear, suggesting that the oxidation/corrosion products may form[24] and the process is not totally reversible. Assuming that the particle charging energy can be neglected, the oxidation potential corresponds to the HOMO energy. Using the IUPAC value for the absolute electrode potential, 4.44 V, these voltammograms indicate energies of 5.66 V to 5.88 V on the vacuum scale. These values are shifted by about 100 mV from those observed in the photoemission experiments.

The LUMO energies of the CdSe NPs could be determined from the reduction waves and were found to lie between -0.89 V and -1.25 V versus NHE, depending on the particle size. Figure 4.6B shows some example voltammograms. In this case the assignment of the peak was

less clear. In part, the smaller signal levels reflect the irreversibility observed in the oxidation peaks. Nevertheless, an excellent agreement between the values assigned in this manner and those calculated by adding the bandgap energy of the NP to the observed HOMO energy was found.

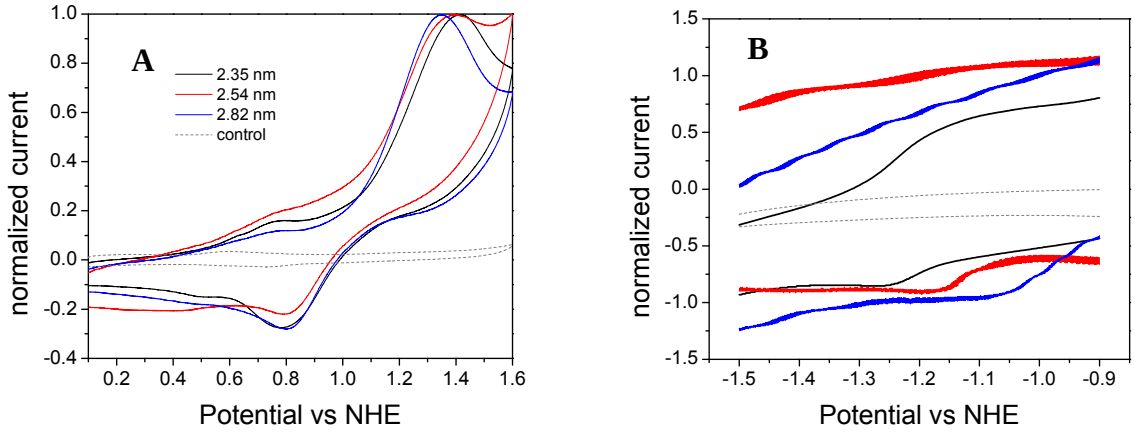

Figure 4.6 Oxidation (A) and reduction (B) voltammograms for different sizes of CdSe NPs immobilized onto a C10 dithiol SAM in acetonitrile solution (the black trace is 2.35 nm NPs, the red trace is 2.54 nm NPs, the blue trace is 2.82 nm NPs and the grey dashed trace is dithiol SAM with no NPs). The scan rate is 100 mV/s. The traces shown in panel B are an expanded region of a broader scan voltammogram.

4.3.3 NP Energetics

Figure 4.7 shows a plot of the HOMO and LUMO energy positions for the differently sized NPs; both those obtained from the voltammetry and those obtained from the photoemission experiments. The NP size assignments are made based upon the position of the first absorption peaks that were observed in solution for the NPs.[19] The HOMO positions in this graph include those taken from the oxidation potential of the NPs and those obtained from the single photon photoemission studies. In both cases, the data for the HOMO energy display a relatively flat size dependence for NPs larger than 2.8 nm. The voltammetry experiments reveal a negative energy shift with decreasing size for sizes below 2.8 nm. The positions obtained from the electrochemistry measurements are shifted systematically by about 100 mV more negative than

those found from the photoemission measurement. This difference may be the result of the way the energy of the HOMO was defined in the photoemission spectra, but could also result from uncertainties in the accepted value of the absolute electrode potential.[25] The valence band edge position for bulk CdSe is reported to lie near -6.0 eV on the vacuum scale,[26] however this would place it below the HOMO of the NPs. The diagram in Figure 4.7 assumes that the valence band of the bulk CdSe is pinned to a value of 1.25 eV below the Au Fermi level, as is the HOMO of the NPs. The figure also shows the change in LUMO energy with NP size. The LUMO energy appears to shift systematically over the entire range of NP sizes and is converging on the value of -3.85 eV corresponding to the valence band edge of bulk CdSe.

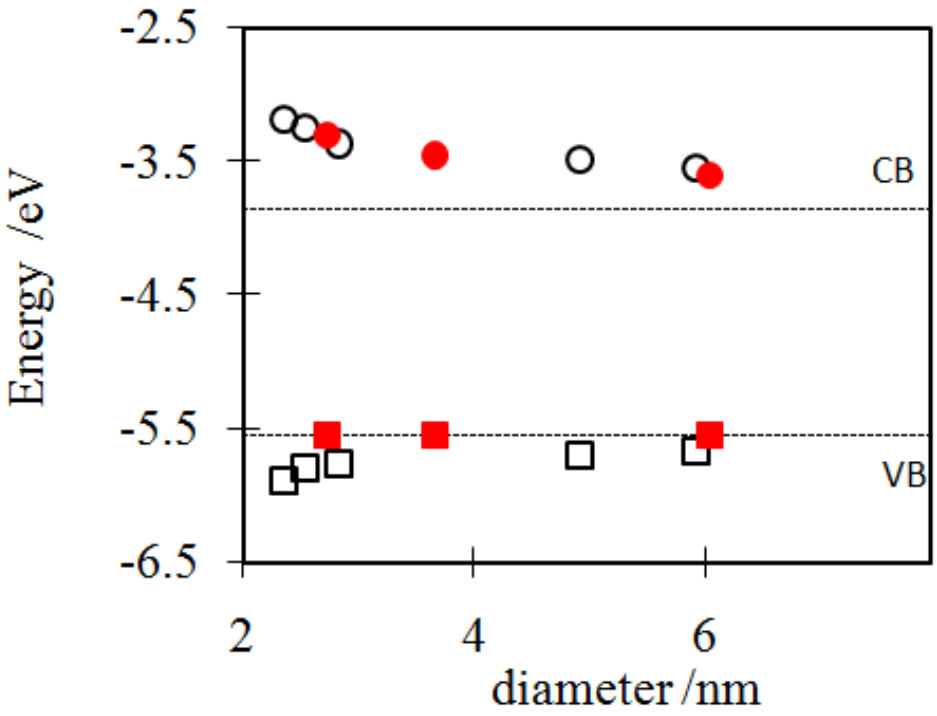

Figure 4.7 The graph plots the HOMO energies (open squares from electrochemistry and filled squares from photoemission measurements) and LUMO energies (open circles from electrochemistry and filled circles from photoemission measurements) of the different CdSe NPs as a function of their diameter. The dashed lines mark the bulk CdSe band positions, assuming that its valence band is pinned at 1.25 eV below the Fermi level of Au.

4.4 Discussion

Figure 4.8 plots the shift in the LUMO energy position, as obtained from the experiments reported here (open circles are voltammetry and filled circles are photoemission). In addition, this plot includes a comparison to literature data (x's) for the change in the NP energy gap with size. This comparison was performed by pinning the HOMO energy at the value measured in this work and adding to it the literature value of the energy gap in order to predict a LUMO energy position. This comparison demonstrates the agreement/consistency between the energy level assignments reported here and the bandgap energy, which is well known.

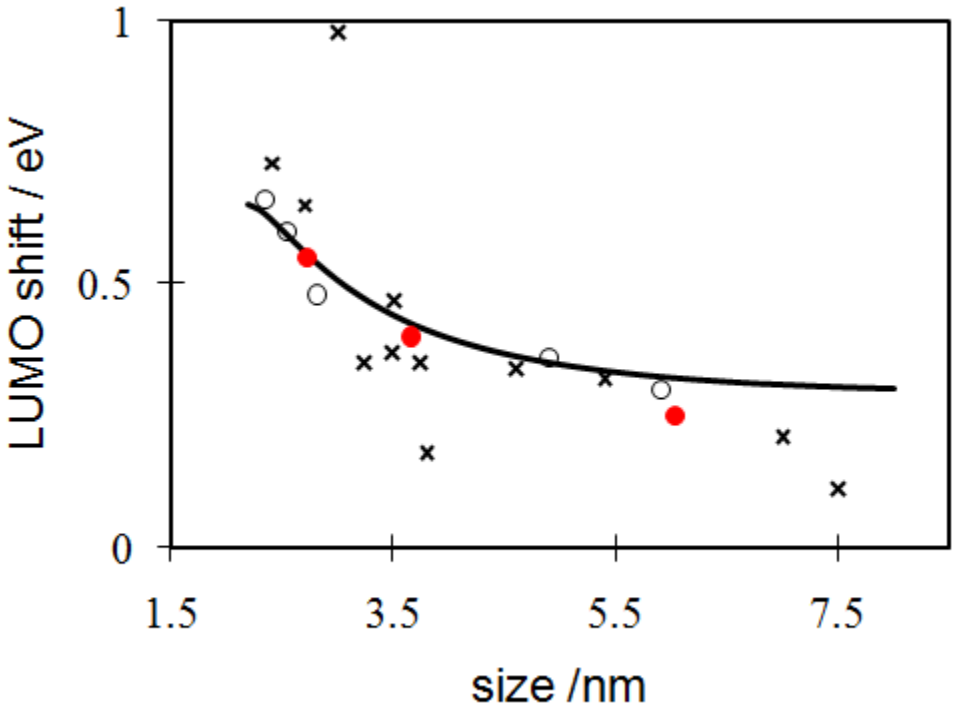

Figure 4.8 The shift of the lowest excited electronic state energy (LUMO) from the bulk value is plotted as a function of particle diameter. The open circles are data obtained from electrochemistry data; the filled circles are data obtained from the photoemission; and the x's are values reported in the literature.[14,16,17] The solid curve represents the theoretical predication from Brus.[7]

Brus has proposed a model for the shift in the energy gap of NPs with particle diameter. [7] In this model, the bandgap change ΔE is expressed as a perturbation to the bulk energy gap; Brus finds that

$$\Delta E = \frac{h^2}{2d^2}\left[\frac{1}{m_e} + \frac{1}{m_h}\right] - \frac{3.6\, e^2}{\varepsilon_2 d} + \frac{2e^2}{d}\overline{\sum_{n=1}^{\infty} \alpha_n \left(\frac{2S}{d}\right)^{2n}} \qquad \textbf{(3)}$$

where m_e and m_h are the effective electron and hole masses ($m_e = 0.13m_0$, $m_h = 0.44m_0$ for bulk CdSe, m_0 as electron rest mass), ε_2 is the dielectric coefficient of the particle (4.86 for CdSe), and *S* is the position where a real positive charge exists in the sphere with the radius *d/2*. The first term is the quantum energy of localization, the second term is the coulomb attraction, and the third term is the solvation energy loss. The curve through the data set corresponds to the prediction of this model for the LUMO energy position, obtained by assuming that the HOMO energy is pinned. Because the HOMO energy is pinned, the LUMO energy should shift in the same manner as the energy gap. The solid curve is a best fit of the experimental LUMO energies by equation 1, with the parameters given above.

The most interesting and surprising finding of the present studies is the fact that the HOMO of the NPs, when attached to the surface, is pinned and its position does not vary with the particle size. A similar effect has been observed for pentacene adsorbed on conducting polymers,[27] In that case it has been rationalized by charge transfer that causes the pinning of the HOMO. This explanation cannot be valid in our case, since contact potential difference studies show that the charge transfer between the NPs and the substrate does not depend on the size of the NPs. Hence, the HOMO pinning must be explained by interactions between the HOMO of the NPs and the states of the substrate coated with the DT. Indeed, it has been found and verified that the thiol coated gold has a high density of states at energies of about 1.2 eV to 1.6 eV below the Fermi level.[28] These interfacial states (thiol:Au states) may act to couple strongly with the

NP. Hence, the coupling of the HOMO of the NPs to the high density of states of the gold is through these states that, at least partially, are located on the DT. As a result one expects that the effective mass of the hole in the NPs will increase. Apparently, the LUMO couples more weakly to the substrate and therefore is more localized on the NPs. Hence, the effective mass of the electron is small and when level adjustment occurs, the LUMO's energy varies more than expected based on the effective masses of the hole and the electron in the unbound nanoparticle. This weak coupling of the LUMO with the substrate also explains the relatively efficient photoemission observed from the adsorbed NPs.

4.5 Acknowledgements

This work was partially supported by the US-DOE (Grant # ER46430), by the Israel Ministry of Science, and by the Grand Center for Sensors and Security at the Weizmann Institute. The electron microscopy studies were conducted at the Irving and Cherna Moskowitz Center for Nano and Bio-Nano Imaging at the Weizmann Institute of Science.

References

(1) Zhang J. Z. *J. Phys. Chem. B* **2000**, *104*, 7239**.**

(2) Guldi, D. M.; Zilbermann, I.; Anderson, G.; Kotov, N. A.; Tagmatarchis, N.; Prato, M. *J. Mat. Chem.* **2005,** *15***,** 114.

(3) S. Kang, M.; Yasuda, H.; Miyasaka, H.; Hayashi, M.; Kawasaki, T.; Umeyama, Y.; Matano, K.; Yoshida, S.; Isoda, H. I. *Chem. Sus. Chem* **2008,** *1*, 254.

(4) Robel, I .; Subramanian, V.; Kuno, M .; Kamat, P. V. *J. Am. Chem.Soc.* **2006,** *128*, 2385.

(5) Kongkanand, A.; Tvrdy, K.; Takechi, K.; Kuno, M.; Kamat, P. V. *J. Am. Chem. Soc.* **2008**, *130*, 4007.

(6) Jiang, X.; Schaller, R. D.; Lee, S. B.; Pietryga, J. M.; Klimov, V. I .; Zakhidov, A. A. *J. Mat. Res.* **2007**, *22*, 2204.

(7) L. E. Brus, *J. Chem. Phys.* **1983**, *79*, 5566.

(8) H. Weller *et al.*, *Chem. Phys. Lett*. **1986**, *124*, 557.

(9) Y. Kayanuma, *Phys. Rev. B*, **1988**, *38*, 9797.

(10) Y. Kayanuma and H. Momiji, *Phys. Rev. B*, **1990**, *41*, 10261; D. B. Tran Thoai, Y. Z. Hu, and S. W. Koch, *Phys. Rev.***1990**, *B, 42*, 11261; Y. Nosaka, *J. Phys. Chem.* **1991**, *95*, 5054; J. L. Marı´n, R. Riera, and S. A. Cruz, *J. Phys.: Condens. Matter* **1998**, *10*, 1349; S. V. Nair, S. Sinha, and K. C. Rustagi, *Phys. Rev. B*, **1987**, *35*, 4098; J. M. Ferreyra and C. R. Proetto, *Phys. Rev. B*, 1999, *60*, 10672; S. Horiguchi, *Physica B* **1996**, *227*, 336; G. W. Bryant, *Phys. Rev. B* ,**1995**, *52*, R16997; K. K. Nanda, F. E. Kruis, H. Fissan, *Nano Lett.* **2001**, *1*, 605.

(11) T. Z. Markus, S. S. Daube, R. Naaman, A. M. Fleming, J. G. Muller, C. J. Burrows, *J. Am. Chem. Soc.* **2009**, *131*, 89–95.

(12) P. Liljeroth, L. Jdira, K. Overgaag, B. Grandidier, S. Speller, D. Vanmaekelbergh, *Phys. Chem. Chem. Phys.* **2006**, *8*, 3845–3850.

(13) D. Steiner, D. Dorfs, U. Banin, F. D. Sala, L. Manna, O. Millo, *Nano Lett.*, **2008**, *8* (9), 2954-2958.

(14) Wang, C.; Shim, M.; Guyot-Sionnest, P.; Franck, J. *Science* **2001**, *291*, 2390.

(15) S. N. Inamdar, P. P. Ingole, . S. K. Haram, *ChemPhysChem*. **2008**, *9*, 2574; E. Kucur, W. Bucking, R. Giernoth, T. Nann, *J. Phys. Chem. B*, **2005**, *109*, 20355; E. Kucur, W. Bucking, S. Arenz, R. Giernoth, T. Nann, *ChemPhysChem*. **2006**, *7*, 77–81.

(16) E. Kucur, J. Riegler, G. A. Urban, and T. Nann *J. Chem. Phys.* **2003**, *119*, 2333-2337.

(17) I. Robel, M. Kuno, and P. V. Kamat, *J. Am. Chem. Soc*. **2007**, *129*, 4136-4137.

(18) Meulenberg, R. W., Lee, J. R.I., Wolcott, A., Zhang, J. Z., Terminello, L. J., and van Buuren T. *ACS Nano* **2009**, *3*, 325-330.

(19) W. W. Yu, L. Qu, W. Guo, and X. Peng *Chem Mater* **2003**, *15*, 2854-2860..

(20) *Electroanalytical Methods: Guide to Experiments and Applications*, Edited by Fritz Scholz. Springer. Verlag, Heidelberg , **2002**, p298

(21) T. Aqua, H. Cohen, A. Vilan, R. Naaman *J. Phys. Chem. C*, 2007, *111* (44), pp 16313–16318

(22) Ron, H.; Matlis, S.; Rubinstein, I. *Langmuir* **1998**, *14*, 1116-1121.

(23) Ray, S. G.; Daube, S. S.; Cohen, H.; Naaman, R. *Isr. J. Chem* **2007**, *47*, 149.

(24) S. K. Poznyak, N. P. Osipovich, A. Shavel, D. V. Talapin, M. Gao, A. Eychmueller, and N. Gaponik *J. Phys. Chem. B* **2005**, *109*, 1094-1100.

(25) a) Gomer, R.; Tryson. G.. *J. Chem. Phys*. **1977**, *66*, 4413; b) Trasatti, S. *Pure and Appl. Chem*. **1986**, *58*, 955.

(26) J. Jasieniak, J. Pacifico, R. Signorini, A. Chiasera, M. Ferrari, A. Martucci, and P. Mulvaney *Adv. Func. Mat.* **2007**, *17*, 1654-1662

(27) N. Koch, A. Elschner, J.P. Rabe, R.L. Johnson, *Adv. Mat*. **2005**, *17*,330; N. Koch, A. Vollmer, *App. Phys. Lett*. **2006**, *89*, 162107.

(28) A. L. Graham,. R. Colorado, Jr., V. H. Wysocki, T. R. Lee, P. A. Lee, N. R. Armstrong, *J. Phys. Chem. B* **2003**, *107*, 11690-11699.

Supplement material

The electronic structure of CdSe nanoparticles adsorbed on Au electrodes by an organic linker: Fermi level pinning of the HOMO

T. Z. Markus, M. Wu, L. Wang, D. H. Waldeck, D. Oron, R, Naaman

Chemicals

All aqueous solutions were prepared with 18.3 MΩ cm^{-1} deionized water (Nanopure, Barnstead, Dubuque, IA). 1,10-decanedithiol ($HSC_{10}H_{20}SH$) was purchased from Alfa Aesar, and tetrabutylammoniumhexafluorophosphate ($TBAPF_6$) was purchased from Sigma. Electrodes used in all experiments were gold ball electrodes made from gold wire (0.5 mm diameter, 99.99%, Alfa Aesar). Selenium powder (99.999%), hexadecylamine (HDA, 99%), trioctylphosphine (TOP, 97%), trioctylphosphine oxide (TOPO, 90%), oleylamine (97%), oleic acid (90%), 1-octadecene (ODE, 90%), CdO (99.999%) were purchased from Aldrich and used as received. All reagents and solvents were obtained from commercial sources and used as received.

CdSe NP synthesis and purification

Spherical CdSe nanoparticles were prepared in a manner similar to a previously published procedure.[1] All synthetic routes were carried out under argon gas using Schlenk techniques. For a typical synthesis of 2-4 nm CdSe nanoparticles, 0.0514 g of CdO, 0.2919 g of HDA and 3.8768 g of TOPO were loaded into a 25 mL three-neck round-bottom flask. The mixture was heated to 300 ℃ under Ar flow, and CdO was dissolved in HDA and TOPO. A

selenium stock solution (0.0787 g of selenium powder dissolved in 4 ml of TOP) was injected quickly. After injection, nanocrystals were allowed to grow at 280 ℃ until they reached the desired size. For 4-6 nm CdSe nanoparticles, typically, 5.0 mL of oleylamine and 0.15 mL of Se stock solution (2.1 M in TOP) were loaded in a 50-mL flask, and the mixture was heated to 90 ℃ and degassed under a vacuum for 30 min. The reaction vessel was then filled with argon, and the temperature was increased to 300 ℃ under stirring. A 1.0 mL volume of Cd stock solution (0.3 M in 1:1 v/v oleic acid and ODE) was injected quickly into the reaction flask. The temperature was then set at 280 ℃ for the subsequent growth and annealing of nanocrystals.

For the photoemission measurements, particles were synthesized in a non-coordinating solvent. 0.013 g of CdO and 0.3ml of oleic acid were added to 5ml octadecene. 0.008g of Se in 2ml TOP was injected at 280 ℃, and particles were grown at 250 ℃. For the largest particles, Cadmium oleate in octadecene and Se in TOP were further injected until the desired size was reached.

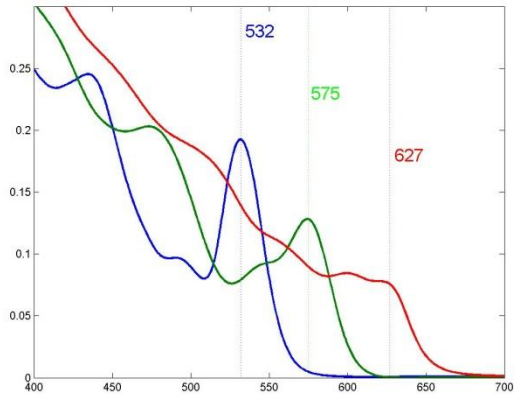

Figure 4.1S: The absorption spectra of the nanoparticles taken in solution.

1. a) Peng, Z. A. ; Peng, X. *J. Am. Chem. Soc.* **2001,** *123*, 183-184; b) Zhong, X; Feng, Y.; Zhang ,Y. *J. Phys. Chem. C* **2007,** *111*, 526-53; c) Talapin, D.V.; Rogach, A.L.; Kornowski, A.; Haase, M., Weller, H. *Nano Letters*, **2001,** *1* (4), 207-211

5.0 ENERGY ARCHITECTURE DEPENDENCE ON THE ORDERING OF CDSE/CDTE NANOPARTICLES

Abstract

CdSe and CdTe nanoparticles have been successfully immobilized onto Au electrodes through a dithiol self-assembled monolayer. The electronic states of the nanoparticles were determined by cyclic voltammetry. The HOMO positions of the nanoparticles are pinned when they are immobilized onto the surface. On the other hand, the LUMO positions of the nanoparticles shift with the particle sizes. Bilayer structures were produced by assembling different sizes of CdSe and CdTe particles. The energy architecture of the NP bilayers was varied to explore its impact on photocurrent generation. To maximize the energy gradient for different layers, CdSe of larger size and CdTe of smaller size were chosen. When the smaller sized CdTe is in the outer layer, a high photocurrent is observed and can be explained as the facilitated electron transfer by the inner CdSe layer. When the larger sized CdSe is in the outer layer, a very low photocurrent is observed. In this case, the outer layer of CdSe acts to block the hole scavenging. Also a bilayer system of differently sized CdSe NPs was examined. The photocurrent is much larger for the "small on large" system.

5.1 Introduction

Increasing demand for environmentally clean alternative energy sources is driving a resurgence of interest in solar energy harvesting.[1] While silicon-based photovoltaic technology is well evolved, it remains costly and a need for higher efficiency and lower cost photoconversion technologies exists. The recent development of nanomaterials as new building blocks to construct light energy harvesting assemblies offers promise for meeting this challenge.[2] One prominent example is the creation of organic and inorganic hybrid structures with semiconductor nanoparticles (NPs) that exhibit improved selectivity and efficiency toward light energy conversion.[3,4] Because of the quantum size effect, semiconductor NPs of different size and/or composition can be used to create light harvesting assemblies that capture a large fraction of the incident solar spectrum.

Beyond this straightforward advantage, NPs offer the promise to more efficiently utilize the incident solar energy by a better exploitation of hot electrons or the generation of multiple charge carriers with a single photon. The maximum thermodynamic efficiency for the conversion of solar irradiation into electrical free energy was calculated by Shockley and Queisser[5] to be about 32% for Si based solar cells. A major factor limiting the conversion efficiency is that the absorbed photon energy above the semiconductor band gap is lost through thermalization processes. One approach to overcoming this efficiency limitation is to create a bandgap cascade (tandem solar cell),[6] a strategy that is very amenable to semiconductor NPs as well as bulk materials. Another approach, which is yet to be realized, is for the energetic/hot carriers to produce a second, or more, electron-hole pair through impact ionization.[7] It has been proposed and reported that photogenerated carriers in semiconductor NPs can have their relaxation dynamics dramatically altered; specifically the hot carrier cooling rates may be dramatically

reduced, and the rate of the impact ionization can become competitive with the rate of carrier cooling.[8] Thus, semiconductor NPs promise to play an important role for improving photoconversion efficiency, and a better understanding of their properties, particularly their relationship to structure and composition, will be critical in learning to manipulate and optimize their function.

Control and knowledge of the band gap and band edge position are crucial for photovoltaic and electroluminescent applications of NPs. To this end, many experimental studies and model calculations concerning the size quantization effect have been published over the past two decades.[9-12] The majority of these calculations start from the assumption that exciton with a size smaller than the Bohr radius can be described with a particle-in-a-box model, where the particle is represented by the exciton and the box by the nanoparticle. This model and experimental data show that the band gap of semiconductor NPs increases with decreasing particle size. While significant effort has been made to make these models more realistic for the bandgap position, relatively little effort has been made to predict and experimentally test the energies of the band edges.

The electrochemical determination of the band edge and defect states in CdSe NPs has been review by Kucur et al.[13] The ionization potentials, electron affinities, and the quantum confinement in CdSe NPs were determined by means of cyclic voltammetry, and they were found to be consistent with theoretical expectations and spectroscopic data. More recently our group[14] compared electrochemical voltammetry and ultraviolet photoelectron spectra for different sizes of CdSe NPs immobilized onto a C10 dithiol SAM and found a good correspondence between the energy level positions measured in these two very different ways (see the supporting material which summarizes the relevant findings). These previous studies

show that the difference between E_{ox} for the NP valence band and E_{red} for the NP conduction band compares well to the spectroscopically observed exciton absorption peak E_{abs}. Most interesting and surprising was our finding that the valence band (HOMO) of the CdSe NPs was Fermi-level pinned to the Au substrate on which it was immobilized; i.e., its position did not vary significantly for particle sizes larger than 2.8 nm. Subsequently, Carlson et al.[15] reported a similar effect for CdSe NPs adsorbed on a single crystal ZnO surface via 3-mercaptopropionic acid linkers; they report that the valence band maximum (VBM) of the CdSe NPs is 0.1 eV above the VBM of ZnO. These observations support the hypothesis that the the HOMO pinning results from the interaction between the HOMO of the NPs and the states of the substrate coated with the dithiol.[14]

CdTe is another II-VI semiconductor material that has a bulk band gap of 1.5 eV[16] at 300 K and a strong optical absorption coefficient. Water soluble thiol-capped CdTe NPs can be successfully incorporated into ultrathin polymer films using the layer-by-layer assembly method, and CdTe NPs display a distinct size dependent photostability.[17,18] The electrochemical behavior of CdTe in solution has been thoroughly investigated by Poznyak et al.[19] and others.[20,21] Electrochemical studies of thiol-capped CdTe NPs in aqueous solution have demonstrated several distinct oxidation and reduction peaks in the voltammograms, with the peak positions being dependent on the size of the NPs.[22] Bard et al.[21] showed that the electrochemical band gaps (~2.1 eV) between the first anodic and cathodic peaks was close to the optical E_g value (2 eV) for TOPO-capped CdTe NPs. Upon changing the particles size the reduction and oxidation peaks in the voltammograms were shifted in the direction predicted by theory.[11,23] Thus, CdTe NPs in solution do not display Fermi-level pinning with respect to the electrode. One goal of the current

study is to compare the energetics of CdTe NPs that are immobilized on a Au electrode to those that are freely diffusing in solution.

To explore the features of NPs, we have assembled monolayer and bilayer assemblies of CdTe and CdSe nanoparticles (NPs) on Au electrodes using bifunctional surface modifiers of the type HS-R-HS. Absolute band gap positions were obtained from electrochemical measurements, and the photophysical and photoinduced electron transfer processes that follow the excitation of the NP assemblies are probed by photoelectrochemical measurements. For bilayer assemblies of two different NPs on a Au substrate, the photocurrent response of the bilayer assemblies depends on the ordering of differently sized nanoparticles with respect to the surface.

5.2 Experimental Section

The CdSe and CdTe nanoparticles were synthesized, purified, and characterized using standard protocols and details of these procedures are provided in the supporting information.

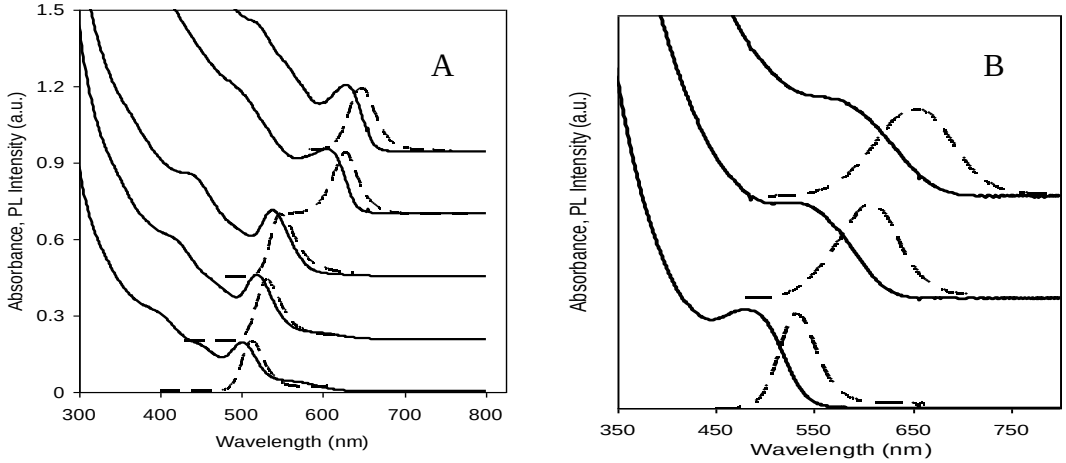

Figure 5.1 Normalized absorbance spectra (solid lines) and photoluminescence spectra (dashed lines, λ_{ex} = 400 nm) of five different sizes of CdSe nanoparticle samples in toluene (A) and three different sizes of CdTe nanoparticles samples in aqueous buffer (B); the curves for different NPs are shifted vertically for clarity.

5.2.1 Absorption and fluorescence emission spectra. The absorption and emission spectra for five sizes of the CdSe NPs in toluene solution are presented in Figure 5.1A, and the absorption

and emission spectra for three sizes of the CdTe NPs in aqueous solution are presented in Figure 5.1B. The UV-visible absorption spectra were measured at room temperature with an Agilent 8453 spectrometer. Photoluminescence (PL) spectra were measured at room temperature with a Horiba J-Y Fluoromax 3 Fluorescence Spectrophotometer, using an excitation wavelength of 400 nm. All electrochemical and photochemical measurements were performed using spherical CdSe nanoparticles of five sizes (diameters): 2.35 nm, 2.54 nm, 2.82 nm, 4.91 nm and 5.91 nm, and CdTe nanoparticles of three sizes (diameters): 1.87 nm, 3.21 nm, and 3.51 nm. Particle sizes were estimated by TEM images (figure 5.2) and the empirical fitting functions of the peaks in UV/visible absorption.[24]

CdSe: $D = (1.6122\times10^{-9})\lambda^4 - (2.6575\times10^{-6})\lambda^3 + (1.6242\times10^{-3})\lambda^2 - (0.4277)\lambda + (41.57)$

CdTe: $D = (9.8127\times10^{-7})\lambda^3 - (1.7147\times10^{-3})\lambda^2 + (1.0064)\lambda - (194.84)$

In the above equations, D (nm) is the diameter of a given nanoparticle sample, and λ (nm) is the wavelength of the first excitonic absorption peak of the corresponding sample.

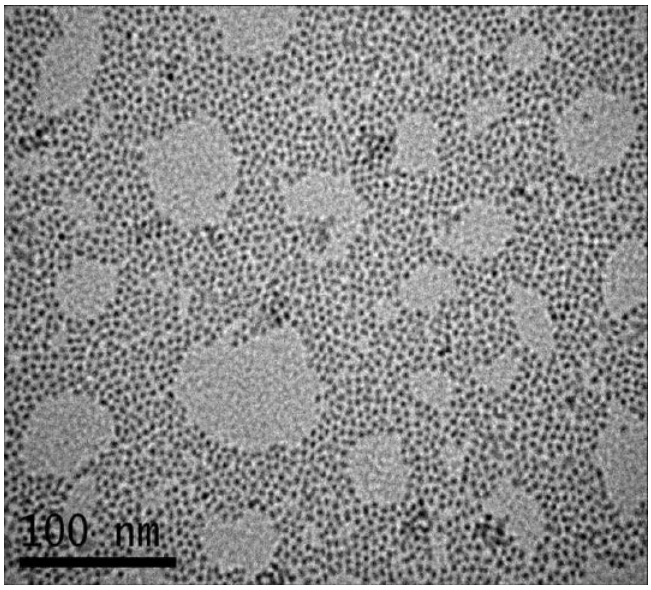

Figure 5.2 TEM image of CdSe nanoparticle with average diameter: 3.1 nm

5.2.2 Voltammetry Studies. Both Au ball electrodes and Au film electrodes were used in this study. *Gold ball electrodes* were made according to the procedure described previously.[25,26] A Au wire (0.5 mm diameter, 99.99% purity) was cleaned by reflux in concentrated nitric acid (68-70%) at 130 °C overnight and then was washed with deionized water. The tip of the gold wire was heated to form a ball of ~0.06-0.15 cm^2 surface area. The gold ball was reheated in the flame until glowing and then quenched in deionized water. This annealing process was performed more than 15 times to make a smooth gold ball. The exposed Au wire was sealed in a glass capillary tube, and the Au ball tip was annealed and cooled in a high-purity stream of Ar gas. *Gold film electrodes (thickness: 150 nm)*: Au films were prepared by an e-beam evaporator under vacuum (3×10^{-5} Pa) onto glass plates (micro slide glass) with 5-nm-thick Cr as an adhesion layer. The deposition rate was controlled to be 0.1 nm/s. The thickness was estimated by QCM.

Immobilization of nanoparticles (NPs): Chemically modified electrodes were prepared by placing the gold ball electrodes into the 5 mM 1,10-decanedithiol SAM solution for overnight (> 12 hours). After that, the electrodes were taken out from the solution, rinsed with absolute ethanol, and dried under a nitrogen stream. The NP layers were prepared by immersing the Au-dithiol (Au-dt) coated electrodes into an NP dispersion for 6 hours (Au-dt-NP), rinsed with DI water, dried and immediately used in voltammetry studies. Additional layers of the dithiol and NPs were formed on the Au-dt-NP sample by consecutive immersion into a dithiol solution to form Au-dt-NP-dt and subsequently a solution of NP' (Au-dt-NP-dt-NP'). NP and NP' may or may not be the same nanoparticle type.

Electrochemical Measurements: A computer-controlled CHI 618B electrochemical workstation (CH Instruments, Austin, TX) and a Faraday cage were used for all electrochemical measurements. The three-electrode cell, composed of a platinum counter electrode, a Ag|0.01 M

$AgNO_3$, 0.1 M $TBAPF_6$ in acetonitrile as reference electrode, and SAM-coated Au as a working electrode, was used for CdSe NPs. For CdSe NPs, the voltammetry measurements were performed in a 100 mM solution of $TBAPF_6$ in acetonitrile to inhibit corrosion. The $Ag|AgNO_3$ has a potential at 0.54 V versus NHE. The three-electrode cell, composed of a platinum counter electrode, a Ag|AgCl reference electrode, and the SAM-coated Au as a working electrode, was used for CdTe NPs. All the mixed layers of particles were test in aqueous solution. The Ag|AgCl has a potential at 0.22 V versus NHE.

Photocurrent measurements: The working electrode was illuminated with a 150-W Oriel Xenon lamp through a quartz window. A Photon Technology International high-intensity grating monochromator was introduced into the light path to select the excitation wavelength for the measurement of action spectra. All experiments were carried out under ambient conditions.

5.3 Results and Discussion

5.3.1 Absolute band gap positions determination by cyclic voltammetry. A typical cyclic voltammogram is shown in Figure 5.3A for a Au ball electrode immersed in a CdTe NPs acetonitrile solution. The solid curve shows the voltammogram for the CdTe NPs in solution and the dashed curve shows the voltammogram for the buffer solution background. Over a scan window from -1.0 to 1.0 V the current is negligible for the Au electrode. For a more positive scan window, the oxidation of the Au electrode starts from 1.2 V and causes a cathodic current peak to occur at 0.8 V during the reverse potential scan. Upon introducing CdTe NPs into the buffer solution multiple peaks can be observed when the potential is swept from the negative to positive position. As shown in Figure 5.3B the peaks remained stable with repetitive scans. At least three distinct anodic peaks can be recorded in the potential regions from 0.85 to 0.95 V (peak A1), from 0.05 to 0.2 V (peak A2) and from -0.5 to -0.2 V (peak A3). The peak positions

depend on the CdTe NPs size and the potential scan rate. Similarly, at least three distinct cathodic peaks appear during the reverse potential scan in the potential regions from -1.2 to -1.1 V (peak C1), from -0.85 to -0.65 V (peak C2) and from 0.2 to 0.4 V (peak C3). Both the oxidation and reduction of the Au electrode are strongly suppressed due to the existence of the CdTe NPs. The large peak to peak separation reflects the irreversibility of the oxidation and reduction of NPs.

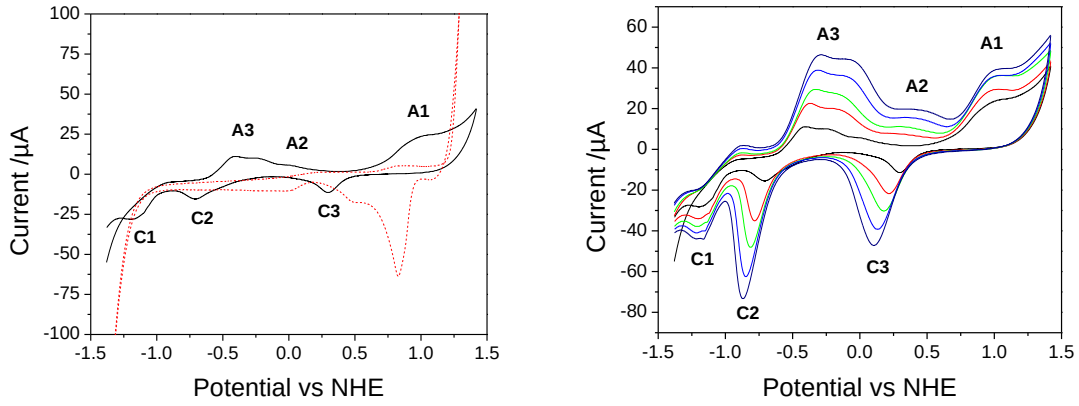

Figure 5.3 (A) Cyclic voltammogram of Au electrode in aqueous solution containing MPA-capped CdTe NPs (solid line), and in the aqueous solution background (dashed red line). Scan rate: 100 mV/s. (B) Scan rate dependence of the CV response for the Au electrode in CdTe NPs solution: υ= 100, 200, 300, 400 and 500 mV/s.

The peak to peak separation between A1 and C1 is 2.1 V when extrapolated to 0 V/s potential scan rate, a value comparable to the band gap of 2.14 eV estimated from the first absorption peak of the absorption spectrum. Thus, the potential of the peak A1 and C1 are assigned to the energy positions of the HOMO and LUMO, respectively. For metallic nanoparticles, electron transfer to the NP charges is quantized, so-called quantized double layer charging (QDL). The lack of QDL and the irreversibility for the oxidation and reduction of the CdTe NPs suggests a multielectron transfer process where the electrons are consumed by fast coupled chemical reactions that lead to eventual decomposition of the particles.[27] Essentially, the

electron is scavenged after injection into the particle, and the CdTe NPs can accept additional electrons at the same potential, giving rise to higher peak currents. The appearance of additional cathodic and anodic peaks in the middle of the potential window (A2, A3, C2 and C3) supports this hypothesis. The decomposition upon charge transfer to the particle can be viewed as the trapping of electron and holes on the particle surface.

To investigate the possibility of adsorption, cyclic voltammograms at different scan rates were obtained as shown in figure 5.3B. The linear fit of peak currents C2 and C3 (see supporting materials figure S5.4) indicate that CdTe NPs adsorb onto the gold surface. The peak position shifted with increasing potential scan rate, indicating kinetic effects. This result agrees with the phenomenon observed by Poznyak et al,[19] who noticed that the voltammogram of the preadsorbed CdTe NPs is nearly identical to that of the solution case.

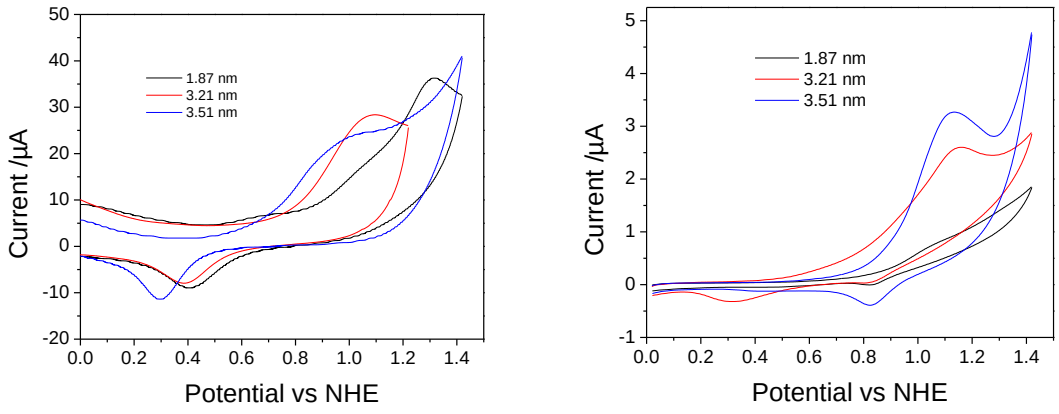

Figure 5.4 Voltammograms of the Au electrode in aqueous solution containing different sizes of MPA-capped CdTe nanoparticles (A) and Au electrodes with preadsorbed different sizes of CdTe nanoparticles onto a decanedithiol SAM in 0.1 M phosphate aqueous pH = 3 buffer solution (B). Scan rate: 100 mV/s.

Figure 5.4A shows three cyclic voltammograms at an Au electrode for three different CdTe NP buffer solutions, in which the CdTe NP size is changed. The peak A1 moves in the positive direction with decreasing NP size when NPs are in the solution. Since the peak A1

correlates the HOMO energy level, the HOMO energy shifts with the size of the NP when it is immersed in solution. While the trend of peak C1 changes less strongly with NP size, it does shift and the band gap between the HOMO and LUMO increases as the particle size decreases.[28]

Table I. Summary of band positions of CdTe nanoparticles in solution

	NP1	NP2	NP3
λ_{max} (nm)	492	553	580
D (nm)	1.87	3.21	3.51
$E_{ox\ in\ soln}$(V)	1.33	1.10	0.96
$E_{red\ in\ soln}$(V)	-1.09	-1.1	-1.14
E_g (eV)	2.42	2.20	2.10
E_{abs} (eV)	2.53	2.25	2.14

Table I summarizes the peak potentials for the oxidation and reduction of adsorbed nanoparticles. The values were determined from the cyclic voltammograms in figure 5.4A. The difference $E_g = E_{ox} - E_{red}$ should be similar to the effective band gap of the semiconductor particles, and may be compared to the observed band gap E_{abs} by absorption spectra. The band gap obtained from the electrochemistry measurements are slightly smaller than those found from the absorption spectrum measurement. This difference may be the result of the way the energy of the band gap was defined in the absorption spectra, but could also result from how the energy of the HOMO and LUMO positions are defined in the electrochemistry measurements.

Figure 5.4B shows the cyclic voltammograms of different sized CdTe immobilized onto a C10 dithiol SAM that is immersed in a 100 mM pH 3 phosphate buffer solution. Previous studies show that the stability of the SAM can be improved by low pH,[29] and control experiments

indicate that the dithiol SAM is stable up to 1.5 V under pH=3 conditions. In contrast to the solutions of NPs (figure 5.4A), the voltammograms in Figure 5.4B show strong oxidation waves in the range of 1.08 V to 1.14 V versus NHE that depend only weakly on the different particle sizes; nor do the oxidation and corresponding reduction peaks appear to change significantly with the potential scan rate. Following the findings discussed above, these peaks are assigned to the oxidation potential for the NP HOMO level. Using the IUPAC value for the absolute electrode potential, 4.44 V, these voltammograms indicate energies of 5.52 V to 5.58 V on the vacuum scale. Similar to what was found for CdSe NPs,[14] the HOMO of the CdTe NPs, when attached to the surface through a dithiol linker, is pinned and its position does not change significantly with the particle size.

5.3.2 Energy architecture. Figure 5.5 shows a plot of the HOMO and LUMO energy positions for the differently sized NPs. The NP size assignments are made based upon the position of the first absorption peaks that were observed in solution for the NPs. The HOMO positions in this graph include those taken from the oxidation potential of the NPs. The data for the HOMO energy display a relatively flat size dependence for both the CdSe and CdTe NPs. The voltammetry experiments reveal a negative energy shift with decreasing size for CdSe NPs with sizes below about 2.8 nm. The diagram in figure 5.5 assumes that the HOMO is pinned when NPs are immobilized on the dithiol SAM. Hence, the LUMO energy should shift in the same manner as does the energy gap with the change in the NP size. The voltammograms indicate HOMO energies for CdTe NPs that are higher than those for CdSe NPs at all tested sizes. While the position of the LUMO energies change with the NP size. The smallest CdTe NP of 1.9 nm has the highest LUMO energy. When the CdSe NP size is above 2.8 nm, its LUMO energy lies below that found for CdTe NP sizes less than 3.5 nm.

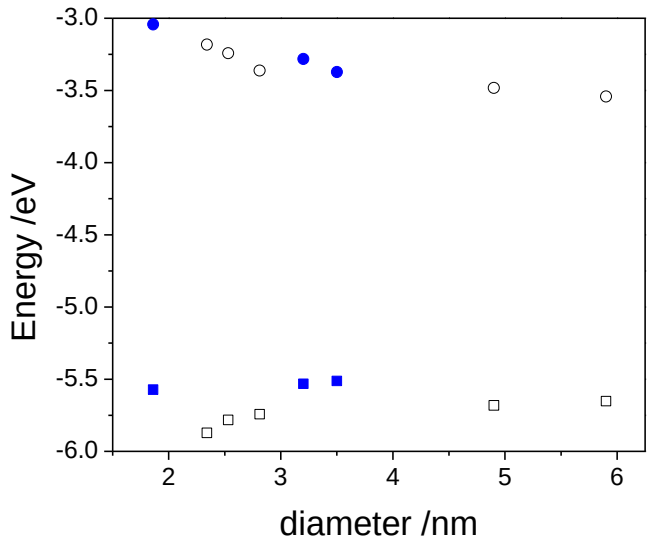

Figure 5.5 The graph plots the HOMO energies (open squares for CdSe and filled squares for CdTe) and LUMO energies (open circle for CdSe and filled circle for CdTe) of the different NPs as a function of their diameter. The error bars are smaller than the size of the symbols.

5.3.3 Photocurrent Studies

To test the impact of the NP energetics on the efficiency of photocurrent generation, two different bilayer assemblies were constructed (see Figure 5.6). Figure 5.6 shows the energetic diagrams for the NPs immobilized onto the Au electrode. The holes in the outer layer of NPs are scavenged by triethanolamine, a known hole scavenger in solution. With larger size of CdSe (625 nm) and smaller size of CdTe (492 nm), large energy gradients for both the LUMO and HOMO are created. The LUMO and HOMO for the chosen CdSe NPs are -3.9 eV and -5.88 eV, and for the chosen CdTe NPs they are -3.04 eV and -5.56 eV. When CdSe NPs were placed in the inner layer and CdTe NPs were placed in the outer layer (figure 5.6A), the dark electron transfer from the outer layer of CdTe NP to the Au electrode is difficult because of the long distance (> 4 nm). However, after excitation from the HOMO to LUMO in the CdSe NP, electrons can be injected into the Au electrode; i.e., the empty orbitals in the CdSe HOMO

facilitate the charge transfer. When CdTe NPs were placed in the inner layer and CdSe NPs were placed in the outer layer (figure 5.6B), the outer CdSe layer acts to block the hole scavenging because of its lower HOMO level. Thus, the excited electrons and holes efficiently recombine at the Au electrode and a smaller photocurrent is expected.

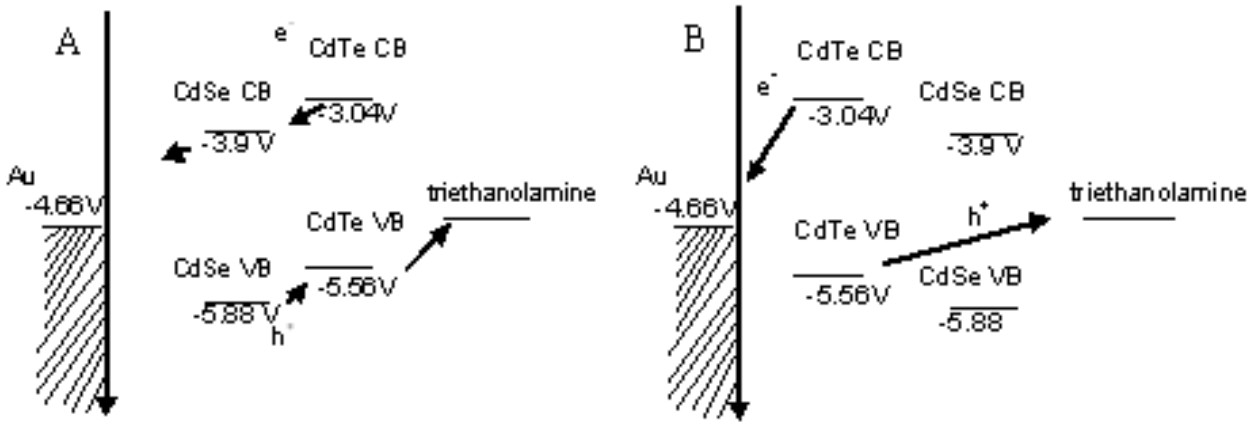

Figure 5.6 (A) Energy scheme for Au-dt-CdSe-dt-CdTe system. (B) Energy scheme for Au-dt-CdSe-dt-CdTe system.

This hypothesis was tested by both the cyclic voltammetry and photocurrent measurements of these assemblies. Figure S5.5 in the supporting information shows the cyclic voltammograms for Au-dt-CdSe-dt-CdTe system both in the dark and under illumination. Figure 5.7 shows the photocurrent dependence on potential (i.e., difference of the light and dark voltammograms) in which an anodic peak occurs at about 1.1 V, corresponding to the oxidation peak at the CdTe HOMO.

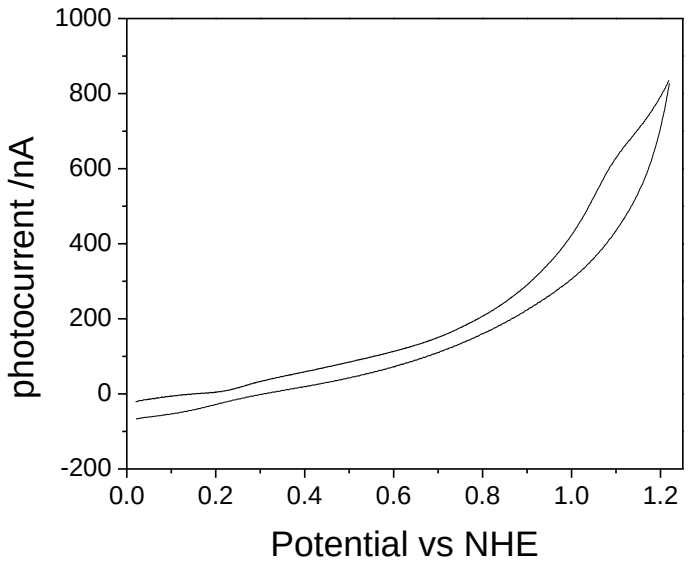

Figure 5.7 Photocurrent for Au-dt-CdSe-dt-CdTe system after dark current subtraction in 100 mM pH 3 phosphate buffer.

The photoresponse for the Au-dt-CdSe-dt-CdTe system here is similar to that reported recently for Au-dt-CdS.[30,31] The anodic photocurrent instantly flowed at the commencement of illumination and reached a steady-state within a few seconds. When the illumination was terminated, the anodic photocurrent quickly fell almost to zero. Figure 5.8a is representative of the response observed in the potential range 0.3 to 1.2 V. The steady-state photocurrent dependence of the potential is shown in figure 5.8b. The data correspond well with the results of cyclic voltammetry. The modified electrode interface may be viewed as a metal-insulator-nanoparticle junction. Current flows across such a junction as a result of electrons tunneling between the NPs and the metal. A photocurrent flows when photogenerated charge carriers are transferred between the outer surface of the NP film and the underlying Au substrate. The model of this process in figure 5.6a involves the oxidation of triethanolamine by the photogenerated positive hole followed by injection of electrons from the photoexcited CdTe and CdSe to the substrate across the dithiol layer. The potential dependence of the photocurrent can be explained

by considering the relative position of the LUMO of CdSe and CdTe to the electrode potential. When the electrode potential is more positive than the LUMO of CdSe, the photoexcited electron is injected into the electrode thus leading to the anodic photocurrent.

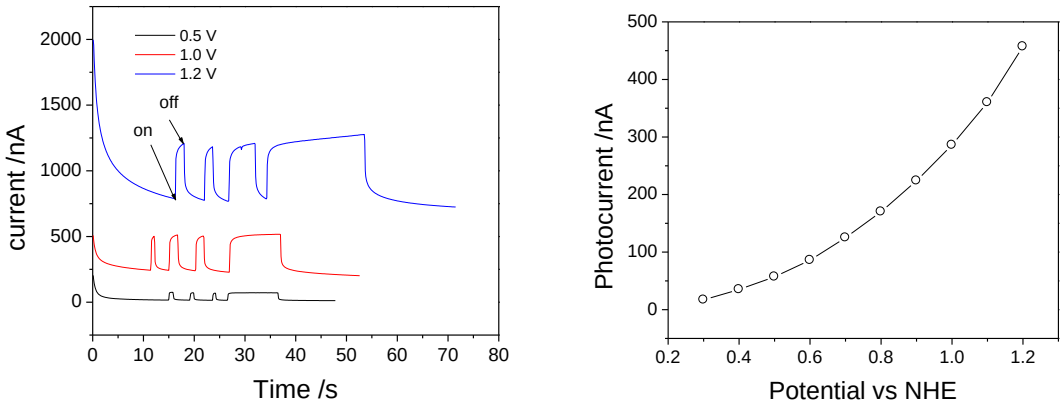

Figure 5.8 (A) Photocurrent recorded at potential above 0.3 V. (B) Photocurrent dependence of potential the of Au-dt-CdSe-dt-CdTe in 10m mM pH 3 phosphate solution containing 20 mM triethanolamine. The error bars are smaller than the size of the symbols.

The cyclic voltammograms for the Au-dt-CdTe-dt-CdSe system (Fig 5.6B) are shown in figure 5.9. Two oxidation peaks were observed at the potentials of 0.8 V and 1.1 V. When the potential was scanned positively, the direct electron transfer of CdTe was observed at a potential of 1.1 V. Because the HOMO of CdSe is lower than HOMO of CdTe, the HOMO electron transfer of CdSe is blocked. Surprisingly, a weak peak is observed near 0.8 V and it is tentatively assigned to a filled interband trap state (i.e., between the HOMO and LUMO) in the CdSe NPs, and it is interpreted as the higher energy level of trap states in the CdSe particle than the HOMO of CdTe particle. Thus, this layout facilitates the trap state electron transfer.

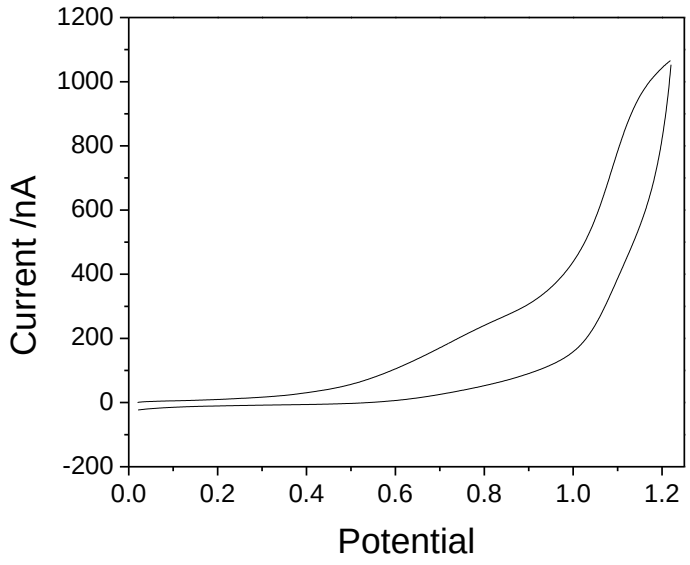

Figure 5.9 Cyclic voltammogram of for Au-dt-CdTe-dt-CdSe system in 100 mM pH 3 phosphate buffer.

The photoelectrochemical response for the Au-dt-CdTe-dt-CdSe system in the potential range of 0.4 to 0.9 V is shown in figure 5.10A, and the photocurrent dependence on the applied potential is shown in figure 5.10B. The photocurrent is only a few nanoamperes, which is 100 times smaller than the Au-dt-CdSe-dt-CdTe system. The energy scheme in figure 6B explains the large decrease in photocurrent. The outer CdSe layer acts to block the hole scavenging because of its lower HOMO level. Thus, the excited electrons and holes efficiently recombine at the Au electrode. The small photocurrent indicates the pinhole between the two layers which is also expected because of the uneven layer structure.

We observe a hundred-fold change in the photocurrents of Au-dt-CdTe, Au-dt-CdSe, Au-dt-CdTe-dt-CdSe and Au-dt-CdSe-dt-CdTe at an applied potential of 0.5 V. The highest photocurrent is 60 nA and occurs for Au-dt-CdSe-dt-CdTe, indicating that the inner CdSe layer facilitates electron transfer by acting as a relay. This photocurrent is six times larger than the 10 nA photocurrent for a Au-dt-CdTe monolayer film. Note that both NP layers are photoexcited by

the incident light. The lower photocurrent of 0.6 nA occurs for the Au-dt-CdTe-dt-CdSe assemblies for which the energy architecture inhibits electron transfer; i.e. the CdTe layer behaves as a barrier from the outer CdSe layer.

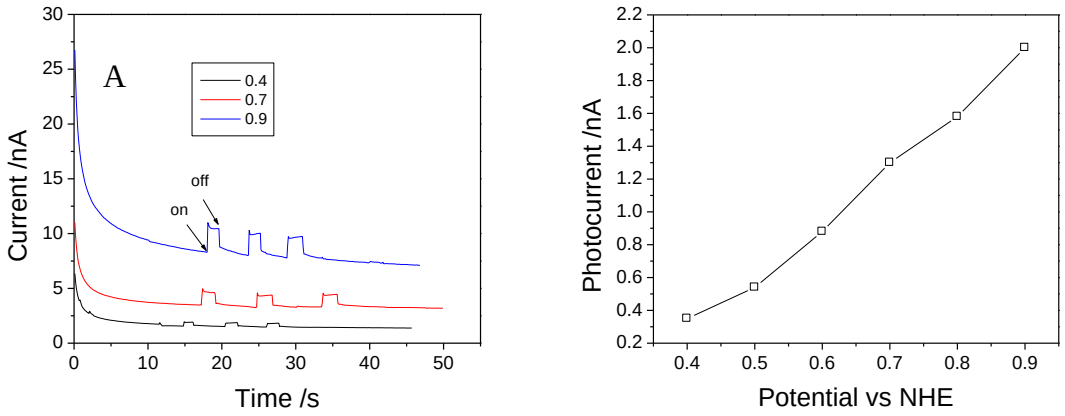

Figure 5.10 (A) Photocurrent recorded at potential above 0.4 V. (B) Photocurrent dependence of the potential of Au-dt-CdTe-dt-CdSe in 10m mM pH 3 phosphate solution containing 20 mM triethanolamine. The error bars are smaller than the size of the symbols.

CdSe nanoparticles bilayer: While the energy architecture shown in Figure 5.6 was realized through manipulation of the NP particle composition and size, it should also be possible to change the energy architecture by manipulating the NP size of a given composition. Figure 11A shows cyclic voltammograms for a CdSe bilayer system immobilized onto the Au electrode. The NP sizes are 5.91 nm and 2.35 nm. Because the HOMO position is pinned, both the "small on large" and "small on large" show similar oxidation peaks in the voltammogram. The band gap is estimated to be 1.99 eV for the larger NP and 2.48 eV for the smaller NP, and the LUMO position shifts as the size of the CdSe particle shifts,[14] giving rise to a 0.49 eV LUMO energy shift. In the "small on large" system, LUMO energy level of the 2.35 nm sized particle is higher than that of 5.91 nm sized particle, so the layout facilitates the electron transfer for both layers. While on the "large on small" system, the outer layer LUMO position is lower than the inner

layer LUMO position, so the layout can only reflect the inner layer electron transfer. Photogenerated holes can hop through the layers for both cases. Figure 11B compares the photocurrent for both layouts. The highest photocurrent is 18 nA and occurs for "small on large" system, which is about twice the 10 nA photocurrent for the Au-dt-CdSe monolayer film, reflecting the photoresponse for both the inner and outer CdSe NPs. The lower photocurrent of 5 nA occurs for "large on small" system, indicating a slower hole scavenging process.

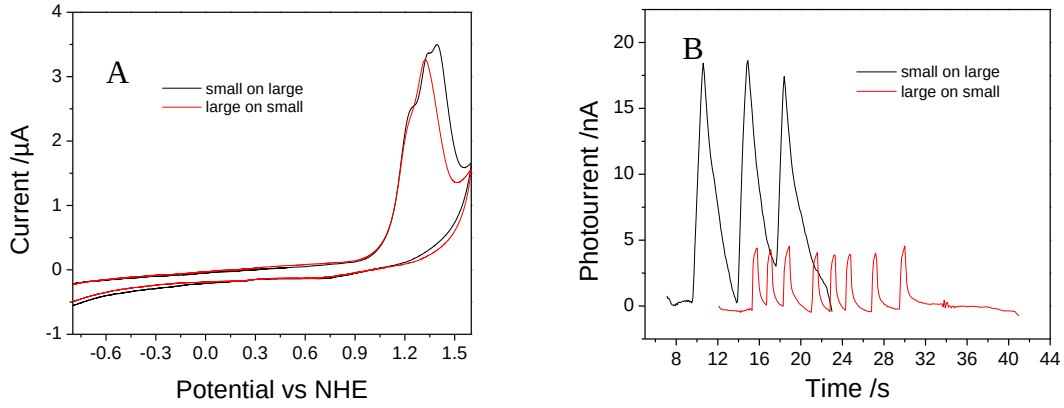

Figure 5.11 (A) Cyclic voltammogram for CdSe NPs bilayer system with particle sizes of 5.91 nm and 2.35 nm. Scan rate: 100 mV/s (B) Representative photoelectrochemical responses from the CdSe NPs bilayer system

5.4 Conclusions

Semiconductor nanoparticles have been successfully immobilized onto the Au electrodes through a dithiol SAM. The band edges of the NPs were determined by cyclic voltammetry. The energy architecture of the NP bilayers was varied to explore its impact on photocurrent generation. To maximize the energy gradient for different layers, CdSe of larger size and CdTe of smaller size were chosen. When the smaller sized CdTe is in the outer layer, a high photocurrent is observed and can be explained as the facilitated electron transfer by the inner CdSe layer. When the larger sized CdSe is in the outer layer, a very low photocurrent is observed. In this case, the outer layer of CdSe acts to block the hole scavenging. Also bilayer

system of differently sized CdSe NPs was examined. The photocurrent is much larger for the "small on large" system. The "small on large" system reflects the photoresponse for both the inner and outer CdSe NPs, while the "large on small" system can only reflect the photoresponse for inner layer CdSe NPs.

5.5 Acknowledgement. This work was supported by the US-DOE (grant no. ER46430).

References

(1) Kamat, P. V. *The Journal of Physical Chemistry C* **2007**, *111*, 2834-2860.

(2) Zhang, J. Z. *J. Phys. Chem. B* **2000**, *104*, 7239-7253.

(3) Guldi, D. M.; Zilbermann, I.; Anderson, G.; Kotov, N. A.; Tagmatarchis, N.; Prato, M. *J. Mater. Chem.* **2005**, *15*, 114-118.

(4) Robel, I.; Subramanian, V.; Kuno, M.; Kamat, P. V. *J. Am. Chem. Soc.* **2006**, *128*, 2385-2393.

(5) Shockley, W.; Queisser, H. J. *J. Appl. Phys.* **1961**, *32*, 510-19.

(6) Nozik, A. J. *Physica E (Amsterdam, Neth.)* **2002**, *14*, 115-120.

(7) Kamat, P. V. *J. Phys. Chem. C* **2008**, *112*, 18737-18753.

(8) Landsberg, P. T.; Nussbaumer, H.; Willeke, G. *J. Appl. Phys.* **1993**, *74*, 1451-2.

(9) Weller, H. *Adv. Mater. (Weinheim, Ger.)* **1993**, *5*, 88-95.

(10) Weller, H.; Schmidt, H. M.; Koch, U.; Fojtik, A.; Baral, S.; Henglein, A.; Kunath, W.; Weiss, K.; Dieman, E. *Chem. Phys. Lett.* **1986**, *124*, 557-60.

(11) Brus, L. E. *J. Chem. Phys.* **1983**, *79*, 5566-71.

(12) Brus, L. *J. Phys. Chem.* **1986**, *90*, 2555-60.

(13) Kucur, E.; Riegler, J.; Urban, G. A.; Nann, T. *J. Chem. Phys.* **2003**, *119*, 2333-2337.

(14) Markus, T. Z.; Wu, M.; Wang, L.; Waldeck, D. H.; Oron, D.; Naaman, R. *J. Phys. Chem. C* **2009**, *113*, 14200-14206.

(15) Carlson, B.; Leschkies, K.; Aydil, E. S.; Zhu, X. Y. *J. Phys. Chem. C* **2008**, *112*, 8419-8423.

(16) Zanio, K. *Semiconductors and semimetals, Academic: New York* **1978**, *13*.

(17) Gao, M.; Kirstein, S.; Moehwald, H.; Rogach, A. L.; Kornowski, A.; Eychmueller, A.; Weller, H. *J. Phys. Chem. B* **1998**, *102*, 8360-8363.

(18) Gao, M.; Lesser, C.; Kirstein, S.; Mohwald, H.; Rogach, A. L.; Weller, H. *J. Appl. Phys.* **2000**, *87*, 2297-2302.

(19) Poznyak, S. K.; Osipovich, N. P.; Shavel, A.; Talapin, D. V.; Gao, M.; Eychmueller, A.; Gaponik, N. *J. Phys. Chem. B* **2005**, *109*, 1094-1100.

(20) Li, J.; Zou, G.; Hu, X.; Zhang, X. *J. Electroanal. Chem.* **2009**, *625*, 88-91.

(21) Bae, Y.; Myung, N.; Bard, A. J. *Nano Lett.* **2004**, *4*, 1153-1161.

(22) Gaponik, N.; Poznyak, S. K.; Osipovich, N. P.; Shavel, A.; Eychmueller, A. *Microchim. Acta* **2008**, *160*, 327-334.

(23) Ogawa, S.; Hu, K.; Fan, F.-R. F.; Bard, A. J. *J. Phys. Chem. B* **1997**, *101*, 5707-5711.

(24) Yu, W. W.; Qu, L.; Guo, W.; Peng, X. *Chem. Mater.* **2003**, *15*, 2854-2860.

(25) Basova, L. V.; Kurnikov, I. V.; Wang, L.; Ritov, V. B.; Belikova, N. A.; Vlasova, I. I.; Pacheco, A. A.; Winnica, D. E.; Peterson, J.; Bayir, H.; Waldeck, D. H.; Kagan, V. E. *Biochemistry* **2007**, *46*, 3423-3434.

(26) Wang, L.; Waldeck, D. H. *J. Phys. Chem. C* **2008**, *112*, 1351-1356.

(27) Haram, S. K.; Quinn, B. M.; Bard, A. J. *J. Am. Chem. Soc.* **2001**, *123*, 8860-8861.

(28) Brus, L. E. *J. Chem. Phys.* **1984**, *80*, 4403-9.

(29) Widrig, C. A.; Chung, C.; Porter, M. D. *J. Electroanal. Chem. Interfacial Electrochem.* **1991**, *310*, 335-59.

(30) Nakanishi, T.; Ohtani, B.; Uosaki, K. *J. Electroanal. Chem.* **1998**, *455*, 229-234.

(31) Hickey, S. G.; Riley, D. J.; Tull, E. J. *J. Phys. Chem. B* **2000**, *104*, 7623-7626.

Energy Architecture Dependence on the Ordering of the CdSe/CdTe Nanoparticles

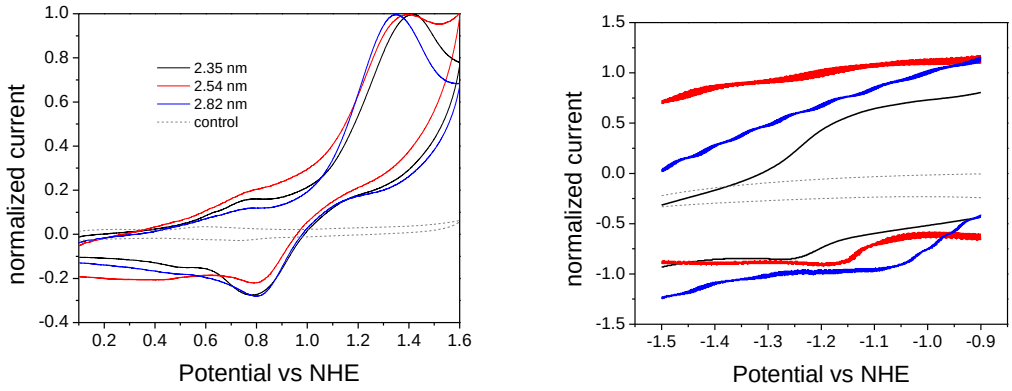

Figure S5.1 Oxidation (A) and reduction (B) voltammograms for different sizes of CdSe NPs immobilized onto a C10 dithiol SAM in acetonitrile solution (the black trace is 2.35 nm NPs, the red trace is 2.54 nm NPs, the blue trace is 2.82 nm NPs and the grey dashed trace is dithiol SAM with no NPs). The scan rate is 100 mV/s. The traces shown in panel B are an expanded region of a broader scan voltammogram.

Figure S5.1 shows cyclic voltammograms for three differently sized CdSe NPs adsorbed on a dithiol SAM on a gold electrode in acetonitrile solution. The voltammograms in Figure S5.1a show strong oxidation waves in the range of 1.22 V to 1.44 V versus NHE that depend on the different particle sizes. The oxidation and corresponding reduction peaks do not appear to change significantly with the potential scan rate. Following these earlier results, the peak of the oxidation wave is assigned to the oxidation potential of the NP. Eventually, with subsequent potential scans the oxidation peaks disappear, suggesting that the oxidation/corrosion products may form and the process is not totally reversible. Assuming that the particle charging energy can be neglected, the oxidation potential corresponds to the HOMO energy. Using the IUPAC value for the absolute electrode potential, 4.44 V, these voltammograms indicate energies of 5.66

V to 5.88 V on the vacuum scale. These values are shifted by about 100 mV from those observed in the photoemission experiments.

The LUMO energies of the CdSe NPs could be determined from the reduction waves and were found to lie between -0.89 V and -1.25 V versus NHE, depending on the particle size. Figure S5.1b shows some example voltammograms. In this case the assignment of the peak was less clear. In part, the smaller signal levels reflect the irreversibility observed in the oxidation peaks. Nevertheless, an excellent agreement between the values assigned in this manner and those calculated by adding the bandgap energy of the NP to the observed HOMO energy was found.

Photoelectrochemistry. Figure S5.2 shows a photocurrent-time plot of a CdSe/10-SAM/gold electrode in 5 mM Ferrocene in acetonitrile buffer solution. The electrode was illuminated with chopped white light from a 150 W xenon lamp. At potentials more positive than 0 V, a steady state photocurrent was observed. The observation of a photocurrent means that tunneling between the metal and the quantum dot can compete with intraparticle decay.

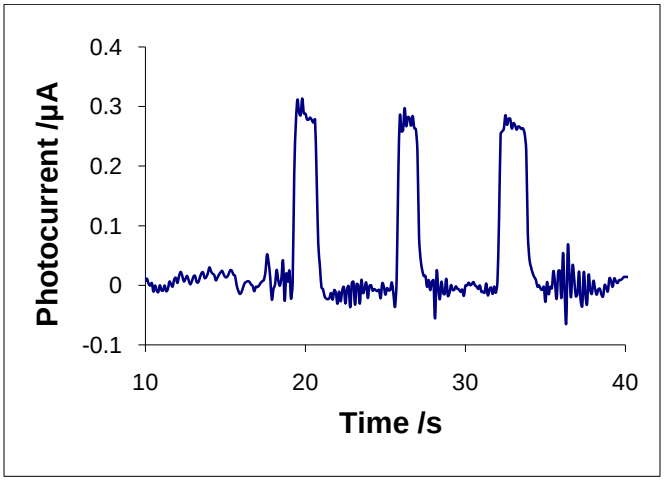

Figure S5.2 Representative photoelectrochemical responses from the CdSe/10-SAM/gold electrode at a bias of 0.8 V in a three-electrode cell.

An action spectrum for the CdSe/10-SAM/gold electrode is shown in Figure S5.3 and was obtained by measuring the cathodic photocurrent under irradiation with light. Figure S5.3 compares the absorption spectrum of the CdSe NP's first excitonic absorption peak of 625 nm with the action spectrum of the same particle. Clearly, the signal level decreases as the light wavelength increases for both the absorption spectrum and action spectrum; however, the first excitonic absorption peak is not as clear in the action spectrum as in the absorption spectrum.

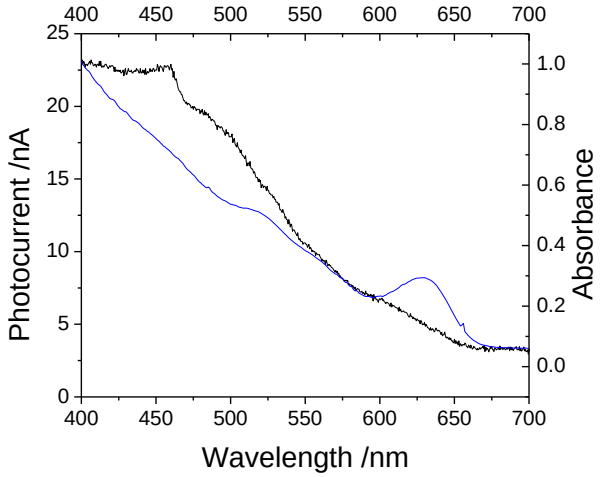

Figure S5.3 Photocurrent action spectrum (blue curve) of CdSe/10-SAM/gold electrode and absorption spectrum (black curve) of the same size CdSe in solution.

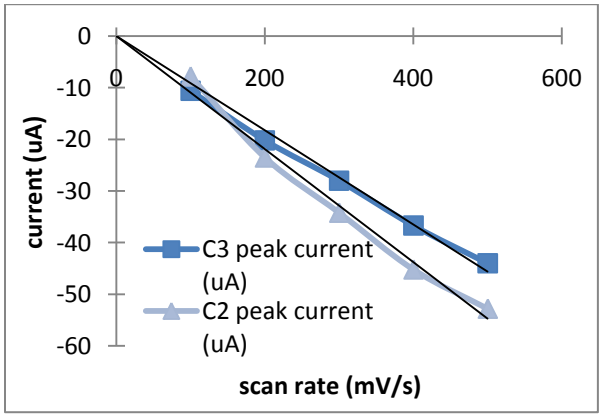

Figure S5.4 Peak current dependence on potential scan rate for Au electrode in aqueous solution containing MPA-capped CdTe NPs.

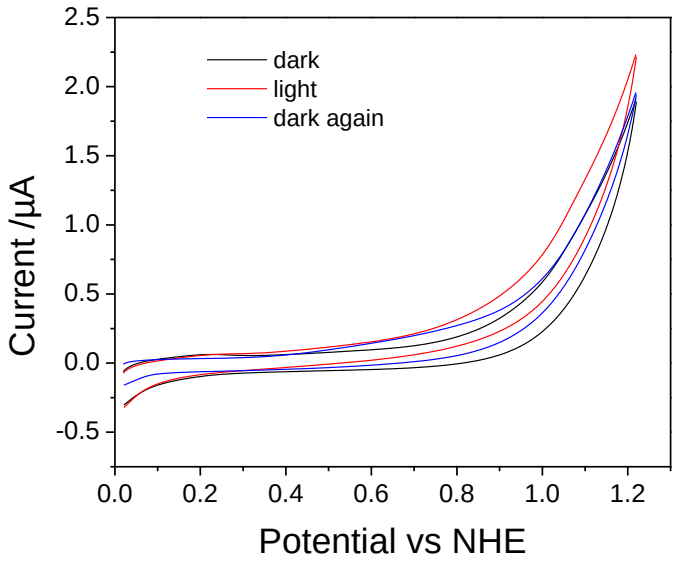

Figure S5.5 Cyclic voltammogram of for Au-dt-CdSe-dt-CdTe system in dark and illumination. Scan rate: 50 mV/s

Figure S5.5 shows the cyclic voltammograms for Au-dt-CdSe-dt-CdTe system both in the dark and under illumination. Direct electron transfer can hardly be resolved for both cases. However, the overall current was larger under illumination and fell back once the illumination was terminated.

6.0 CONCLUSIONS

This thesis consists of two parts. The first part described the effect of solution pH value and cardiolipin binding on the comformation of metalloprotein immobilized at the metal surface, and how the comformation changes affect the metalloprotein's peroxidase activity. The second part described studies of semiconductor nanoparticles to determine the positions of the electronic states, both occupied and unoccupied, by cyclic voltammetry and photoemission spectroscopy. It was found that the photoresponse of the nanoparticles depends on the ordering of nanoparticles immobilized at the electrode surface.

In chapter 2, cytochrome *c* was covalently attached onto mixed carboxylic acid and hydroxyl terminated SAM coated electrodes for preventing the loss of cytochrome *c* during the experiment. The amount of immobilized cytochrome *c* onto the SAM is 1 to 2 pmol/cm^2, a surface coverage of 7%~10%. The chemically modified gold ball electrode was used to explore how the unfolding of cytochrome *c* affects its electrochemistry. Cyclic voltammetry allows one to monitor the redox reaction as cytochrome *c* unfolds with decreasing pH. The effect of pH on cytochrome denaturation is irreversible. As the pH decreases, the peak currents strongly decrease. At pH = 4, the Faradaic peak current drops almost to zero. When cytochrome *c* is unfolded by lowering the pH, the heme pocket loses its integrity and unwraps, exposing the heme to solvent molecules. Easy access to the heme pocket by the H_2O_2 substrate facilitates the heme's peroxidase activity and electrocatalytic current can be observed. The current increased

with the concentration of H_2O_2 and the apparent Michaelis-Menten constant K_m was determined to be 7.9 mM and 144.3 mM for cytochrome *c* at pH 3 and pH 7 respectively, indicating that the peroxidase activity of denatured cytochrome *c* decreases at higher pH.

In chapter 3, cytochrome *c*'s interaction with mitochondria-specific cardiolipin (CL) and subsequent peroxidase activity were studied on. Cytochrome *c* (cyt *c*) loses its tertiary structure and its peroxidase activity dramatically increases once it binds to CL. The CL induced peroxidase activity of cyt *c* has been found to be important for selective CL oxidation in cells undergoing programmed death. During apoptosis, the peroxidase activity and the fraction of CL-bound cyt *c* markedly increases suggesting that CL may act as a switch to regulate cyt *c*'s mitochondrial functions. Using cyclic voltammetry and equilibrium redox-titrations, we show that the redox potential of cyt *c* shifts negatively by 350-400 mV upon binding to CL-containing membranes. Consequently, functions of cyt *c* as an electron transporter and cyt *c* reduction by complex III are strongly inhibited. Further, CL/cyt *c* complexes are not effective in scavenging superoxide anions and are not effectively reduced by ascorbate. Thus, both redox properties and functions of cyt *c* change upon interaction with CL in the mitochondrial membrane, diminishing cyt *c*'s electron donor/acceptor role and stimulating its peroxidase activity.

In chapter 4, assemblies of CdSe nanoparticles (NPs) on a dithiol coated Au electrode were created and their electronic energetics were quantified. We describe the energy level alignment of the filled and unfilled electronic states of CdSe nanoparticles with respect to the Au Fermi level. Using cyclic voltammetry it was possible to measure the energy of the filled states of the CdSe NPs with respect to the Au substrate relative to a $Ag/AgNO_3$ electrode, and by using photoemission spectroscopy it was possible to independently measure both the filled state energies (via single photon photoemission) and those of the unfilled states (via two photon

photoemission) with respect to the vacuum level. Comparison of these two different measures shows good agreement with the IUPAC accepted value of the absolute electrode potential. In contrast to the common model of energy level alignment, the experimental findings show that the CdSe filled states become 'pinned' to the Fermi level of the Au electrode, even for moderately small NP sizes.

In chapter 5, CdSe and CdTe semiconductor nanoparticles have been successfully immobilized onto the Au electrodes through a dithiol linker. The band edges of the NPs were determined by cyclic voltammetry. Bilayer structures were produced by assembling different sizes of CdSe and CdTe particles. The energy architecture of the NP bilayers was varied to explore its impact on photocurrent generation. To maximize the energy gradient for different layers, CdSe of larger size and CdTe of smaller size were chosen. When the smaller sized CdTe is in the outer layer, a high photocurrent is observed and can be explained as the facilitated electron transfer by the inner CdSe layer. When the larger sized CdSe is in the outer layer, a very low photocurrent is observed. In this case, the outer layer of CdSe acts to block the hole scavenging. Also bilayer system of differently sized CdSe NPs was examined. The photocurrent is much larger for the "small on large" system.

In summary, nanoscale objects, both protein and inorganic nanoparticles, were immobilized at a metal electrode. Cyclic voltammetry was used to explore the redox molecules' dynamic and kinetic properties. The metalloprotein's peroxidase activity increases by lowering of the solution pH value or binding of cardiolipin. When cytochrome *c* is unfolded by lowering the pH, the heme pocket loses its integrity and unwraps, exposing the heme to solvent molecules. Easy access to the heme pocket by the H_2O_2 substrate facilitates the heme's peroxidase activity. The redox potential of cyt *c* shifts negatively by 350-400 mV upon binding to CL-containing

membranes. Thus, both redox properties and functions of cyt *c* change upon interaction with CL in the mitochondrial membrane, diminishing cyt *c*'s electron donor/acceptor role and stimulating its peroxidase activity. The electronic states of the semiconductor nanoparticle were determined by cyclic voltammetry and photoemission spectroscopy. The positions obtained from the electrochemistry measurements are shifted systematically by about 100 mV more negative than those found from the photoemission measurement.The filled states become 'pinned' to the Fermi level of the Au electrode. The photoresponse of the nanoparticles can be controlled by the sizes and ordering of the immobilized nanoparticles. CdSe of larger size and CdTe of smaller size were chosen to optimize the photoresponse of the assemblies.